The Effects of an Arbitrary Waveform Generator on Single-Electron Pumps in GaAs/AlGaAs Heterostructures

by:

Dominique Gouveia

B.Sc., Eng., The University of Cape Town, 2014
M.Sc., Eng., The University of Cape Town, 2017

Supervisor: Assoc. Prof. Mark Blumenthal

A DISSERTATION SUBMITTED IN PARTIAL FULFILLMENT OF
THE REQUIREMENTS FOR THE DEGREE OF
DOCTOR OF PHILOSOPHY

in:

The Faculty of Science

(Physics)

University of Cape Town

February 2021

Name: Dominique Gouveia

Student Number: FRGDOM001

Declaration

I know that plagiarism is wrong. Plagiarism is to use another's work and pretend that it is one's own.

I have used the IEEE convention for citation and referencing. Each contribution to, and quotation in, this dissertation from the work(s) of other people has been attributed, and has been cited and referenced.

This dissertation is my own work.

I have not allowed, and will not allow, anyone to copy my work with the intention of passing it off as his or her own work.

Signature Signed by candidate

Date 17/02/2021

Abstract

The Ampere is the base unit of electric current in the international system of units (SI). The international committee for weights and measures (CIPM) has recently redefined the Ampere in terms of the elementary charge $e = 1.602176634 \text{ x } 10^{-19}$ C of the electron. National metrology institutes worldwide are working towards the realisation of this definition by using the single-electron pump technology. In this report, we studied the effects of the arbitrary waveform generator (AWG) on the single-gate modulated pump in gallium arsenide (GaAs)/aluminium gallium arsenide (AlGaAs) heterostructure. We fabricated a split-finger gate electron pump. We designed five trapezoidal waveforms and a sinusoidal waveform in MATLAB. The frequency of the sinusoid was 180 MHz, while the frequency of the five trapezoids was 181.81 MHz due to the different number of samples used to create the waveforms. The amplitude of these waveforms was 1 volt peak to peak (Vp-p). We conducted three experiments, labelled A to C, in a dilution refrigerator at a temperature of around 150 mK and in zero external magnetic fields.

In experiment A, we compared the pump maps of a sinusoid outputted by a signal generator (SG) to the sinusoid outputted by an arbitrary waveform generator. We observed three main differences: firstly, the AWG pump map was more robust in entrance voltage compared to the SG pump map. The first plateau of the AWG spanned 760 mV as opposed to the 600 mV spanned by the SG. Secondly, the AWG produced a pump map that contains a very high degree of ripples on the onset lines compared to the smoother onset lines of the signal generator. Lastly, both the AWG and SG allowed us to pump in the 'long plateau regime[1]'. In experiment B, we observed the pump behaviour in response to AWG pulses of different rising edge slopes. We found that plateaus 1, 2 and 3 were elongated

[1]The phrases 'long plateau regime' or 'long pumping regime' was coined by Howe and Blumenthal, et al. [1]. It means that we can elongate the pump map or the plateaus along the exit voltage with parameters such as the source-drain bias, magnetic fields, pulse waveforms, etc.

(robust) over the entire exit voltage range for the entrance voltage interval from -600 mV to -400 mV. In this entrance voltage interval, we found that the pumped current restores with a steeper sinusoidal slope on the rising edge of the pulse. In experiment C, we selected a robust third plateau at an entrance voltage of -530 mV and successfully tuned it with the source-drain bias voltage. The third plateau migrated from the first to the eighth plateau as we swept the source-drain bias from – 100 mV to 200 mV in increments of 1 mV. The plateaus were very robust in exit voltage for the source-drain bias voltages above -70 mV. Below -70 mV, we began to lose robustness.

The main implication of these results is that whether we are pumping with an AWG or SG makes a difference. We can make the quantised current robust in exit voltage by using an arbitrary waveform. Furthermore, we can fine-tune a plateau with source-drain bias, even if the plateau is not an integer multiple of ef. In this report, we tuned the 3rd plateau to the 8th plateau. These effects are yet to be properly understood and will, when properly understood, have a significant implication on the way we understand single-electron pumps. It might give us a new perspective on single-electron pumps concerning the source-drain bias, split-finger gate pumps, and different modulation waveforms. Moreover, it might bring us closer to the realisation of the new definition of the Ampere.

Acknowledgment

I would like to express my gratitude to the following people for contributing to the successful completion of this research project:

- **Associate Professor Mark Blumenthal**, for allowing me the opportunity to get a PhD in physics (in the field of nano-electronics) amid the struggle I have securing proper documentation in South Africa since 1997. I feel highly privileged to have had you as my supervisor. Thank you for all the support you have given me through my financial difficulties. It was always fun to be working in the lab with you. We would often exclaim in utter excitement: "I could teach a course!" after overcoming a difficulty or an issue. Thank you.

- **Hume Howe**, your presence in the UCT nano-electronics lab has always been a benefit to us all. I am glad to have met you, and I enjoy working with you. Thank you for all of your hard work. We had good times staying in the lab past midnight working on the fridge. Thanks for allowing me to stay at your place during those times. Also, thanks for all the insightful discussions we always had over Skype. It enhanced my understanding of the work.

- **My colleagues in the nano-electronics group**, I enjoyed being part of the group. Sam, Sahl, Nasheeta, Marija, Brian, Oliver, Zakeele, Carine and Hisaan, thank you all for being part of such an awesome group. May your futures be bright.

- **Prof. Sir Michael Pepper**, Thank you for inviting me to the weekly talks and for allowing me to present as well. I enjoyed listening to the talks.

- **Physics department's technical team** Kerwin, Clint and James, thank you for all your hard work. We are very fortunate to have you in the physics department.

- **The physics department**, thank you for permitting me to get a degree in physics. You have a great team, lead by a wonderful HOD, prof Buffler.
- **To all my friends**, I have been truly blessed to have you as friends. Friends that will go above and beyond for me. Thank you so much for everything you have done for me.

Table of Contents

List of Figures

List of Tables

Abbreviation

Abbreviations

AC: Alternating Current
AFG: Arbitrary Function Generators
AFM: Atomic Force Microscope
AuGeNi: Gold Germanium Nickel
AWG: Arbitrary Waveform Generators
GaAs/AlGaAs: Gallium Arsenide /Aluminium Gallium Arsenide
BIPM: International Bureau of Weights and Measures
CAD: Computer-Aided Design
CCEM Consultative Committee for Electricity and Magnetism
CGPM: General Conference on Weights and Measures
CIPM: International Committee for Weights and Measures
CPR: Conventional Pumping Regime
CVD: Chemical Vapor Deposition
DAQ: Data Acquisition
DC: Direct Current
DDS: Direct Digital Synthesis
DI: Demineralization
DMM: Digital Multimeter
EBL: Electron Beam Lithography
FG: Function Generators
GHS: Gas Handling System
GPIB: General Purpose Interface Bus
HCL: Hydrochloric acid
HEMT: High Electron Mobility Transistor
H2O2: Hydrogen Peroxide
H2SO4: Sulphuric Acid

IPA: Isopropanol
ISO: The International Organization for Standardization
IVC: Inner Vacuum Can
JCGM: Joint Committee for Guides in Metrology
LCC: Leadless Chip Carrier
LN2: Liquid Nitrogen
LOR: Lift-Of Resist
LPR: Long Plateau/Pumping Regime
MBE: Molecular Beam Epitaxy
MC: Mixing Chamber
MOCVD: Metal-Organic Chemical Vapour Deposition
MODFET: Modulation-Doped Field-Effect Transistor
MOSFET: Metal-Oxide-Semiconductor Field-Effect Transistor
N2: Dinitrogen
OVC: Outer Vacuum Can
pA: pico-Amperes
PC: Computer
PCB: Printed Circuit Board
PMMA: Polymethyl Methacrylate
p-p: Peak to Peak
PR: Photoresist
Pt: Platinum
PT: Pulse Tube
PVD: Physical Vapor Deposition
QD: Quantum Dot
QPC: Quantum Point Contact
RTA: Rapid Thermal Annealer
SEM: Scanning Electron Microscope
SG or SigGen: Signal Generator
SiO2: Silicon Dioxide
SI: The International System of Units
SMP: Sub Miniature Push-on
SMU: Source Measure Unit
UCT: University of Cape Town
UHV: Ultra-High Vacuum
UV: Ultraviolet

Acronym

SAW: Surface-Acoustic Wave

SEM: Scanning Electron Microscope

SEP: Single Electron Pump

SET: Single Electron Transistor

Si-doped: Silicon-doped

SINIS: Superconductor-Insulator-Normal Metal-Insulator-Superconductor

Chapter 1

Introduction

1.1 Statement of the Problem

Humanity has engaged in measurement for millennia. It is an essential part of every human existence. In the past, measurement standards differed universally, making it difficult and confusing to convert from one to another. Today's measurement practice is very different from its early days. The international bureau of weights and measure (BIPM) has joined measurement standards into an international system of units (SI) [3]. The joint committee for guides in metrology (JCGM) defines measurement as a: **"process of experimentally obtaining one or more quantity values that can reasonably be attributed to a quantity"** [4].

National metrology institutes are responsible for realising the base SI units. Generally, realising a unit means establishing the value and the associated uncertainty of the quantity that is consistent with the definition of the unit [5]. The SI consist of seven base units, one of which is the subject of this thesis, the Ampere. In October 1948, the 9th general conference on weights and measures (CGPM) accepted the Ampere for the unit of electric current, following a definition proposed by the international committee for weights and measures (CIPM) in 1946, which states that: **"the Ampere is that constant current which, if maintained in two straight parallel conductors of infinite length, of negligible circular cross-section, and placed 1 meter apart in vacuum, would produce between these conductors a force equal to 2 x 10^{-7} newton per meter of length"** [6].

It is difficult, if not impossible, to realise the Ampere as defined above for several reasons: firstly, practical conductors have finite length and cross-section; secondly, space is the closest to a perfect vacuum we can get; Lastly, the Ampere is an electrical unit defined in terms of force, with the unit of Newton (Kgm/s^2). Thus it has the prototype of Kilogram (platinum-iridium artefact) which is drifting with time [7]. National metrology institutes do not have the resources needed to implement the definition above with the accuracy and precision required today [7] [8] [9]. The lowest demonstrated uncertainty achieved is no better than about 0.3 ppm [7].

To circumvent these limitations, metrology institutes worked outside the SI unit and used Ohm's law to define the Ampere in terms of its relation to the Ohm (Ω) and Volt (V). These units are in turn based on the quantum Hall and Josephson effects, respectively. These effects link both the Ohm and Volt to combinations of the Planck constant h and elementary charge e, which results in precise and reproducible standards of resistance and voltage based on quantum effects in semiconductor and superconductor at low-temperature [5] [7] [8]. The quantum Hall effect relates voltage to current via the von Klitzing constant, $R_K = h/e^2$. The Josephson effect relates voltage to frequency via the Josephson constant, $K_J = 2e/h$. Consequently, the current can be determined from these relationships. These standards are often referred to as 'quantum standard' because their accuracy is grounded on fundamental physics and are not dependent on the material properties and physical structure [8].

Figure (1.1a) illustrates the present realisation of the Ampere. The product $R_K K_J^2$, in the SI unit, is determined with a Watt balance and a calculable capacitor. It is then used to determine the Volt and Ohm, and hence, the Ampere. This method presents a situation in which the Volt and Ohm have a higher precision compared to their SI derived units because they are based on constants derived from fundamental effects in quantum physics. Consequently, the Volt can be realised with an uncertainty of about 6 ppb, and the Ohm with an uncertainty of about 0.2 ppb. The lowest demonstrated uncertainty for the Ampere is 0.3 ppm, from the conventional definition based on Ampere's law. This inconsistency between the SI and Ohm's law was resolved by fixing the numerical value of h and e to redefine the Kilogram and the Ampere. So that, the classical SI standard now became the quantum SI standard [7] [8] [10].

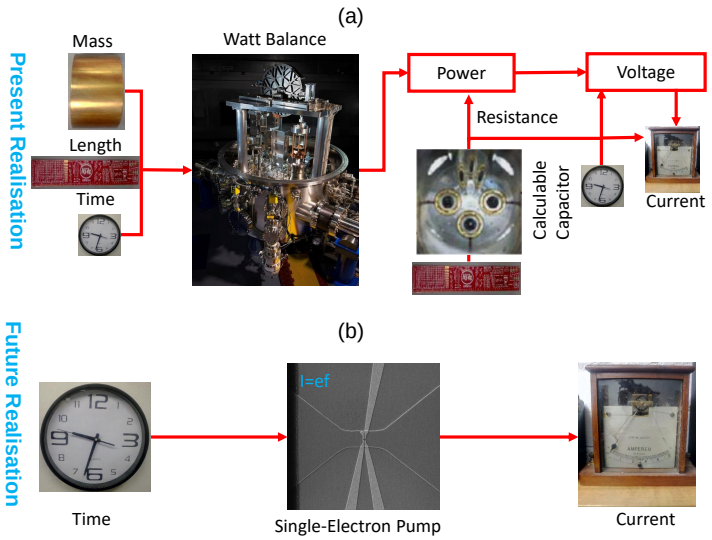

Figure 1.1: **Present (a) and future (b) realisation of the Ampere (adapted from [8] [11])**

The decision to base the SI unit on fixed fundamental constants of nature and to avoid using physical objects came into effect on May 20, 2019 [10]. Thus, the future definition of the Ampere based on a fixed numerical value of the elementary charge e, was adopted in resolution 1 of the 26th CGPM (2018), and it reads: **"the Ampere, symbol A, is the SI unit of electric current. It is defined by taking the fixed numerical value of the elementary charge e to be 1.602176634 x 10^{-19} when expressed in unit C, which is equal to A.s, where the second is defined in terms of Δv_{Cs}[1]"** [10].

This definition implies the exact relation:

$$\boxed{e = 1.602176634 \times 10^{-19} \quad \text{A.s};} \tag{1.1}$$

the exact expression for the unit Ampere is then obtained by inverting we get,

$$\boxed{1\text{A} = \left(\frac{e}{1.602176634 \times 10^{-19}}\right) \quad \text{s}^{-1};} \tag{1.2}$$

substituting reciprocal of the second we have,

$$\boxed{1A \approx 6.789687 \times 10^{8}\, e.\Delta v_{Cs}.} \tag{1.3}$$

[1]Where Δv_{Cs} is the unperturbed ground-state hyperfine transition frequency of the caesium 133 atom, with a value of 9 192 631 770 Hz [10].

Equation (1.3) implies that the flow of $6.241509074 \times 10^{18}$ elementary charges per second will produce an electric current of one Ampere. Thus, the future realisation of the Ampere is based on manipulating and transporting a known number of electrons at a known frequency. For precision metrology, this operation has to be performed at a relative error level no larger than $1e^{-8}$, while at the same time the electric current needs to be hundreds of pico-Amperes (pA) [7].

The definition of the Ampere does not state or imply any particular experimental technique for its practical realisation. We may, in principle, use any method capable of deriving an electric current value traceable to the set of seven fundamental constants. However, the consultative committee for electricity and magnetism (CCEM) [5] does provide a few primary techniques that are easiest to implement or that results in the smallest uncertainties. The single-electron transistor (SET) is one such technique. This device can be modified to a single-electron current source called 'single-electron pump'. The pump has various applications outside metrology. Such as in radiation dosimetry, environmental monitoring, calibration of detectors for airborne particles and semiconductor wafer characterization [8]. However, here we focus on using the electron pump to realise the new definition of the Ampere as presented in Figure (1.1b).

The better we can control single-electrons, the better we can realise our modern definition of the Ampere. Over the past two and a half-decades, researchers have made great strides towards better control of individual electrons [7]. Several milestones have been achieved in progressing towards a single-electron current source since the initial proposal of the single charge oscillations, and the metrological triangle in Figure (1.2) in the mid-1980s [7] [12] [13] [14]. A few years after this proposal, the first metallic and semiconductor single-electron turnstiles and pumps demonstrated quantised currents with reasonable errors, but it was still magnitudes away from what was required for electrical metrology [7] [15] [16] [17]. Five years later, the accuracy of the pump was improved by a factor of five to six orders of magnitude by significantly suppressing cotunneling events [18]. However, the trade-off to increase accuracy was a reduction in the magnitude of the output current, and an increase in device complexity [7]. In parallel to the study done by Keller et al. [18], was the work done on the surface-acoustic wave (SAW) pumps by Shilton et al. [19]. This study resulted in a significant increase in the current amplitude, yet likely due to overheating effects in the channel, it was

difficult to suppress thermal errors using this method [7]. After a decade, several new ideas were implemented. The most promising devices were single-parameter controlled semiconductor quantum dot (QD) pumps, realised by Blumenthal et al. [20] and Kaestner et al. [21], and the superconductor-insulator-normal metal-insulator-superconductor (SINIS) turnstile by Pekola et al. [22]. These simple devices promise high accuracy and scalability [23]. Kashcheyevs et al. made a major theoretical contribution by deriving an explicit fitting formula to extract the sequence of decay rate ratios from the measurements of averaged current in a periodically driven device. Previously, evaluation and benchmarking of the pumps were only possible by empirically evaluating the plateau length. However, plateaus can be systematically shifted far away from the quantised value. Thus, only the accurate model developed mainly by Kashcheyevs et al. and its subsequent high precision verification allowed substantial progress in the field [24].

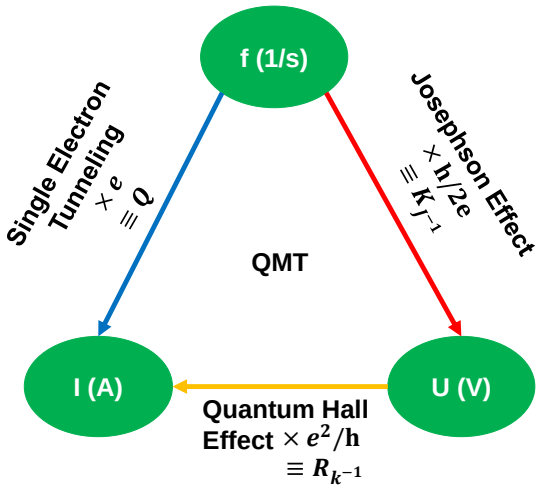

Figure 1.2: **The quantum metrology triangle linking the Ampere, Volt and frequency via the quantum Hall effect, Josephson effect and electron tunneling**

Giblin et al. [25] used an AWG to design a waveform that took into account the time-dependent electron tunnelling dynamics. He based the design on two assumptions: firstly, single-gate modulated pumps typically operate with a sinusoidal waveform. By inspecting the sinusoid, he realised that once one captures the electrons reliably in the QD, then most of the pump cycle time goes into raising and lowering the modulated gate. One can use this large 'dwell time[2]' to

[2]Time duration for the pump to eject a captured electron to the drain reservoir and to pick

operate the pump at a faster rate. Therefore, one can use an arbitrary shaped waveform for this portion of the pump cycle. The second assumption deals with capturing the electron reliably during the capture phase of the pump cycle. The high-frequency error rate is related to the rate at which one raises the modulated gate during the capture phase. Thus, if one can raise the gate slow enough during the capture phase, back tunnelling will occur, allowing one to capture the electrons reliably. From these assumptions, Giblin designed a waveform that had a sinusoidal segment during the capture phase, combined with a trapezoidal segment during the ejection and loading phase. This waveform can minimise the capture errors and allows one to increase the pump frequency. Giblin et al. [25] used this technique to study the effects an AWG has on a finger-finger gate single-electron pump. We used Giblin's scheme to study the effects an AWG has on a finger-split gate single-electron pump.

1.2 Purpose Statement

The purpose of this report is to investigate the impact that various arbitrary waveforms have on a finger-split gate pump, that is:

- we must use an arbitrary waveform generator to design and test different waveforms
- we must use these waveforms to study the behaviour of a finger-split gate pump at cryogenic temperatures.

1.3 Thesis Layout

The layout of this report is as follows: In Chapter (2), we review the theory of GaAs/AlGaAs devices. We begin with a basic introduction to the dimensionality of low-dimensional systems. We then discuss heterostructure devices and the realisation of the two, one and zero-dimensional electron gases. In Chapter (3), we discuss the principles of operation of non-adiabatic single-electron pumps and their realisation. We present the methodology used to design and carry out the experiments in Chapter (4). In this chapter, we address the fabrication of the

up an electron from the source reservoir

pumps, the validity of the instruments used, and the procedures followed to perform the measurements. We report the results of the experiments in Chapter (5). Lastly, in Chapter (6) we present and discuss the major results and their relationship to existing ones, and the limitations, implication and overall significance of our study.

Chapter 2

Review Of GaAs/AlGaAs Devices

2.1 Dimensionality of Low Dimensional Systems

Today's scientists and engineers can manufacture new kinds of materials at an atomic scale. At such a scale, we have to take quantum effects into account to understand the behaviour of these nanostructures [26] [27]. Thus, the size of the system, denoted by **L**, is very important and leads to other lengths, energy and time scales. For a three dimensional system, its size may differ in three directions in space, L_x, L_y and L_z. The study of a phenomenon at this scale requires one to scale all the other length scales relative to the size of the system. That is, the dimensionality of a system depends on the phenomenon under consideration [28] [29].

Quantum effects arise in systems that confine electrons to regions comparable to their de Broglie wavelength. This section discusses how to establish a d-dimensional system for electrons, i.e. a 0D for full confinement, 1D for transport in one direction, 2D for freedom in a plane and 3D for an unconfined system. Assuming an ideal[1] system, if electrons are confined in a certain 3D space, L_x, L_y, L_z, then for each direction $(i = x, y, z)$ a standing wave equation can be setup:

$$\boxed{\lambda_{i,j_i} = \frac{2L_i}{j_i} \qquad (j_i = 1, 2, 3...);} \tag{2.1}$$

[1]By ideal it is meant that there is no motion in the confining direction and no electron-electron or electron atom interaction.

with associated k-vectors

$$\boxed{k_{i,j_i} = \frac{j_i \pi}{L_i}.} \tag{2.2}$$

The total kinetic energy of each level characterized by the set of quantum numbers j_x, j_y, j_z is then the sum of the three components:

$$\boxed{E = \sum_{j_i} E_{j_i} = \frac{\hbar^2}{2m} \sum_{j_i} k_{j_i}^2 = \frac{\pi^2 \hbar^2}{2m} (\frac{j_x^2}{L_x^2} + \frac{j_y^2}{L_y^2} + \frac{j_z^2}{L_z^2});} \tag{2.3}$$

and the density of state is

$$\boxed{g(E) = \frac{1}{2\pi^2} (\frac{2m}{\hbar^2})^{3/2} \sqrt{E}.} \tag{2.4}$$

Furthermore, restricting the motion of electrons in the appropriate direction(s) result in the energy and density of state equations in Table (2.1) for the 2D, 1D and 0D systems. Figure (2.1) shows the relationship between the energy and density of state for each dimension. Thus, we see that the density of state is a strong function of the spatial dimension. It influences the transition of electrons from one energy state to another, an extremely important effect in the transport properties of quantum heterostructures [26].

Table 2.1: **The total kinetic energy and density of state for 2, 1 and 0 dimensional electron gases for an ideal quantum system**

Dimensions	**2D**	**1D**	**0D**
Quantized Energy	$\frac{\pi^2\hbar^2}{2m}(\frac{j_x^2}{L_x^2} + \frac{j_y^2}{L_y^2})$	$\frac{\pi^2\hbar^2}{2m}(\frac{j_x^2}{L_x^2})$	E_0
Density of state	$\frac{m}{\pi\hbar^2}$	$\frac{1}{2\pi}(\frac{2m}{\hbar^2})^{1/2}\frac{1}{\sqrt{E}}$	$\delta(E - E_0)$

By contrast, practical[2] systems do not have perfect confinement. For instance, the restriction of the motion of electrons along the z-direction happens within a small z-range comparable to the de Broglie wavelength. As a result, the energy will be strongly quantized along this small z-range, and in general, more than one energy level will be allowed [26]. This effect is termed 'degeneracy'. It is responsible for sub-bands observed in the dispersion relation and the density of state,

[2]The interaction between electrons and electron-atom is still neglected, the later interaction will result in energy bandgaps in the dispersion relation of Figure (2.2)

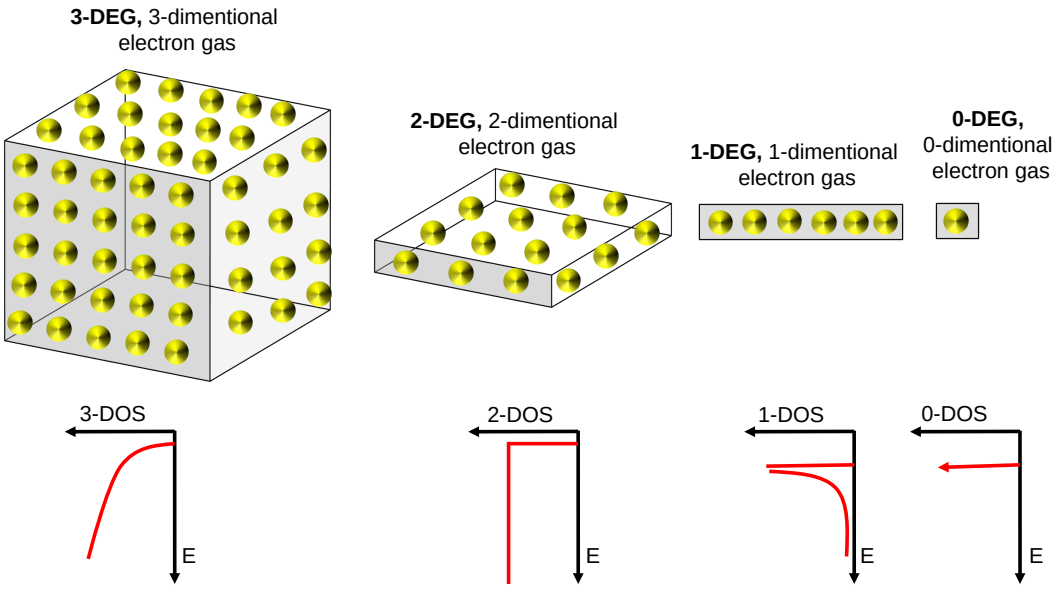

Figure 2.1: **Shows the 3, 2, 1, and 0-dimensional electrons gases, and their corresponding density of state for an Ideal system**

as shown in Figure (2.2), which is the plot of Equation (2.5) for the case of the 2DEG. The plot in Figure (2.2a) is a generalization of the ideal case, which would just be the blue parabola. For energies $E < E_0$ (region A), there are no available states. For energies between $E_0 < E < 4E_0$ (region B), we get the density of states per unit area of the perfect 2DEG. For energies in regions C and D we get twice and thrice the density of states of the perfect 2DEG respectively and so forth. This is demonstrated by the increasing step height in Figure (2.2b), where the density of states of the 2DEG is compared to the 3DEG. Thus, the system is ideal if there are no sub-bands. Some example of practical systems are quantum well (2D), quantum wire (1D), and quantum dot (0D) [26].

$$\boxed{E = \frac{\pi^2\hbar^2}{2m}\left(\frac{j_x^2}{L_x^2} + \frac{j_y^2}{L_y^2}\right) + E_n} \tag{2.5}$$

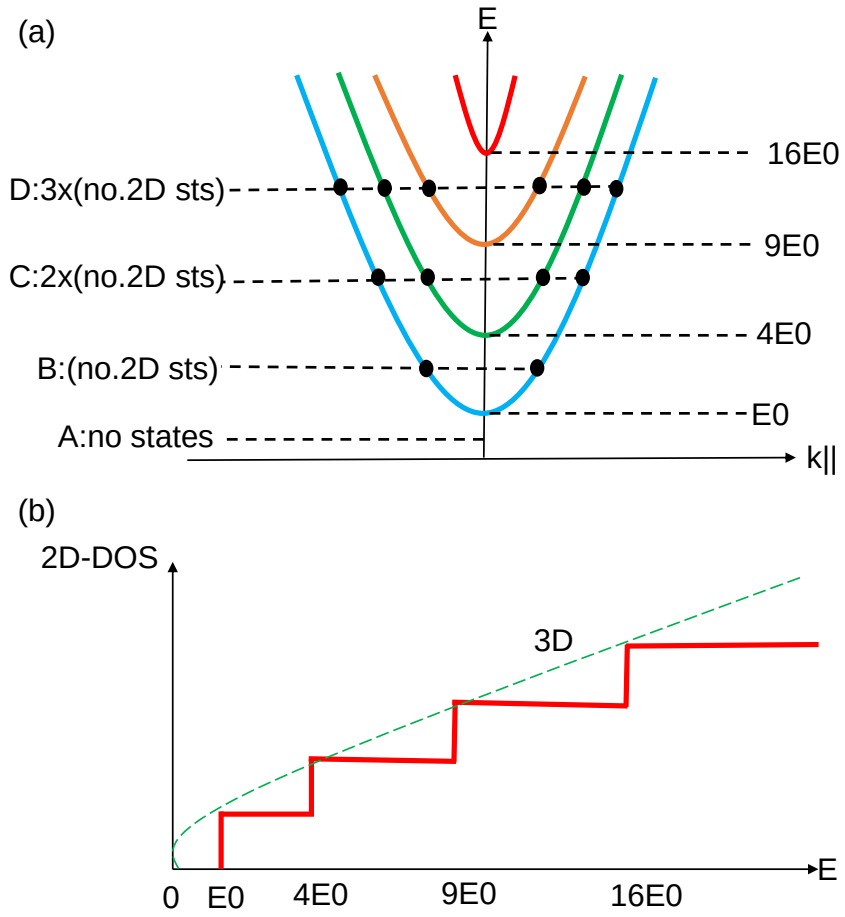

Figure 2.2: **2DEG energy versus wavenumber and density of state for an infinite square well (adapted from [26])**

2.2 Heterostructure Devices

A homojunction is an interface between layers of semiconductor that have the same band gaps. By contrast, a heterojunction is an interface between layers of semiconductor with dissimilar band gaps [30]. A heterostructure is a composition of heterojunctions. We can control the motion of charge carriers in a heterostructure by varying the composition of the semiconductors. This practice is called 'band engineering'. Many of the group III-V materials have been studied for their semiconducting properties. However, only a few of these materials are commonly used in heterostructures, limiting their properties. Therefore, by alloying various compounds, the properties of the heterostructure can be increased. The minimum bandgap and the lattice constant are two very important material properties to consider when alloying materials. Figure (2.3) shows a plot of these two factors for different materials [31].

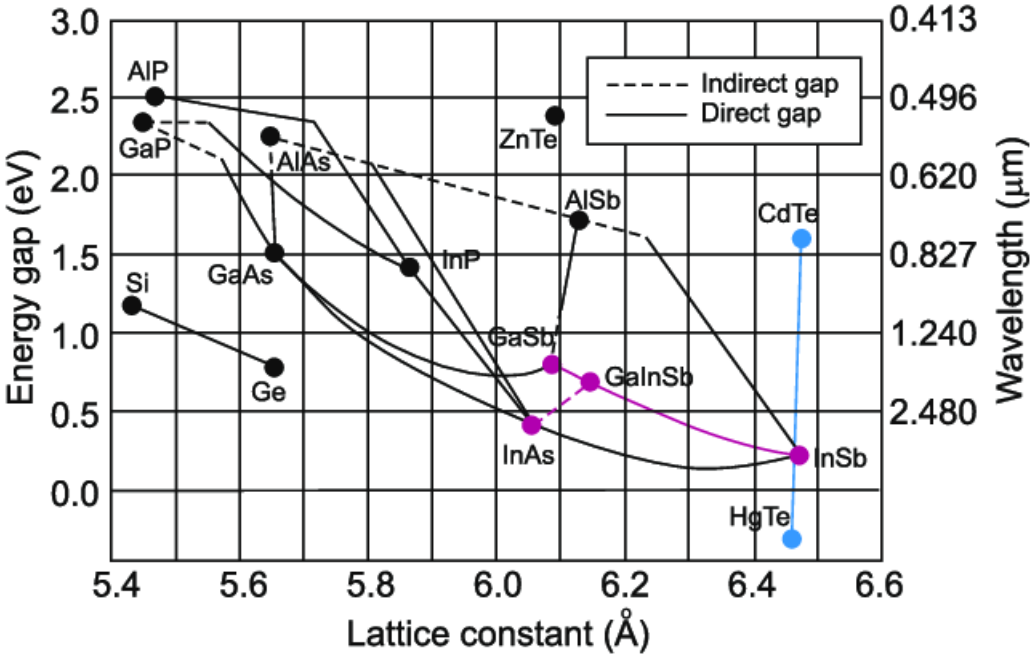

Figure 2.3: **The low temperature energy band gap of semiconductors versus their lattice constants (adapted from [32])**

The active region of the heterostructures is typically at or very close to the interface between two materials. For example, the electrons in a metal-oxide-semiconductor field-effect transistor (MOSFET) move along an interface between silicon (Si) and silicon dioxide (SiO_2). In this case, the SiO_2 is amorphous but the Si in crystalline. These two materials cannot be joined continuously. Thus, electrons are scattered due to the imperfections as they move along the interface. This scattering due to surface roughness, as well as from charged defects in the oxide, keeps the mobility of electrons in a MOSFET below 4 $m^2V^{-1}s^{-1}$ at low temperatures. By contrast, modulation-doped field-effect transistor (MODFET) has a mobility of over 1000 m $^2V^{-1}s^{-1}$ at low temperatures. Such high mobility is the result of the almost perfect crystalline quality of the group III-V heterostructure and the ability to separate carriers from the impurities. Well-developed processes, such as, molecular-beam epitaxy (MBE) and metal-organic chemical vapour deposition (MOCVD) are used to grow the group III-V heterostructures [26] [29] [31].

2.3 2DEG in GaAs/AlGaAs Heterostructure

Two-dimensional material systems are not a natural phenomenon. However, J.R. Schrieffer demonstrated that it was theoretically possible, that under special circumstances, some systems can behave as if they were two-dimensional within very limited energy and temperature intervals. He showed that at the surface interface between a metal and a semiconductor some electrons can move along the surface but not perpendicular to it. Some years later, a research team at IBM realised this idea experimentally [33]. A 2DEG is present at the interface between GaAs and AlGaAs layers. Typically, the Al mole fraction x = 0.3. The band bending diagram of Figure (2.6) shows that the electrons are confined to the interface between the GaAs and AlGaAs by a potential well. The well is formed by the repulsive barrier due to the conduction band offset of about 0.3 V between the two semiconductors and the attractive electrostatic potential due to the positive charged ionised donor in the silicon-doped AlGaAs layer [29]. Furthermore, scattering from the donors is reduced by separating the doped AlGaAs layer from the interface with an undoped AlGaAs spacer layer. This idea was first introduced by Horst L. Störmer [34]. Sub-bands are formed at the interface, due to the imperfect confinement as discussed in Section (2.1). Thus, the energy of the electrons is quantised along the confinement direction, and their motion is restricted to discrete energy levels [29].

2.4 1DEG in GaAs/AlGaAs Heterostructure

The presence of the 2DEG at the interface of a modulation-doped GaAs/AlGaAs heterostructure enables one to restrict the motion of the electrons to a narrow constriction or channel, by selective depletion of the electron gas in some spatial regions. The simplest lateral confinement technique is realised by defining a deep mesa using wet or dry etching, as shown in Figure (2.4a). This technique is still of use for some experimental studies, but it seems to be generally unreliable for channels less than 1 um wide, particularly due to the sidewalls of the structure [29]. The split-gate lateral confinement technique was first introduced by Thornton [35] and Zheng [36] as an alternative to etching, see Figure (2.4b). When a negative voltage is applied to the split-Schottky-gate, the 2DEG region under the gates is depleted of electrons, leaving only a narrow channel un-depleted. Con-

sequently, the motion of the electrons is restricted to this narrow channel. This confinement scheme has the advantage that the channel width and electron density can be varied continuously but not independently by varying the gate voltage [29].

The shallow-mesa depletion (shallow etching) technique in Figure (2.4c) was introduced by Van Houten [37]. This is the second widely used approach to defining a 1D constriction. This method relies on the fact that a 2DEG can be depleted by removing only a thin layer of the doped AlGaAs. The required thickness is a sensitive function of the parameters of the heterostructure material and the details of the lithographic process. This process usually involves electron beam lithography followed by dry etching [29]. Ford [38] introduced a variant to the split-gate technique. This scheme uses a patterned layer of electron beam resist as a gate dielectric to ensure that the separation between the gate and the 2DEG is largest in those regions where the narrow conducting channel must remain after application of a negative gate voltage. The cross-sectional view of this technique is illustrated in Figure (2.4d) [29].

2.5 0DEG in GaAs/AlGaAs Heterostructure

With modern semiconductor technology, we are now able to fabricate particles of metal and semiconductors that are only a few hundred angstroms in size. We can use external leads to control the electrons in these small structures via tunnel junctions [39]. These clusters of atoms are often called 'quantum dot' because electrons are tightly confined in all three spatial dimensions [7]. Like natural atoms, an important property of the QD is that it contains a discrete number of electrons (quantized charge) and has a discrete spectrum of energy levels (quantized energy). Unlike natural atoms, the current through the QD or the capacitance between its leads can vary by many orders of magnitude when its charge is changed by a single electron [39]. Such a device finds application in many areas of quantum technology: quantum metrology, quantum cryptography, and quantum computer to give a few examples.

Conceptually, the difference between a small metal island and the quantum dot is that the Fermi level and hence conduction electron density is much higher in a metallic island. As a result, the energy level spacing between the spatially

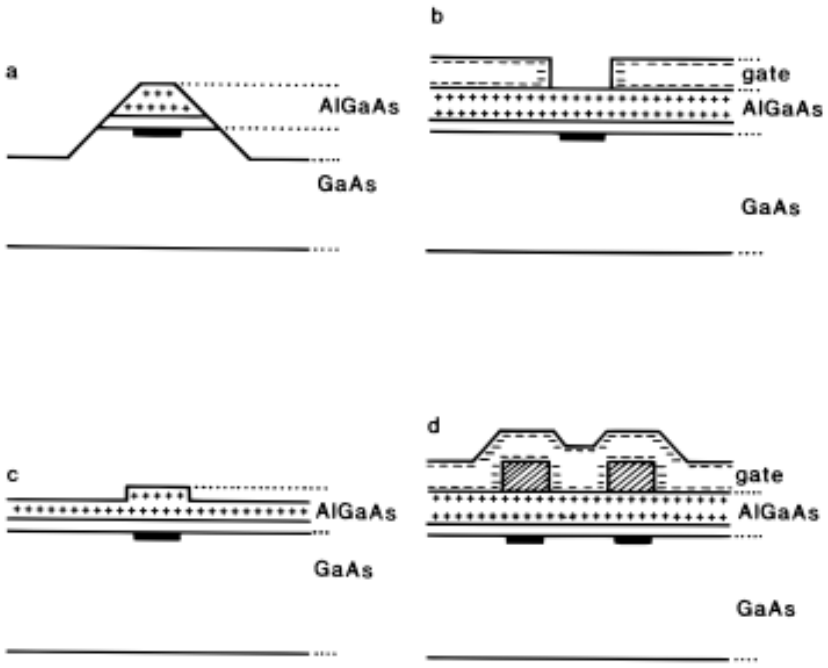

Figure 2.4: **Schematic cross-sectional views of four different ways to define 1DEG channels from a 2DEG GaAs/AlGaAs heterostructure. (a) Deep mesa defined with wet or dry etching, (b) mesa defined using a split-Schottky-gate, (c) mesa defined with shallow etching, (d) mesa defined using the variant of the split-gate having gate dielectric (or resist has shown by the hatched region) (adapted from [29])**

excited electron states is extremely small in metallic islands compared to the quantum dot. The metallic island is typically described by a constant density of state as opposed to the strongly peaked density of state describing the quantum dot. Furthermore, metallic systems contain a larger order of magnitude of electrons, whereas the corresponding number of conduction electrons in a QD ranges from zero to more than a few hundred, similar to natural atoms [7] [39].

A quantum dot can be fabricated by confining electrons in a small region, by employing material boundaries to surround a metal particle with insulators; or one can use electric fields to confine electrons to a small region within a semiconductor [7] [39]. Either technique requires fabricating very small structures accomplished by the techniques discussed in Chapter (4). Figure (2.5) shows typical quantum dot architectures. The most conventional quantum dots are those based on degenerate 2DEG that either form naturally, for example at the interface between

the GaAs and AlGaAs (MODFET) or is induced by an external gate between the interface of silicon and silicon oxide (MOSFET) [7]. Alternatively, quantum dots can be fabricated from either epitaxially grown nanowires or lithographically [7].

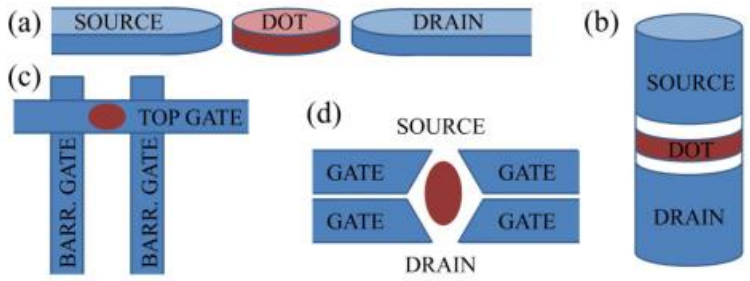

Figure 2.5: **Lateral quantum dot arrangements. The electrons tunnel between the dot and the source and drain. The tunnel barriers isolates the dot from the reservoirs, and it is created either electrically using gates or by different materials such as AlGaAs. (a) Horizontal setup, (b) vertical setup, (c) accumulation gate setup and (d) gate depletion mode setup (adapted from [7])**

2.6 GaAs/AlGaAs Modulation Doped Field-effect Transistor Heterstructure Device

A simple isometric view of a GaAs/AlGaAs device along with its energy diagram is shown in Figure (2.6). Its has an undoped GaAs substrate that forms a heterojunction interface with an undoped AlGaAs spacer layer. The spacer layer is kept very thin to raise the density of electrons at the interface. A 2DEG is formed at this interface as donor electrons situated in a remote layer of n-doped AlGaAs connected to the un-doped spacer layer migrates to the interface between the substrate and the spacer layer. A thin layer of un-doped GaAs or GaAs cap is placed on the surface of the doped AlGaAs layer to prevent oxidation of the AlGaAs beneath it [31].

A metal gate is placed on top of the GaAs cap. The contact between the GaAs cap and the metal gate is called a 'Schottky contact', and the metal piece is called a 'Schottky gate'. The Schottky gate defines the shape (Quantum wire

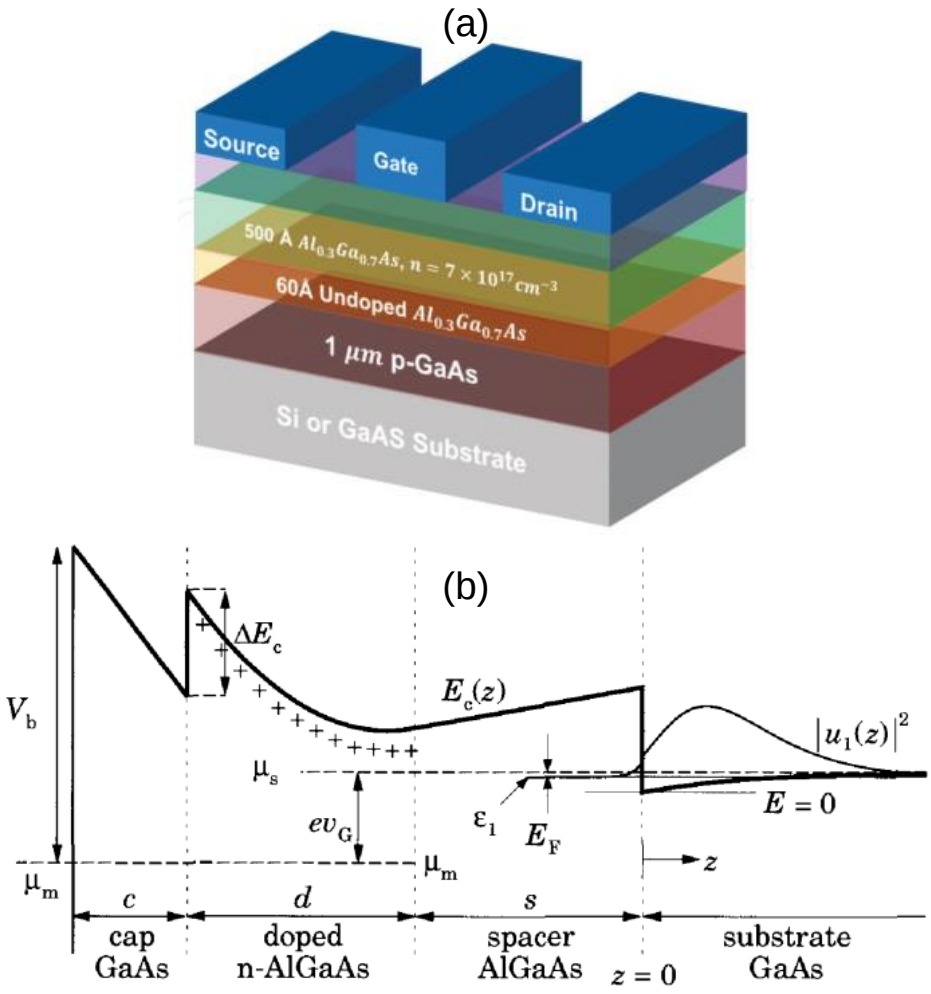

Figure 2.6: **Shows the basic structure of GaAs-based HEMTs and its potential profile. (a) the isometric view of the basic layers, and (b) its potential profile (adapted form [40] and [31] respectively)**

1D and Quantum dots 0D) and carrier density of the 2DEG in the active region. The doped AlGaAs also acts as the insulator between the Schottky gate and the channel. Electron reservoirs such as 'Ohmic gates' are directly connected to the 2DEG channel via 'Ohmic contacts' to make a direct electrical connection between the two. The Ohmic gate makes it possible to bias the device [26] [31] [41].

Chapter 3

The Theory And Realisation Of Single-Electron Pump

3.1 The Operation Principles of Single-Electron Turnstile and Pump

We know that some materials can be electrically charged and exert a force on nearby objects. This phenomenon is termed 'Coulomb interaction'. Close to the end of the 19th century, it was clear that this interaction was caused by a particle called 'electron', carrying a well-defined electric charge [28]. Millikan was the first to observe the discrete nature of electron charge in 1911 [42]. It was evident from the experiment that all electrical charge is an exact multiple of the charge of an electron [7] [42]. In Millikan's experiment, the oil droplets were charged randomly by the ions existing in the air. By contrast, mesoscopic devices can be charged or discharged in a controllable way [7]. Since the interest of this work is on single-electron manipulation, it is important to study the effects resulting from the electrostatic (Coulomb) interaction of electrons both mutually and with an external electrostatic potential [28]. We will see that in small isolated devices, the electrostatic potential energy of a single electron may lead to a blockade or prevention of the transport of electrons through the device. This phenomenon is called 'Coulomb blockade', and the energy to overcome it is called the 'charging energy'. It manifests itself at temperatures such that the charging energy exceeds the thermal energy. In addition to the ratio of these two energy scales, the degree of isolation of the device or the localization of the charge on it is crucial for one to observe this phenomena [28].

3.1.1 Basic physics and energy scales

Figure (3.1) shows the basic concept of single-electronics. A small isolated conductor, which is initially electrically neutral (see Figure 3.1a), does not generate electric-field to its surrounding. Thus, a weak electric force (**F**) can charge the conductor with an additional electron. The island (as is conventionally called in literature) obtains a net charge Q = -e, and it generates an electric field (**E**) to its environment, which repulses any additional electrons (see Figure 3.1b).

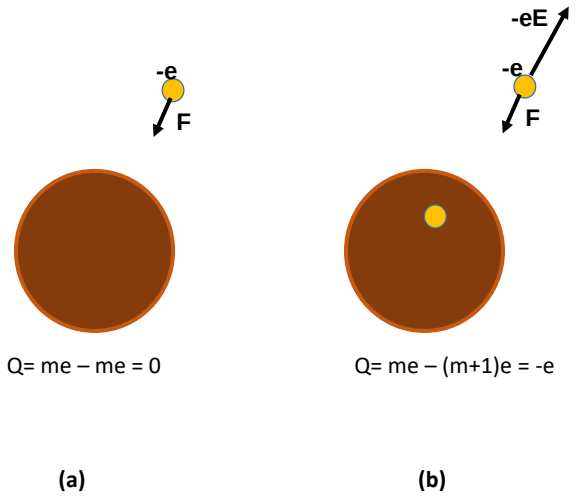

Figure 3.1: **Illustrates the basic concept of single-electron control. (a) a neutral conducting island before the addition of an electron. A weak force can add an electron onto the island. (b) The island has a net charge -*e*, and it creates an E-field which may prevent the addition of the following electrons (adapted from [43])**

This repulsion can be strong in the nanoscale. The theory of single-electron phenomena does not utilize the electric field to measure the strength of this effect, but the charging energy

$$\boxed{E_c = \frac{e^2}{C}} \tag{3.1}$$

where C is the capacitance of the island [43]. When the size of the island compares to the de Broglie wavelength of the electrons, energy quantization becomes significant. In this case, we add the charging and quantization energies, and approximate it by the formula:

$$\boxed{E_a = E_c + E_k} \tag{3.2}$$

where E_k is the quantum kinetic energy of the added electron. Figure (3.2) is the plot of Equation (3.2) as a function of the diameter of the island. One can see, that for 100 nm devices, E_a is dominated by the charging energy E_c and is of the order of 1 meV, i.e. approximately 10 K in temperature units. Since thermal fluctuations (random tunnelling) suppress most single-electron effects unless the following condition is met

$$\boxed{E_a > 10k_BT} \tag{3.3}$$

charging effect experiments have to be carried out in a helium dilution refrigerators. If on the other hand the island size is reduced below approximately 10 nm, E_a approaches 100 meV, and some single-electron effects become visible at room temperature. One can also see that in the size range below approximately 1 nm, electron quantization energy E_k becomes comparable with or larger than the charging energy E_c for most materials; this is the reason islands this small are often termed quantum dots [43].

3.1.2 The orthodox theory

Kulik and Shekhter [44] [45] established the orthodox theory to describe charge transport under the influence of Coulomb blockade. It is a microscopic approach to the behaviour of small, current-biased tunnel junctions [13]. The theory assumes the following [43]:

- *If $E_k << k_BT$ then the confinement energy quantization in a conductor is taken to be continuous. The total charging energy must be $E_a >> k_BT$.*
- *The tunnelling times τ_t through the barrier is small compare to other time scales and is therefore negligible. Practically τ_t is approximately femtoseconds.*
- *If the resistance R of all the tunnel barriers of the non spin degenerate system is much higher than the quantum unit of resistance R_Q:*

$$R >> R_Q, \qquad R_Q = h/2e^2 \tag{3.4}$$

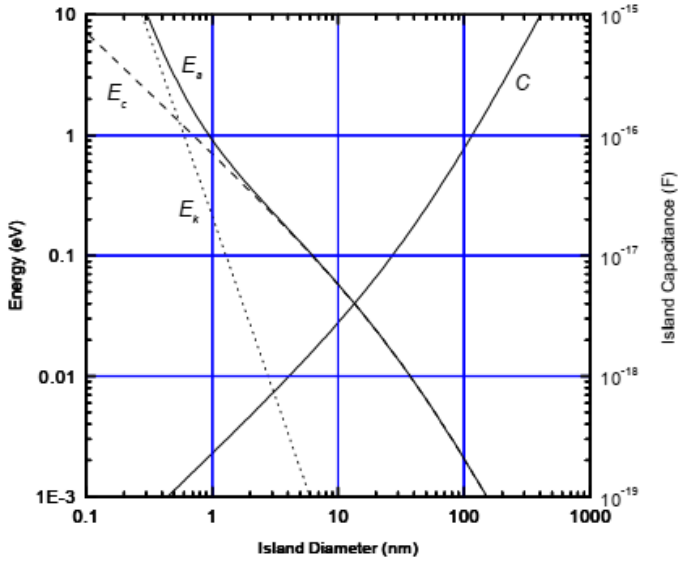

Figure 3.2: **The graph of the total energy of the island E_a (solid line), and its components: charging energy E_c (dashed line) and electron kinetic energy E_k (dotted line), calculated from Equation (3.2) for a simple model of a metallic island. The island is a round 3D ball with free, degenerate electron gas (electron density 10^{22} cm^{-3}), electron effective mass m_0), embedded into a dielectric matrix (dielectric constant $\epsilon = 4$), with 10 per cent of its surface area occupied by tunnel junctions with barrier thickness d= 2 nm (adapted from [43])**

> *then Coherent quantum processes consisting of several simultaneous tunnelling events (co-tunnelling) are ignored. This relation is fundamental for single-electron manipulation as a whole because it ensures the localization of each electron in the island at any instant. Therefore, tunnel barriers with low transparency may effectively suppress the quantum-mechanical uncertainty of the electron location. Only this suppression makes single-electron control possible.*

The main result of the orthodox theory is formulated as follows: "the tunnelling of a single electron through a particular tunnel barrier is always a random event, with a certain rate Γ (i.e. probability per unit time) which depends solely on the reduction ΔW of the free (electrostatic) energy of the system as a result of this tunnelling event. Within the orthodox theory this dependence may be expressed with a universal formula" [43]

$$\boxed{\Gamma(\Delta W) = (1/e)I(\Delta W/e)[1 - exp(-\Delta W/k_B T)]^{-1}} \tag{3.5}$$

where I(V) is the DC I-V curve of the tunnel barrier in the absence of single-electron charging effects. ΔW may be found from the system's electrostatics [43].

Figure (3.3) illustrates the dependency of the tunnelling rate as a function of the electrostatic energy loss of the system given by Equation (3.5). At low temperatures ($k_B T << \Delta W$) only tunnelling events decreasing the systems electrostatic energy (and dissipating the difference) are possible, and their rate is proportional to ΔW. This fact is illustrated by the potential landscape of Figure (3.3); an increase in the bias voltage increases the Fermi level in the source reservoir, and an electron may be able to tunnel into the drain reservoir's empty state [43].

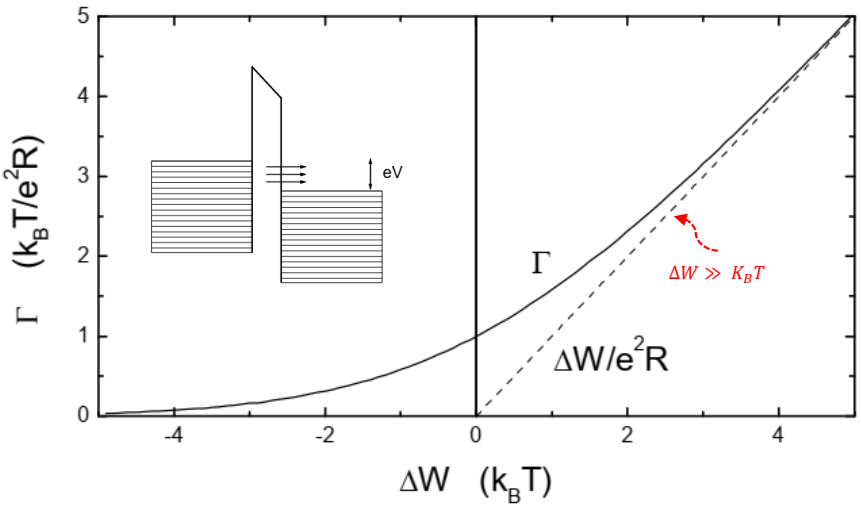

Figure 3.3: **Illustrates the dependency of the tunnelling rate as a function of the electrostatic energy loss of the system given by Equation (3.5). The insert is the energy diagram of a tunnel junction, explaining why the tunnel rate is proportional to the energy loss at low temperatures: the rate is proportional to the number of occupied quantum states in the source, which contributes to the total probability of tunneling into empty states in the drain (adapted from [43])**

Although Equation (3.5) is rather simple, in many situations, several tunnelling events are possible at the same time. Since the orthodox theory describes the probability of a particular outcome, we must use statistical techniques to describe

multiple simultaneous events. Thus, for a system with relatively few islands, we can insert Equation (3.5) into the 'master' equation

$$\boxed{\frac{dp_j}{dt} = \Sigma_j(\Gamma_{jtoi}p_j - \Gamma_{itoj}p_i)} \tag{3.6}$$

which describes the time evolution probability of each state. After we solve this equation for the probabilities, we can then use it for a straightforward calculation of average values and fluctuations of any variable. For more complex systems, we usually have to simulate the random dynamics of the system by Monte Carlo method [43].

3.1.3 Beyond the orthodox theory

As already seen in Figure (3.2) of Section (3.1.1), the confinement energy splitting E_k may become larger than E_c and k_BT for very tiny islands. The orthodox theory can be generalized to include this case as carried out by Averin and Korotkov, who considered a situation where tunnelling is only possible between islands with discrete levels and larger electrodes where electrons still have a continuous spectrum. They showed, that if the tunnelling barriers are not very thin, that is, $h\Gamma < k_BT$, then the situation may again be described with master equations similar to Equation (3.6) of the orthodox theory, but with a different energy dependence of the tunnelling rate to or from a certain quantum level [43]:

$$\boxed{\Gamma(\Delta W) = \Gamma_0[1 + exp(-\Delta W/k_BT)]^{-1}} \tag{3.7}$$

3.1.4 Application of the orthodox theory to single-electron turnstile: From L. P. Kouwenhoven Ph.D. dissertation Chapter 8 [2]

The operating principle of the turnstile is explained schematically in Figure (3.4). It shows the potential landscape of the quantum dot, barriers, and electron reservoirs system for 4 phases of the RF cycle. These phases are labelled (a) to (d). The two barriers are dynamic and oscillate with a phase difference of π relative to each other. In Figure (3.4a), the barriers are in their equilibrium position. The states in the reservoirs are occupied up to the Fermi levels denoted by μ_l and μ_r, which are in non-equilibrium position due to the bias voltage $V = (\mu_l - \mu_r)/e$. The letter N in the dot denotes the level of the electrochemical potential $\mu_d(N)$ when N electrons are localized in the dot (i.e. the minimum energy for the N^{th} electron). Adding an extra electron to the dot would increase the electrochemical potential to $\mu_d(N+1)$, indicated by the $(N+1)$ level in Figure (3.4). The difference $\mu_d(N+1) - \mu_d(N) = e^2/C$ is an electrostatic energy increase, which is represented as an increase of the band bottom [2].

In principle, random tunnelling events could occur where an $(N+1)$ electron could tunnel into the dot from the left reservoir, thereby increasing the Fermi level of the dot from $\mu_d(N)$ to $\mu_d(N+1)$. When the $N+1$ electron tunnels out of the dot, it returns the dot to its initial state. This random oscillation in the number of electrons in the dot alternating between N and $N+1$ can occur when a charge state is enclosed by the electrochemical potentials of the reservoirs $\mu_l > \mu_d(N+1) > \mu_r$, and corresponds to a maximum of the Coulomb oscillation. The typical time for an electron to tunnel through the dot is the RC time, where R is the total tunnel resistance of the two barriers in series. During turnstile operation, these tunnelling events (indicated by the dashed arrows in Figure (3.4a and 3.4c)), will contribute to an unwanted leakage current. One can suppress this leakage current by increasing the resistance of the DC tunnel barriers. When operating the turnstile with DC gate voltages, the suppression of the tunnelling appears as a vanishing amplitude of the Coulomb oscillations [2].

The description of the turnstile operation starts in Figure (3.4a) with N electrons in the dot. The left barrier is at its minimum in Figure (3.4b), and the $(N+1)$ electron has a large probability of tunnelling into the dot at 1/4 of the RF

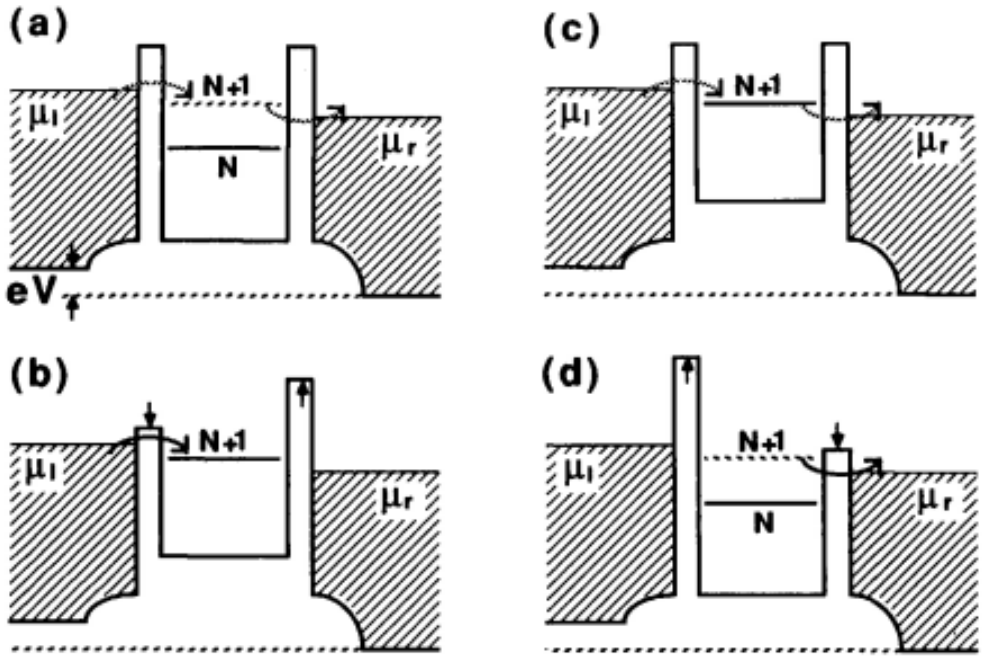

Figure 3.4: **The potential landscape composing of the electron reservoirs, tunnel barriers and quantum dot. The electro-chemical potentials of the left and right reservoirs is denoted by μ_{l} and μ_{r}. $V = (\mu_{\mathrm{l}} - \mu_{\mathrm{r}})/e$ is the bias voltage; N represents the Fermi level μ_{d} of the quantum dot, when N electrons occupy the dot. Figure (3.4a to 3.4d) represent the 4 phases of the RF cycle where the probability for tunnelling is large when the barrier is low (solid arrows), and small for high barriers (dashed arrows) (adapted from [2])**

cycle. At the same time, the right barrier is strongly increased. It suppresses the probability for the $(N+1)$ electron to tunnel out of the dot to practically zero. The barriers return to their equilibrium position again at half the RF cycle in Figure (3.4c). However, unlike Figure (3.4a), one extra electron is localized in the dot. The dashed arrows indicate random tunnelling again. The right barrier is lowered to its minimum value at 3/4 of the RF cycle in Figure (3.4d). So the $(N+1)$ electron has a large probability to tunnel to the right reservoir, as indicated by the solid arrow. Exactly one electron is transported during the cycle from Figure (3.4a to 3.4d), if the wanted tunnel events (solid arrows) have a probability of one, and the unwanted tunnel events (dashed arrows) have zero probability. If we repeat this process with frequency f, then it results in a frequency-determined current $I = ef$. Furthermore, if we increase the bias voltage, such that the number of

charge states in the interval between μ_l and μ_r increases to n, then exactly n electrons will pass through the quantum dot per RF cycle, and the resulting quantized current will be $I = n.ef$. This quantized current corresponds to the current step height $\Delta I = e/RC$ in the Coulomb staircase, however, in the case of the turnstile, the step height $\Delta I = ef$ is determined by the externally applied frequency. The width of the steps in the staircase comes at voltage intervals e/C. Therefore, one can predict an average conductance of the turnstile I-V characteristic proportional to frequency $< G >= ef/(e/C) = fC$ [2].

3.1.5 Application of the orthodox theory to electron pump using one oscillating barrier: Initially proposed in L. P. Kouwenhoven Ph.D. dissertation Chapter 8 [2]

Kouwenhoven [2] observed that an asymmetry in the quantum dot turnstile allowed it to pump a discrete number of electrons at zero bias voltage (i.e. $\mu_s = \mu_D$). That is, electrons are pumped to higher energies by the RF signal applied to a barrier gate. The explanation for this phenomenon and the turnstile form the basis of operation of the single-gate modulated pump realized by Kaestner et al. [21]. Figure (3.5a) shows the potential landscape of the dot with one fixed barrier and one oscillating barrier. The left and right reservoirs are not biased, so electrochemical potentials μ_l and μ_r align. As the left barrier is raised, the conduction band bottom in the dot will be lifted by an amount dependent on the capacitance between the gate and the dot [2].

As the conduction band bottom increases, the electrochemical potential μ_d (indicated by the hatched energy region) of the dot rises above μ_l and μ_r. Thus, the electron in the dot is raised to higher energies, increasing the probability for it to tunnel over the right reservoir. As the left barrier lowers, the dot fills with electrons from the left reservoir because the left barrier height is now smaller. Hence, an oscillating barrier pumps electrons over a fixed barrier. Figure (3.5b) shows the resulting pumped current. This pumping scheme only occurs when we oscillate one barrier around pinch-off and fix the other past pinch-off [2].

Using the above information, Blumenthal et al. [20] demonstrated single-parameter quantized pumping over a barrier tuned into pinch-off using the scheme

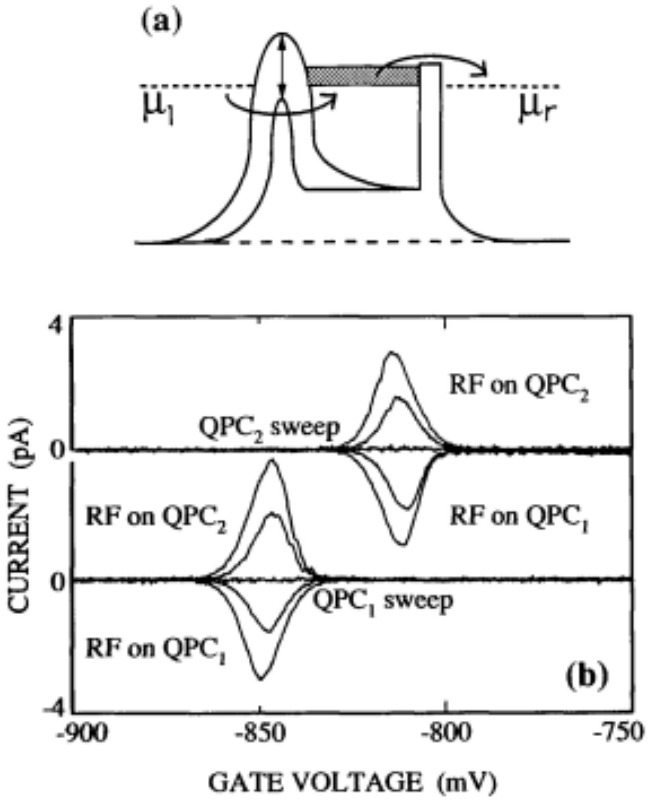

Figure 3.5: **(a) The potential landscape of electron pump using one oscillating tunnel barrier. The electro-chemical potential of the left and right reservoirs μ_l and μ_r are equal. (b) Current vs DC gate voltage on (quantum point contact) QPC1 with a fixed voltage -815 mV on QPC2 (lower set of curves), and vs DC gate voltage on (quantum point contact) QPC2 with a fixed voltage -850 mV on QPC1 (lower set of curves) at zero bias voltage. The curves were measured with RF amplitude of 0 mV (I=0 curves), 8 mV (smaller current peaks) and 11 mV (larger current peaks). The current peak is negative when RF is applied to QPC1, and positive when applied to QPC2 (adapted from [2])**

presented in Figure (3.6). It shows a set of potential landscape corresponding to different phases of the pump cycle. In frame (i), the barrier induced by gate L, and the coupled potential of the dot are below the Fermi level. Frame (ii) illustrates the formation of the populated dot as the barrier, and the dot begins to rise towards the Fermi level. In frame (iii), the dot forms, and the potential of the barrier and the dot are above the Fermi level. Frame (iv) shows that the potential of the left barrier has increased above the potential of the dot and the right barrier (R). The dot potential is above the right barrier potential, increasing the probability for the

electron to tunnel over the right barrier. Therefore, the electrons trapped in the dot by the left barrier are ejected over the right barrier. This process is repeated at some frequency f, resulting in a net current $I_{pump} = (n_c - n_k)ef$, where n_c is the number of electrons captured at point (ii), n_k is the number of electrons kept in the dot at point (iv) and f is the frequency of the RF signals applied to gates L and R.

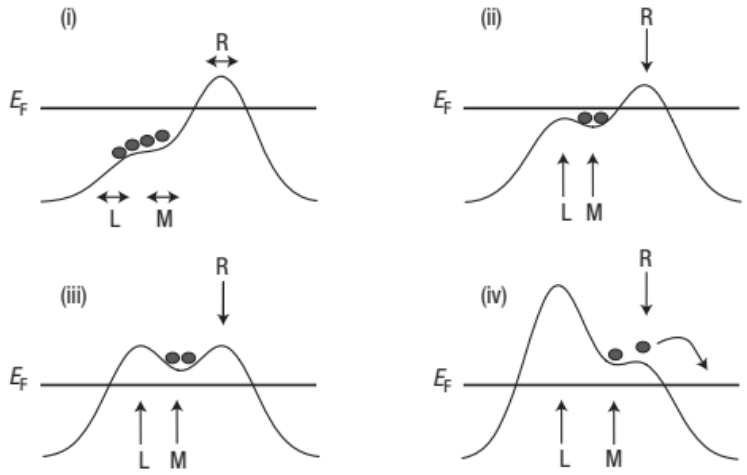

Figure 3.6: **The schematic of the time-dependent potential landscape for electrons transported from the left to right reservoir. The source-drain bias is zero, hence their Fermi levels align. The letters L and R represents the left and right barriers respectively, and the letter M represents the plunger gate. The black dots denote the electrons. Electrons are transported from source to drain in one pump cycle through the phases (i) to (iv) as the barriers are modulated by external voltages indicated by the arrows (adapted from [20])**

Kaestner et al. [21] simplified Blumenthal's et al. [20] idea and realised a single-gate modulated pump. This device has become the research focus of quantised single-electron pump in semiconductor technology due to its simplicity and high-speed operation. Figure (3.7) illustrates its principle of operation. The electrons are pumped periodically from the drain to the source by modulating the left barrier (V_{g1}) with an RF signal superimposed on a fixed DC signal at pinch-off while applying a pinch-off DC signal to the right barrier (V_{g2}). This results in a sequence of confining potential landscapes labelled (i) to (iv) in Figure (3.7a). The average charge captured $< n > = np_n$ is related to the resulting direct current

$I = q_e f < n >$ and the current is a function of the tuning parameters or barrier gate DC voltages, V_{g1} and V_{g2}. For a large-amplitude modulation on V_{g1}, the current shows a characteristic plateau structure at integer levels of $< n >$ shown schematically in Figure (3.7b) [46].

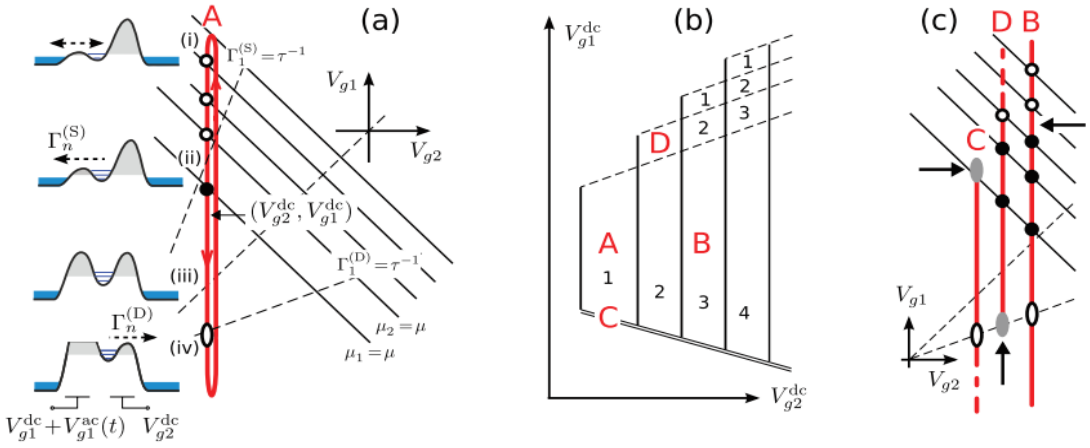

Figure 3.7: **Single-gate non-adiabatic pumping scheme for a tunable-barrier dot leading to robust current quantisation. (a) The potential landscapes at specific time instances during the pump cycle (i) to (iv); the thick red path traces values of the gate voltages controlling the barriers to the source (V_{g1}) and drain (V_{g2}) reservoirs respectively. A conventional two-dimensional pump map of the average pumped current vs the DC voltages of the barrier gates for a relatively large RF modulation. Point A corresponds to the example voltage trace in frame (a). The map consists of three boundaries represented in frame (b) by: the dashed lines, this boundary is called the ejection line, and it is set by incomplete emission at phase (iv). The double line, this boundary is called the capture line, it makes the breaking of the loading phase (i). Finally the vertical line, this boundary is called the onset line, it is set by the outcome of the charge capture process (ii). Pumping paths corresponding to the points B, C and D in the map. The arrows shows the stage of the cycle which limits the number of transferred electrons (adapted from [46])**

In phase (i), multiple electrons are loaded on to the dot as the entrance barrier dips below the source reservoir for a sufficient time to establish near-equilibrium charge distribution on the dot. As the barrier gradually decouples from the source,

in phase (ii), the Fermi level of the dot rises above the electrochemical potential of the source, some electrons at the Fermi energy of the dot back-tunnel into the source reservoir. Figure (3.7a) indicates this with a red contour intersecting a set parallel black lines $\mu_n = \mu$. The open circles are the point of intersection where the barrier is open enough for back-tunnelling to occur, and the filled disks correspond to the point where back-tunnelling does not occur due to low tunnel rates. The source and drain barriers eventually become sufficiently opaque and prevent any further back-tunnelling of the electrons on the dot into the source or drain reservoirs, as shown in phase (iii). After the reliable capture of the electrons, V_{g1} keeps growing more negative, until eventually, the electrons captured in the dot can tunnel into the drain once the corresponding tunnel rates exceed the characteristic opening rate τ^{-1}, as shown schematically by an ellipse marking the emission phase (iv). The dot is then returned to the loading stage (i) through the same sequence of potential shapes (iv) to (i). The electron capture from the drain is prevented by pinching off the exit barrier when the first electron level on the dot is well above the Fermi sea in the drain [46].

The operating principle of the single-gate modulated pump depicted in Figure (3.7a) and marked by point A in Figure (3.7b) remains robust against changes in the RF amplitude and DC offset for V_{g1} as long as the loading (i) and the emission (iv) stages take place properly. Figure (3.7c) shows several pumping trajectories with different DC offsets. In case C, the quantisation plateau boundary along the V_{g1}^{dc} axis is set by insufficient loading. For case D, it is set by incomplete emission. Both of these cases can be seen in Figure (3.7b and 3.7c). For a large RF signal, a larger DC shift on V_{g1} would be required to turn a loading-limited trajectory into and emission-limited one, consequently the length of the quantised plateau along V_{g1}^{dc} (solid vertical lines in Figure (3.7b)) grows with increasing modulation amplitude. The additional steps at the top of Figure (3.7b), such as the one corresponding to case D, results from an emission-rate separation between different charge states at stage (iv). Trajectories A and B are both capture-limited in contrast to C and D. They illustrate that the average number of electrons are loaded, captured and emitted reliably [46].

3.1.6 Decay cascade model

The universal decay cascade model is a tool used to evaluate the performance of the non-adiabatic single-gate modulated pump [24]. It assumes the pump operates as described by Kaestner et al. [46] in Section (3.1.5). Some electrons in the source reservoir get loaded to the dot slow enough, and some electrons back-tunnel as the dot decouples from the source reservoir. We can predict the average number of electrons remaining on the dot using the cascade decay model. The average pumped current $I = q_e f < n >$ is related to the average number of electrons $< n >$. The model then allows one to estimate the minimal achievable quantisation error for a high precision measurement from a low precision measurement from the current-voltage characteristic curve, by extracting device-specific decay rate parameters [24] [25] [46] [47].

The general fitting Equation (3.8) is the double exponential. This model has two fitting parameters, α and δ_n, which are presumed to contain all the information about the parameters of the pumping process. We think of the parameter α as a constant that relates the gate voltage to the height of the confining barrier. The parameter δ_n contains information about the ratio of the tunnelling probabilities of different electrons in the dot, and as well as a Δ_{ptb} term and temperature term, see Equation (3.9) [24] [47].

$$\boxed{< n >= \Sigma_n e^{-e^{(-\alpha(V-V_0)+\delta_n)}}} \tag{3.8}$$

$$\boxed{\delta_n = \frac{\Gamma_n}{\Gamma_{n-1}} + \frac{E_c}{\Delta_{ptb}}} \tag{3.9}$$

Where Γ_n is the back-tunnelling rate of the n^{th} electron in the dot, E_c is the charging energy of the dot, and Δ_{ptb} is the shift of the energy levels in the dot relative to the entrance barrier energy in the time it takes for the tunnelling rate to drop to e^{-1} of its original value.

3.2 Realisation of Single-Electron Turnstile and Pump in GaAs/AlGaAs Heterostructure

To utilise an electron pump as a quantum electrical standard for the Ampere, it must have the following properties: the ability to produce accurate quantised current; it must be simple to realise and operate; it must generate a reasonably high quantised current $I_p > 100$ pA [25] [48]. For the past two and a half decades, many pump technologies were investigated in pursuit of this goal. These included chains of sub-micron normal-metal tunnel junctions [18] [25] [49], the quantum dots driven by a surface acoustic wave [19] and normal metal/superconductor turnstiles [22] [23]. Although 0.015 parts per million (ppm) accuracy has been demonstrated for $I_p = 1$ pA [18], and $I_p = 500$ pA with around 100 ppm accuracy, none of these metallic pump technologies have yet demonstrated the required combination of accuracy and large enough current output [25]. However, the single-gate modulation semiconductor GaAs pump has shown great promise in improving both the accuracy and current magnitude, and it is a simple device. An advantage of this pump is that the quantisation accuracy can be improved with an external tuning parameter [50].

3.2.1 Realisation of single-electron turnstile

In 1991, Kouwenhoven et al. [17] carried out the pioneering experiment-that showed the quantisation of current or single-electron transport in 2DEG GaAs/AlGaAs semiconductor heterostructure. Figure (3.8a)shows a scanning electron microscope (SEM) image of the Schottky gates geometry patterned on top of a GaAs/AlGaAs heterostructure with a 2DEG about 100 nm below the surface. The grown 2DEG has mobility of 2.3 x 10^6 $m^2V^{-1}s^{-1}$ and an electron density of 1.9 x 10^{15} m^{-2}. The brown disk denotes the quantum dot; it is delimited by the finger gate, the two split gates (forming the isolating tunnel barriers) and the plunger gate. Kouwenhoven operated this device as a 'turnstile'.

Kouwenhoven et al. [17] performed his experiment inside a dilution refrigerator at a temperature of 10 mK and in zero magnetic fields. He applied negative direct current (DC) voltages to all four gates. Furthermore, he coupled alternating current (AC) voltages with a phase difference of 180° and a frequency of 10 MHz to the split gates. These RF signals will cause the tunnel barriers induced by the

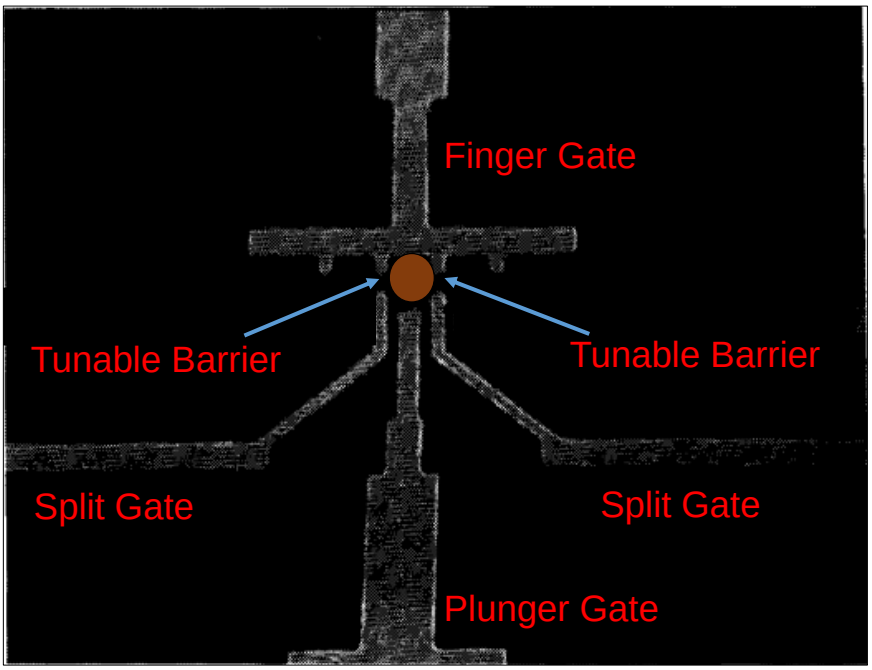

(a) SEM Image of gate geometry denoting: the finger gate, the two split gates, the plunger gate, tunable barriers and quantum dot

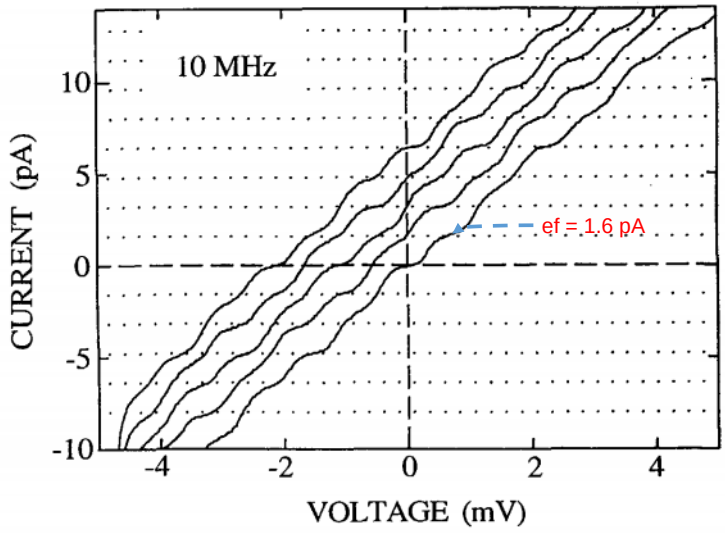

(b) Main figure: I-V characteristics when two phase shifted RF signals are applied with a frequency of 10 MHz, showing current plateaus at integer multiples of ef (dotted lines). The curves correspond to different center-gate voltages and are offset for clarity by an integer times ef.

Figure 3.8: **Sample layout and I-V curve of Kouwenhoven's pioneering experiment (adapted from [17])**

split gates to oscillate between the quantum dot and the wide 2DEG region. This is the main difference between Kouwenhoven's work compared to the work done previously on metallic system. Lastly, he applied a source-drain bias between the electron reservoirs and measured the current in a two-terminal configuration. Figure (3.8b) shows the main result of the experiment. It illustrates the measured I-V characteristic of the turnstile. The I-V curves have current plateaus at integer multiples of ef, demonstrating that a discrete number of electrons pass through the semiconductor quantum dot with each RF cycle. However, the resulting current is only $ef = 1.6$ pA; it is too small for practical application as a current standard.

Although the above experiment was groundbreaking, the accuracy of the quantized current still needed improvement. Kouwenhoven attributed the error to unwanted tunnelling events, which caused smearing or disappearance of the plateaus. Nagamune et al. [51] improved on Kouwenhoven's work by proposing a different quantum dot design. He fabricated the structure in Figure (3.9a) and (3.9b) using a combination of mesa etching and gate formation techniques. It confines the electrons in an etched sub-micron 1DEG nanowire. The two barrier gates crossing the wire depletes the electrons beneath them to form a quantum dot between the gates. This results in a small quantum dot containing less than ten electrons [51]. Such a quantum dot has a large charging energy, which is an advantage for studying charging effects because a large charging energy dominates the thermal energy at low enough temperatures. Thus, unwanted tunnelling events is strongly suppressed, and the current quantisation improves. Nagamune et al. [51] used the same experimental setup as Kouwenhoven et al. [17]. Figure (3.9c) shows the measured I-V characteristic. The current steps achieved in this device are much more distinct than those obtained with the split-gate device in [17]. This result supports Kouwenhoven's claim. That is, Nagamune et al. [51] reduced the error of the quantised current by suppressing the unwanted tunnelling events. The magnitude of the steps is close to $ef = 1.6$ pA, which is in good agreement with the transfer of a precise integer number of electrons per turnstile cycle [17] [51] .

3.2.2 Realisation of Single-Electron pump

So far, both Kouwenhoven et al. [17], and Nagamune et al. [51] operated their device as a turnstile. To operate the device as a turnstile, the energy of the $(N+1)$

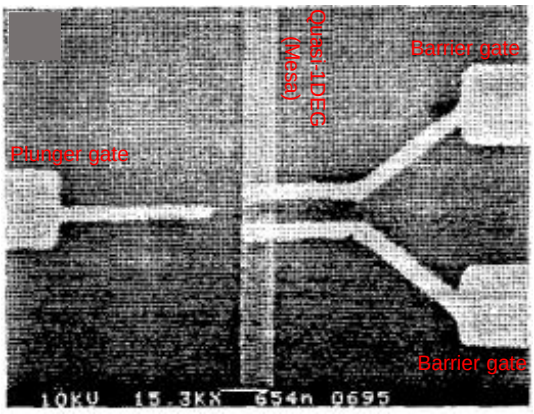

(a) SEM Image of Gate geometry

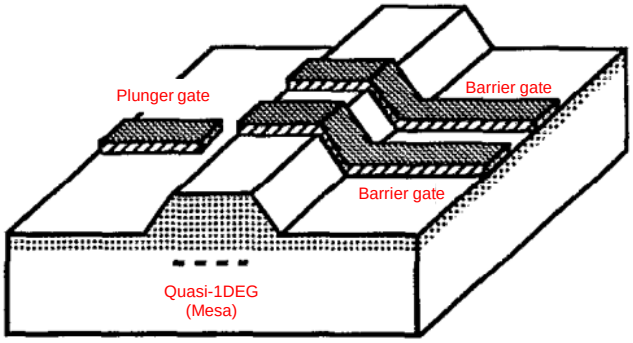

(b) A schematic illustration

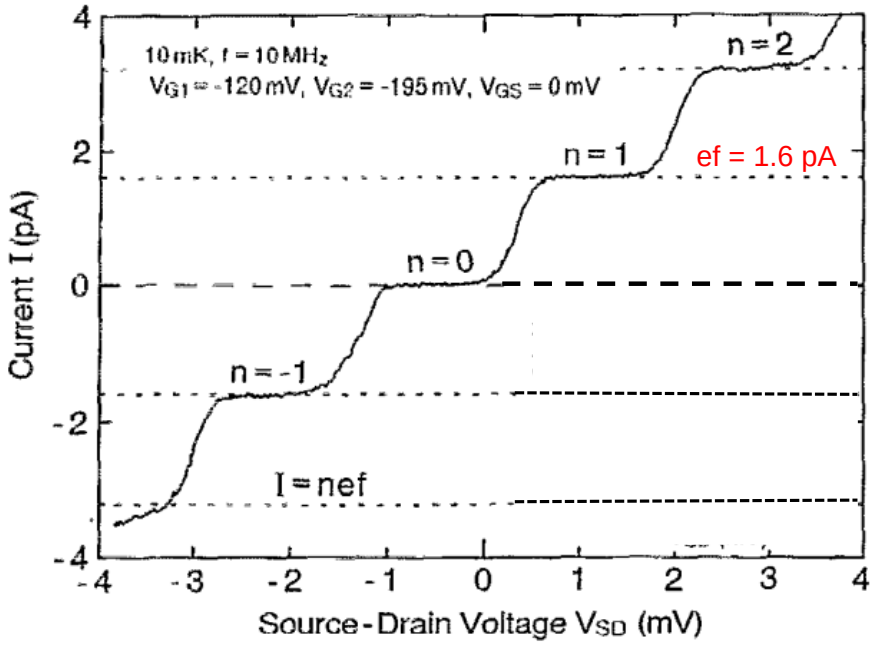

(c) The I-V curve

Figure 3.9: **Sample layout and I-V curve for Nagamune's experiements (adapted from [51])**

electron must be confined to the bias window, $\mu_S > \mu_{N+1} > \mu_D$. That is, the electrochemical potential of the source and drain must be asymmetrical, and the Fermi level of the dot must be in between the Fermi levels of the source and drain. This constraint is difficult to ensure for large RF modulation on the barrier gates because of the crosstalk between the barriers and the dot [2] [46]. Ideally, the barriers should be modulated independently of the dot potential, which should

be kept fixed throughout the turnstile operation cycle [46]. Kouwenhoven et al. [17] addressed this challenge by applying two RF signals with a phase difference of 180° to the barrier gates to compensate for the cross-couping between the potential of the barriers and the dot [46]. Kouwenhoven [2] demonstrated that the same device in Figure (3.8a) could also operate as a 'pump' without the need of a source-drain bias (i.e. $\mu_s = \mu_D$) if the right kind of asymmetry in the modulation amplitude and phase is applied to the barrier gates. Figure (3.10) illustrates a series of I-V curves for the same device as in Figure (3.8a) operating as a pump. The modulation amplitude on the barrier gates, the relative phase and the voltage on the plunger gate C are adjusted so that the plateaus from $-5q_ef$ to $+5q_ef$ appear around zero bias voltage [2] [46].

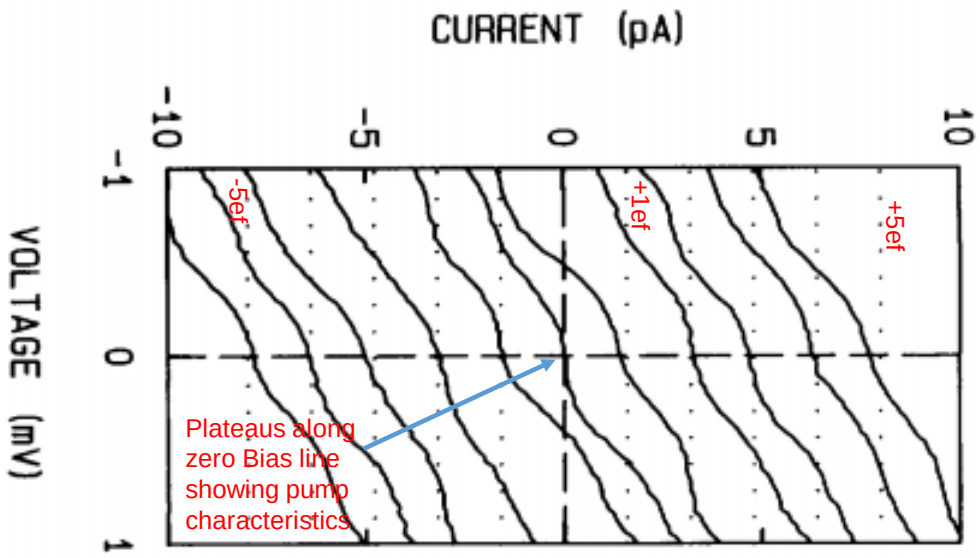

Figure 3.10: **I-V characteristic for a similar device as shown in Figure (3.8a) with settings for voltage on gate C, RF amplitudes and phase differences such that current is quantised at zero bias voltage (adapted from [17])**

It took over a decade before researchers were aware of the importance of Kouwenhoven's [2] work on the single-electron pump. This work would eventually lead the way to the realisation of the single-gate modulation pump. Surprisingly, at that time, the focus on single-electron sources based on gallium arsenide moved towards the idea of using SAWs [19] to drive the single-electrons in a one-

dimensional channel [7]. This was until the seminal work by Blumenthal et al. [20] that first demonstrated single parameter pumping over a fixed barrier tuned into pinch-off in the quantised regime. He fabricated (see Figure 3.11) a 700 nm mesa on a silicon-doped GaAs/ AlGaAs heterostructure to localise the electrons to a 1DEG channel, similar to Nagamune's et al. [51] device. Three surface finger gates separated by about 250 nm overlap the chemically etched wire to induce a potential landscape along its longitudinal direction. The gates are labelled L (which is the barrier to the source), M (which is the tuning parameter gate or plunger), and R (which is the barrier to the drain). The negative potential on gates L and R induces the quantum dot in the wire. Gate M modulates the charge distribution in the dot. Blumenthal et al. [20] achieved quantised charge pumping by applying a 180° phase-shifted sinusoid superimposed with a DC signal to gates L and R. He applied a much larger RF amplitude to gate L than gate R to ensure that the drain barrier is in pinch-off during the pump cycle. He then simultaneously applied a DC voltage to gate M. Figure (3.11) shows that the quantised current plateaus are in agreement with the exact value of one electron per cycle. The value of the current is 87.64 pA at 547 MHz with one standard deviation (1σ) relative uncertainty of 10^{-4} at a bath temperature of 300 mK [20]. This result encouraged further development in using GaAs/AlGaAs pumps as a high-accuracy current standard.

Kaestner et al. [21] subsequently realised a simplified version of the single-gate modulation pump demonstrated by Blumenthal et al. [20]. The device architecture is similar to the one used in [20], but Kaestner et al. [21] only used two gates instead of three, and he only modulates one of the two gates. Figure (3.12) shows the device geometry and its simplified electrical connections. The device has three (although only two were used) metallic finger gates crossing a 1DEG nano-wire etched from an n-type GaAs/AlGaAS 2DEG. Kaestner et al. [21] applied a DC signal to gate 1 and 2, while exclusively modulating gate 1 with an 80 MHz sinusoidal signal. Figure (3.12) shows the I-V trace of the quantised current at a base temperature of 300 mK. One can see up to four quantised plateaus. The advantage of this pump is its simplicity. The simplicity of this scheme has stimulated most of the recent development of single-gate modulation pumps in GaAs/AlGaAs devices [7] [46], and researchers have been working on improving it through various means for high speed, and precision pumping [46]. The remainder of this review will focus on the improvement of the quantised current using this

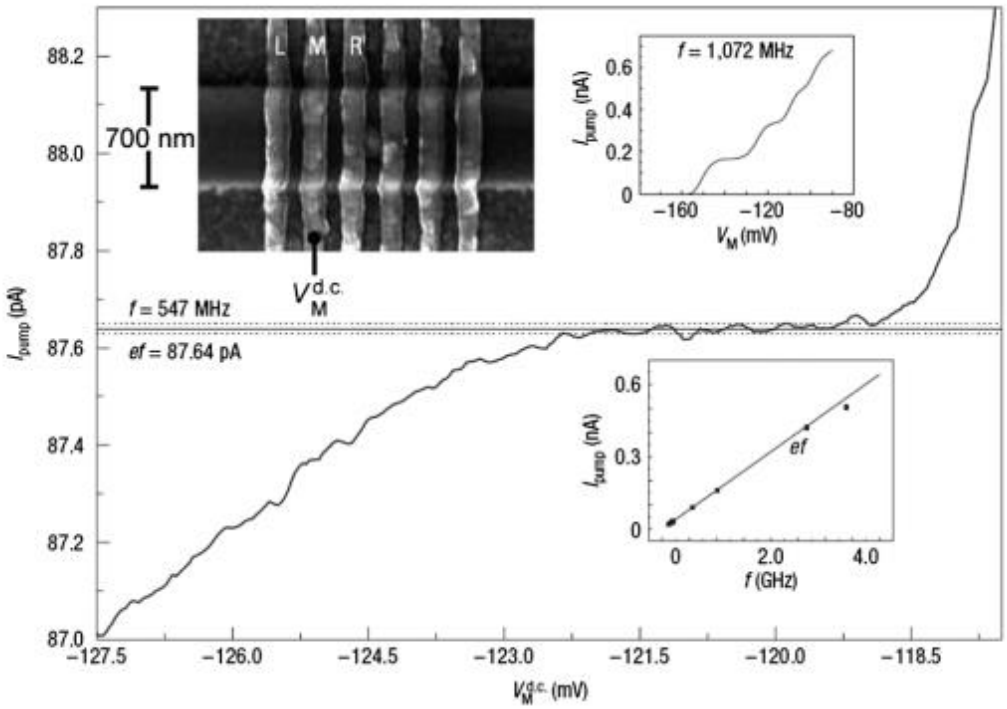

Figure 3.11: **Current plateau in the electron pumping experiments as a function of the middle-gate voltage at 547 MHz operation frequency. The dashed lines show $\sigma = \pm$ 10 fA uncertainty in the electrometer calibration. The top left inset shows the device used as the electron pump. The top right inset shows current plateaus at 1 GHz pumping frequency and the bottom inset shows the pumped current as a function of the operation frequency (adapted from [20])**

scheme.

Maire et al. [52] studied the effects of low-frequency noise on the quantised current of the single-gate modulated pump. To do this, he included a fast-Fourier-transform analyser to the pump (see Figure 3.13a) to monitor the noise on the current. He aimed to investigate whether the quantised current predominantly depended on the driving frequency of the pump. Figure (3.13b) shows the corresponding pumped current spectra of the sample at 400 mK and driven with a 400 MHz RF signal with an amplitude of 1dBm. It shows three current noise spectra corresponding to plateaus 2, 1.6 and 1 at different entrance voltages U1 = -125

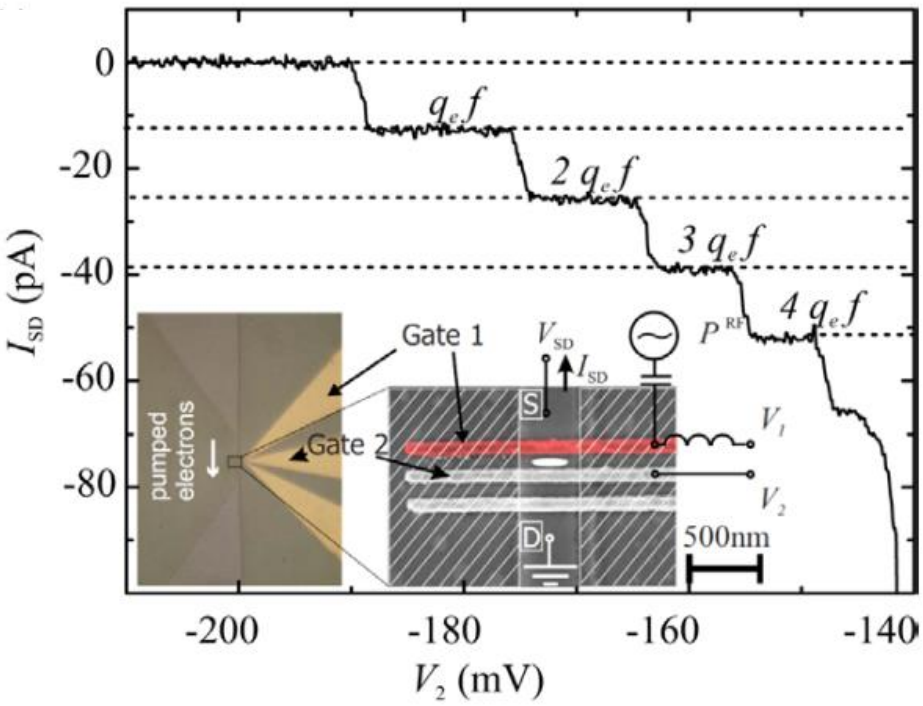

Figure 3.12: **Single-gate modulated quantised current vs the DC voltage applied to gate 2 measured for the device shown in the insets (adapted from** [21] [46])

mV, -103 mV and -91 mV respectively, and at a fixed exit voltage U2 = -86 mV. The red horizontal lines show the noise power averaged over the range of 5-15 kHz. The $\frac{1}{f}$ noise drops at 1 kHz already below a significant level and the current noise power S is frequency independent for f greater than 2kHz. Furthermore, Figure (3.13b) plots the average noise power as a function of the gate voltage U1. As one can see, the noise power is strongly suppressed on the current plateaus (at (a) and (c)) compared to the non quantised regions (at (b)) of the pumped current. This is in agreement with the spectra of Figure (3.13c). This is a strong indication of true quantised current. Maire et al. [52] then concluded that the single-gate modulated pump has very good low-frequency stability. He estimated the error of the quantised current to be about four per cent.

Kaestner et al. [53] investigated the robustness of the quantised current of the single-gate modulated pump against RF power. The experimental conditions were the same as in [21]. Figure (3.14) shows three pump maps at increasing RF power of -29 dBm, -26 dBm and -24 dBm, at a driving frequency of 500 MHz. One

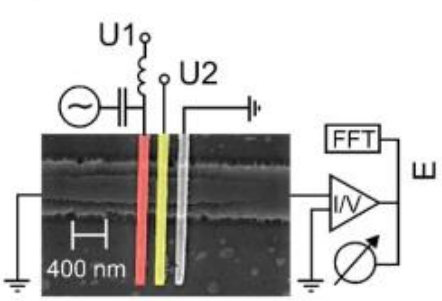

(a) Single-gate modulated pump with a fast-Fourier-transform analyser

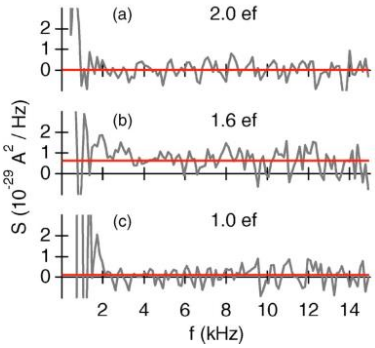

(b) Three current noise spectra corresponding to plateaus 2, 1.6 and 1 at different entrance voltages U1 = -125 mV, -103 mV and -91 mV respectively, and at a fixed exit voltage U2 = -86 mV.

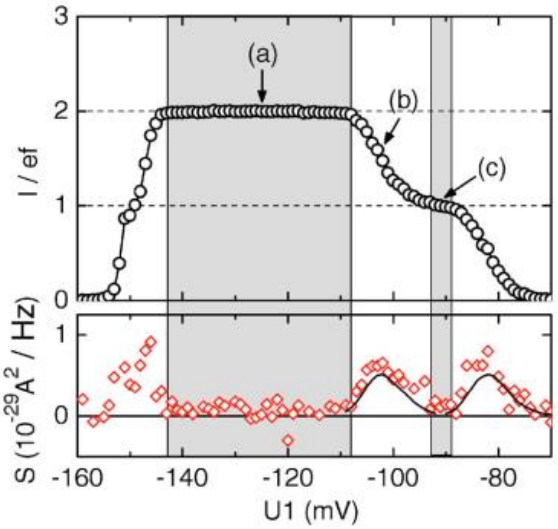

(c) average noise power as a function of the gate voltage U1

Figure 3.13: **Single-gate modulated pump with fast-Fourier-transform analyser to monitor the noise on the quantised current. (a) Sample, (b) three spectra vs U1 and U2, (c) average noise power as function of U1 (adapted from [52])**

can see plateaus of different qualities around the values of $I = \mathrm{n}ef = \mathrm{n}80$ pA for $\mathrm{n} = 1, 2, 3, 4$, where on average n electrons of charge e per cycle are transported. The plateaus become pronounced and extended along the entrance gate voltage (V_1) with increasing RF power. The length of these plateaus is a measure of the robustness of the quantised current along the entrance voltage (V_1). Here the robustness is measured as the range of entrance voltages, along which the number of loaded electrons equals the number of unloaded electrons ($\mathrm{n}_u = \mathrm{n}_l$). Therefore, the pump map of P = −24 dBm, the third graph from the top is more robust than those of P = −26 dBm and P = −29 dBm. Kaestner [53] calculated the quantised current value to be $I = 80 \pm 0.5$ pA at the flattest part of the first plateau for P = −24 dBm at $V_1 = -200$ mV. Furthermore, the bottom of Figure (3.14) shows how the width or robustness window of the first plateau increases along the entrance voltage from P = −28 dBm to P = −23 dBm at an exit voltage of $V_2 = -230$ mV. The case of P = −23 dBm has the most robust first plateau. Kaestner et al. [53] concluded that the robustness and simplicity of the single-gate modulated pump makes it a potential practical module as a scalable quantised current source.

Another way to investigate the robustness of the quantised current is to use a magnetic field. Wright et al. [54] observed that the quantised current is also robust along the exit voltage (V_2) against an applied magnetic field. Additionally, the introduction of the magnetic field also improves the accuracy of the plateaus. Figure (3.15) shows the sample measured at a temperature of 50 mK, with a -12 dBm and 306.7 MHz RF signal applied to the entrance gate (V_1). The plot on the left of Figure (3.15) shows the quantised current in zero magnetic fields. The plot on the right of Figure (3.15) shows that the plateaus elongated along the exit voltage as the magnetic field changes from 0 T to 2.5 T. This elongation of the plateaus is an indication of the robustness of the quantised current along the exit voltage as a function of the applied magnetic field. Wright et al. [54] also showed that the accuracy of the plateaus in Figure (3.15) improved by about 55 per cent at 2.5 T. These results are crucial because it provides a technique to improve the accuracy of the quantised current.

Moreover, he later applied his findings to the case of two pumps operating in parallel and subjected to a magnetic field [55]. Figure (3.16) left shows a SEM image of the device, arranged in such a way to eliminate cross-talk and capaci-

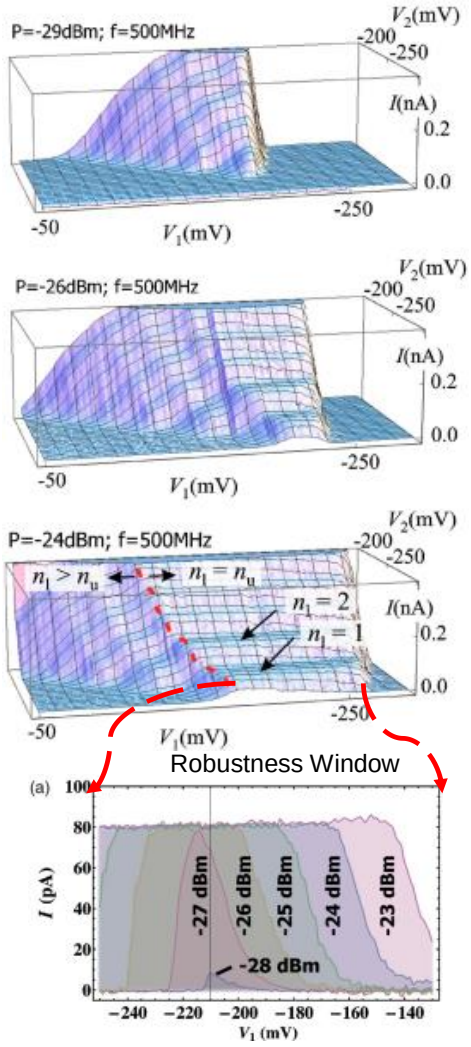

Figure 3.14: **Single-gate modulation pump maps showing the increase in robustness of the quantised current with increasing RF power (adapted from [53])**

tive coupling between the two pumps. Figure (3.16) right presents the resulting quantised current at 40 mK, 5T and 340 MHz RF signal. Wright [55] tuned both pumps to the first plateau to produce a total current of 108.95 pA ($2ef$), and claimed that the plateau was invariant in the exit voltage to better than 20 ppm [55].

Shortly after, Kaestner et al. [56] conducted further studies on two pump samples in high magnetic fields. Figure (3.17) shows the measured results of device 1, at a temperature of 40 mK and RF power of -16 dBm at 500 MHz. It is evident

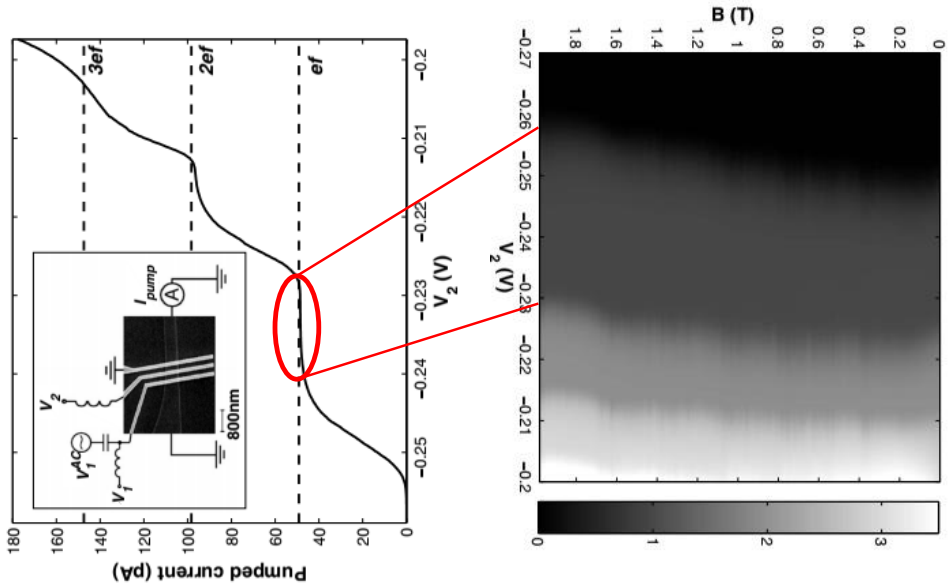

Figure 3.15: **Robust quantised current along the exit voltage due to the application of magnetic fields. The graph on the left shows the quantised current plateau as a function of the exit gate voltage with zero magnetic field. A SEM image of the device is inserted in the figure. The figure on the right shows the pump map of the quantised current as a function of the exit gate voltage and magnetic field. The red circle on the left and the red lines joining the left and right figure indicates how the first plateau elongates along the exit gate voltage with increasing magnetic fields (adapted from [54])**

from both Figure (3.17a and 3.17b) that the accuracy and robustness of the quantised current improve with increasing magnetic field (up to 3 T). Furthermore, he measured device 2, at T = 300 mK, with RF power of -23 dBm at 500 MHz. Figure (3.18a and 3.18b) shows the results of device 2, and the dependence of the quantised current on the magnetic field at B = 0 T and B = 10.2 T respectively, as a function of the entrance and exit gate parameters. The top left figure shows the pump map for plateaus 1 to 4 at B = 0 T, while the top right figure shows the pump map for the 1st plateau at B = 10.2 T. The first plateau in is fitted for both the B = 0 T and B = 10.2 T case, see bottom of Figure (3.18). When we compare the quantised currents at these magnetic fields, and selected values of V_1 at -200 mV and -165 mV, we see clearly that the plateau of B = 10.2 T is more robust and accurate along the exit barrier due to the high magnetic field.

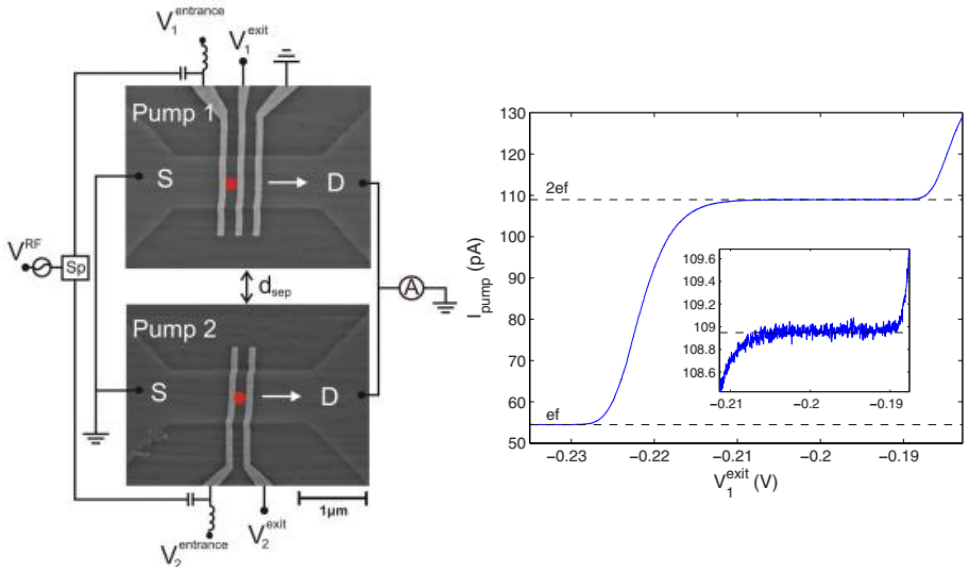

Figure 3.16: **Illustrates single-electron parallel pump operation in single-gate modulated scheme. The picture on the left is the SEM image of the device with all the electrical connections. Both devices are driven with the same RF signals. The quantised current graph on the right shows that when both pumps are operated in parallel the resulting current for the first plateau is $2ef$ (adapted from [55])**

Giblin et al. [50] probed the accuracy of the single-gate modulation pump a bit further. He compared its quantised current to a reference current derived from the primary electrical standard, which has a relative accuracy of approximately 10^{-5}. A key feature of his experiment is the reference current I_R, which he generated by applying a linear voltage ramp to a low loss capacitor. This current is traceable to the primary maintained standard of capacitance, voltage and time, and it has a relative systematic uncertainty of 15 ppm. He measured the samples at 30 mK, with an RF frequency of 340 MHz, and a magnetic field of 5 T. Figure (3.19ia) shows the resulting low-resolution quantised current of samples A and B versus exit voltage (V_{GD}). As expected, both samples exhibited robust plateaus along V_{GD} due to the application of the magnetic field. The current obtained for sample A is $I_o = 54.474$ pA $\pm$ 15 ppm 1σ. Figure (3.19iia to 3.19iid) shows the quantised current of sample B as a function of the entrance voltage (V_{GS}), exit voltage (V_{GD}), bias voltage (V_B) and RF power (P_R). Figure (3.19iiie) presents the average values of the current for the two data sets of sample A and four data sets of sample B. From this figure we notice that the difference in current between

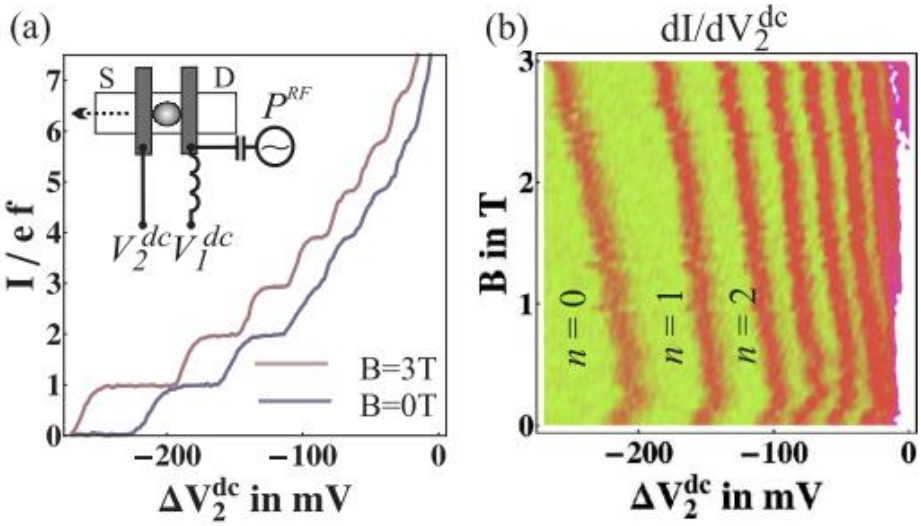

Figure 3.17: **(a) Normalised pumped current by ef vs the V_2. The insert is the schematic of the device. (b) The numerical derivative of the pumped current in arbitrary units as a function of applied B-field and V_2. The measurements were performed on device 1, at 50 MHz, base temperature of 40 mK and RF power of -16 dBm (adapted from [56])**

samples A and B is $(-5 \pm 2.5)10^{-6}$, this indicates possible sample dependence error at the ppm level, which is limited only by the random uncertainty.

Up until now, we have only reviewed single-gate modulated pumps that were driven by a sinusoidal signal. However, we are not limited to this type of waveform. It is possible to design an arbitrary waveform to drive the pump, and Giblin et al. [25] did just that. He was able to extend the operating frequency of the pump by using an arbitrary waveform that took into account the time-dependent electron tunnelling dynamics. We use Figure (3.20) as a visual aid to understand how he designed the waveform. Figure (3.20a) shows a SEM image of the sample. Usually, we modulate the entrance gate with a sinusoid like the one in Figure (3.20c). As one can see, it contains numbered dots of different colours. The numbered points indicate approximately, the four stages in the pump cycle: the loading, back-tunnelling, trapping, and ejection, corresponding to numbers 1, 2, 3, and 4 respectively. The schematic diagram of Figure (3.20b) shows four potential landscapes created by the entrance and exit gates corresponding to the four points representing the pump cycle. An electron is pumped from the source to drain in

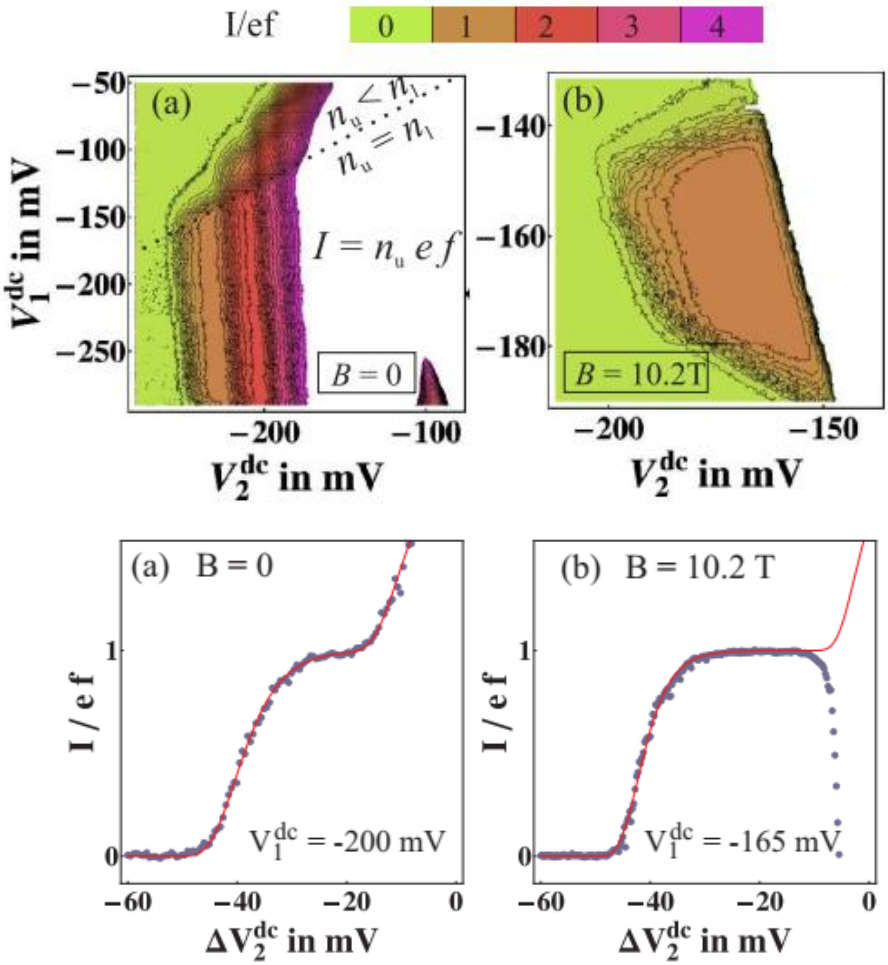

Figure 3.18: **Top diagram (a) shows the normalised pump map at B = 0 T, while (b) shows the pump map of the first plateau as it extends in exit voltage at B = 10.2 T. Bottom diagram (a) shows the normalised pumped current with zero B-field, while (b) shows the elongation and robustness of the pumped current in exit voltage at B = 10.2 T (adapted from [56])**

one pump cycle.

Giblin et al. [25] based the design of the arbitrary waveform on the following assumptions: firstly, by looking at the sinusoid in Figure (3.20c), we see that once we reliably capture the electron(s), point 3 (potential number 3 in Figure 3.20b), then most of the pump cycle time is used to eject (point 4) the electron(s) and load (point 1) other(s). That is, one can use this dwell time to operate the pump

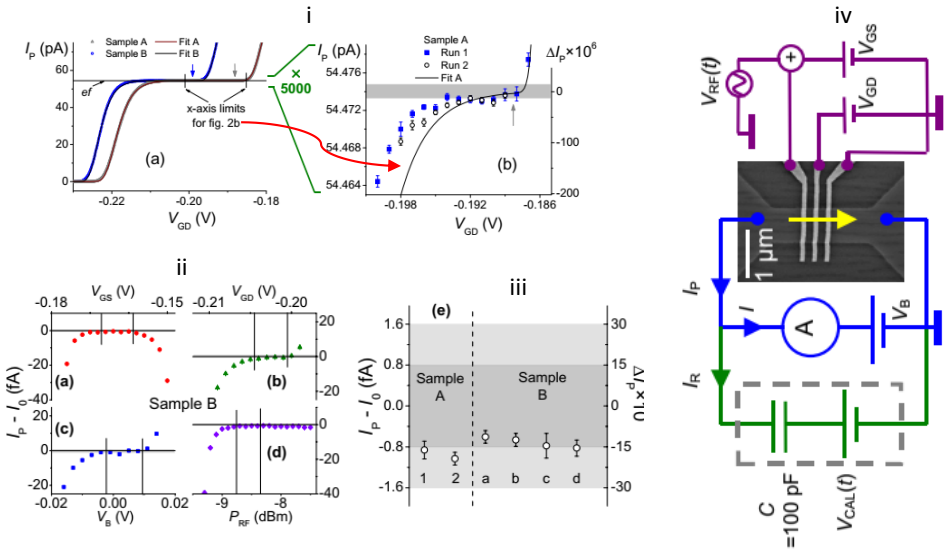

Figure 3.19: **(ia) Shows the low resolution quantised current versus exit voltage (V_{GD}) data fitted with the decay cascade model for samples A and B. (ib) Shows high resolution quantised current for sample A, showing data for two measurement runs and the fitting. (iia–d) Quantised relative to $I_0 = ef = 54.47400$ pA for sample B, as a function of four control parameters, V_{GS}, V_{GD}, V_B and P_{RF}. (iiie) presents the average values of the current for the two data sets of sample A and four data sets of sample B. (iv) Schematic diagram of the measurement (blue), reference current (green) and gate bias (purple) circuitry, incorporating a SEM image of a device (adapted from [50])**

at a faster rate. Therefore, after capture, we can raise and lower the entrance barrier quicker. The second assumption deals with capturing the electron reliably from points 1 to point 3. We know that the error rate at high frequency relates to the speed of raising the entrance barrier during the capture phase (point 1). Thus, we must raise the entrance barrier slowly enough during the capture phase to allow the necessary back tunnelling and reliable capture of the electron(s) to occur. Following these assumptions, Giblin et al. [25] designed an arbitrary waveform shown in Figure (3.20d) that retained the shape of a sinusoid during the capture phase, and contained the shape of a trapezoidal waveform after the capturing phase. The frequency of the sinusoidal segment is a fifth of the frequency of the pulse waveform. Therefore, the entrance gate is slowed down during capture by a factor of five. Thus, the error does not increase too much as the frequency of

the pulse is increased [25]. That is, a pulse at frequency f should have the same characteristics as a sinusoid at $f/5$ [25].

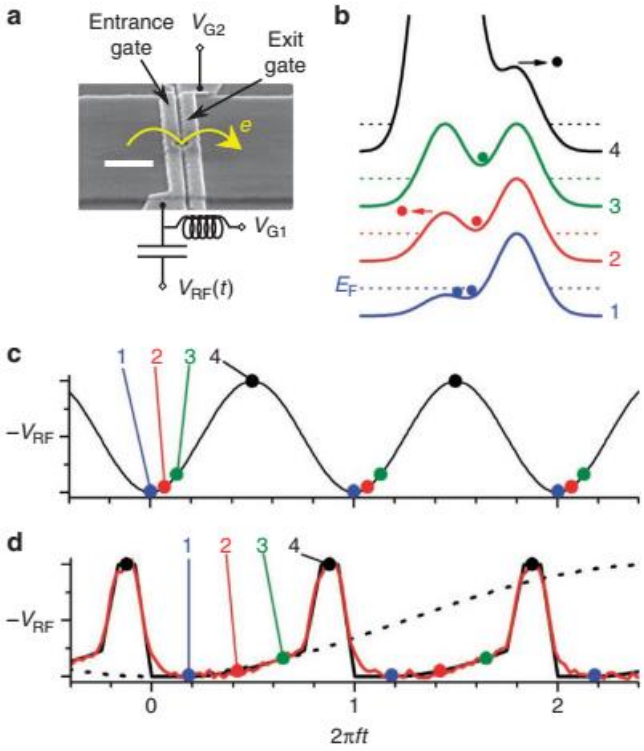

Figure 3.20: **Potential landscapes used to provide a visual aid in the design of the arbitrary waveform. (a) The SEM image of the sample, (b) the potential landscapes showing the operation of the single-gate modulated pump, the numbers represent the pump cycle phases: 1-loading, 2-back-tunnelling, 3-trapping and 4-ejection. The colours correspond to those in (c) which is the conventional sinusoid. (d) The trapezoidal waveform showing the slow sinusoidal segment and fast trapezoidal segment (adapted from [25])**

Figure (3.21iii) shows a schematic representation of the measurement setup. The pico-ammeter used in the experiment is limited to 100 ppm accuracy, even after calibration. This is due to drift in the gain of the pre-amp stage. So, to achieve the required ppm accuracy, Giblin [25] generated a reference current I_R opposite in polarity to I_P by applying a voltage Vc across a temperature-controlled 1 GOhm standard resistor. He measured the device at 300 mK and applied a magnetic field of 14 T. We can see the dramatic effects of the AWG pulse on the quantised current in Figure (3.21iia to 3.21iic). It shows the plot of the fractional deviation

($\Delta Ip = 10^6(Ip - ef)/ef$) of the pumped current in ppm for different frequencies. Initially, in Figure (3.21iia), a 400 MHz sinusoid stimulates the entrance gate, and we see a broad plateau with uncertainty of 3 ppm. Giblin [25] claims that random uncertainty U_R dominates the overall uncertainty. When he increased the frequency to 630 MHz, the plateau became narrow but remained quantised in exit voltage. A further increase in the frequency results in a loss of quantisation. Figure (3.21iib and 3.21iic) illustrate how we can recover the quantisation by stimulating the entrance gate with an AWG pulse instead of a sinusoid. At 630 MHz, the plateau doubles in exit voltage compared to Figure (3.21iia). At 945 MHz, where there was no plateau previously, a quantised current is now present after stimulating the entrance gate with the AWG pulsed wave. Giblin showed that the current generated by the AWG at 945 MHz was about 150 pA (see Figure 3.21i), with a total systematic uncertainty of 1.2 ppm, which is dominated by the 0.8 ppm systematic uncertainty in the calibration of the resistor. They claim an accuracy of one or two orders of magnitude better than the experimental uncertainty could be achieved according to the cascade decay model [25].

In 2019, Howe and Blumenthal et al. [1] conducted a study in which they discovered a 'new' single electron pumping mechanism that leads to the 'long pumping regime' (LPR). In this study, they pumped electrons over a one-dimensional split gate confinement potential rather than over the conventional finger-gate potential. In the LPR, the plateaus of the quantized current are over two orders of magnitude longer than those of the conventional pumps and turnstiles, which operate in the 'conventional pumping regime' (CPR). These extended plateaus are robust along the exit and entrance gate voltages of the pump with increasing RF power and increasing source-drain bias voltage. They conducted the experiments at a temperature of 6 K, with zero magnetic fields (B = 0 T) and a driving frequency of f = 180 MHz.

Figure (3.22a) shows the measurement setup of the sample. The actual sample is in Figure (4.30). Figure (3.22b) shows that the plateau width increases with an increasing RF power. That is, the plateaus are robust in entrance gate voltages. This result is consistent with the study conducted by Kaestner et al. [53]. The two experiments agree although different pump geometries are used. We also notice that the length of the plateaus becomes more robust with increasing RF power. That is, the plateaus elongate along the entire range of the exit voltages

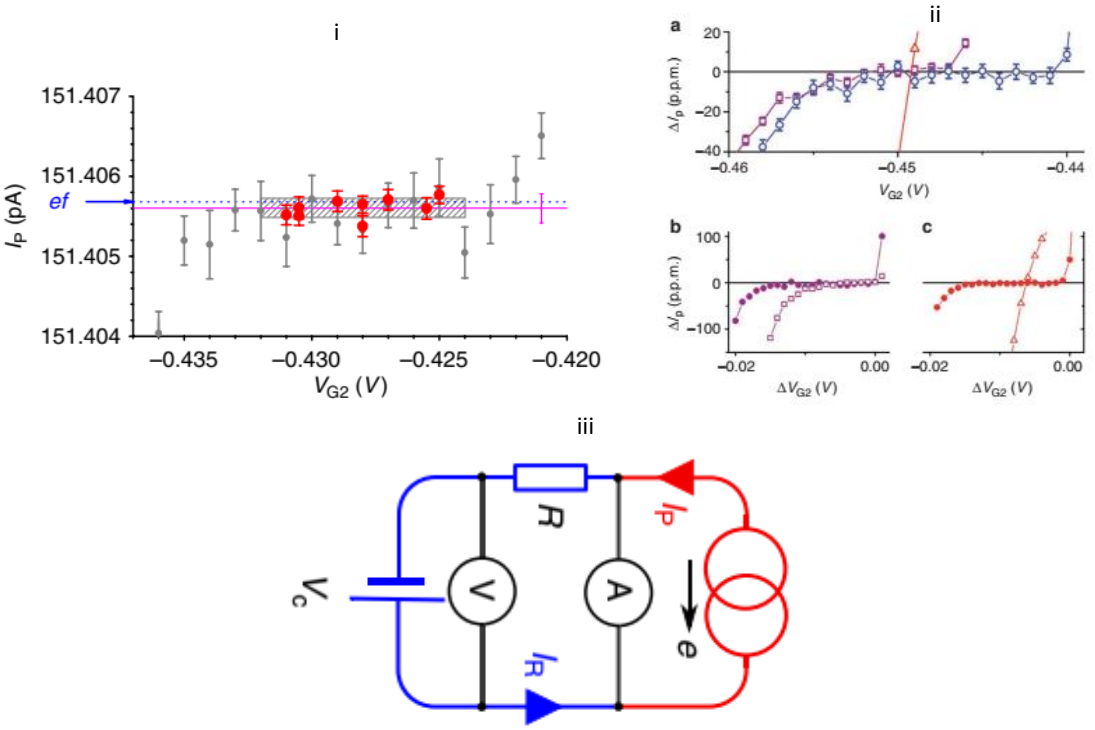

Figure 3.21: **(i) High-resolution measurement of the pump current as a function of exit gate voltage on the n = 1 plateau with f = 945 MHz and B = 14 T. (ii) Effect of AWG on pump performance for sample 1. (a) Fractional deviation of quantised current from ef in ppm, for a sinusoid driven at 400 MHz (circles), 630 MHz (squares) and 945 MHz (triangles) vs Vexit. (b,c) quantized current vs offset exit gate voltage VG2, at 630 MHz (panel b) and 945 MHz (panel c). open (solid) points indicate sine wave (AWG pulse) drive. (iii) Schematic circuit of the measurement setup. The pump is depicted as a current source (adapted from[25])**

with increasing RF power. Figure (3.22c) shows that an increasing source-drain bias elongates the plateaus along the exit gate voltage, making them robust in exit voltage.

The reason we enter into this long plateau regime is explained by the model provided for the finger-split gate configuration in [1]. The cross-section of the potential profile for the finger-finger gate versus the finger-split gate geometries with the energies along y = 0 is shown in Figure (3.23). The finger-split gate has its maximum potential energy at 5.076×10^{-7} m, within the region of the entrance

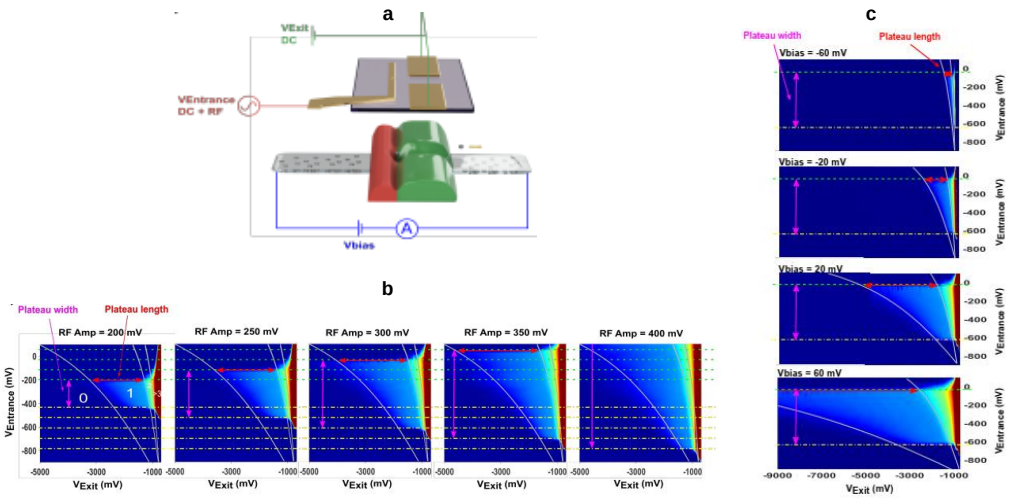

Figure 3.22: **Illustrates the long pumping regime with increasing RF power and source-drain bias voltage. (a) Schematic of gate profile and experimental setup, (b) Pumpmaps in the long plateau regime for different RF amplitudes and (c) Pumpmaps in the long plateau regime for different source-drain bias voltages (adapted from [1])**

finger gate. It is thus favorable for the electron to leave through the exit split gate centred at x = 0 m. In the case of the finger-finger gate geometry, the position of the maximum potential is at x = 2.820×10^{-9} m, within the physical boundary of the exit gate and therefore clearly blocking any path for the electron to exit, and thus pump [1]. This happens because the source-drain bias pulled the split-gate saddle point potential low, thus reducing the exit gate voltage required to form the quantum dot. Therefore, the pump could operate in the long plateau regime for some range of the entrance gate voltages.

3.3 Summary of the Properties of Single-Gate modulation pump

The single-gate modulated pump realised by Kaestner [21] has the following properties: It has a very simple geometric architecture, using only two gates, making it easy to fabricate. It has very good low-frequency stability, and the quantised current is only a function of the pump's driving frequency [52]. This pump is robust along the entrance gate. This is, the length of a plateau along the entrance

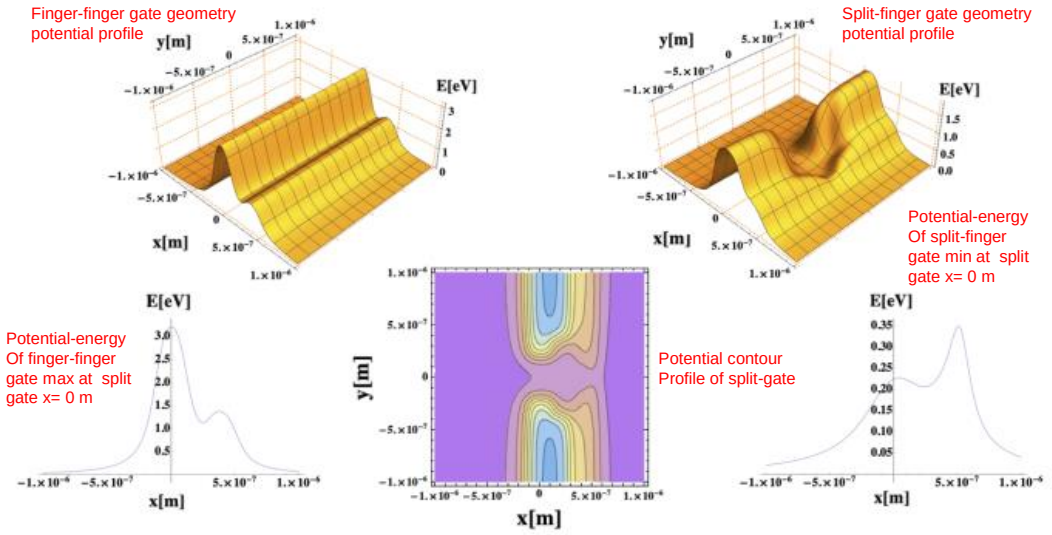

Figure 3.23: **Presents the potential profile model for the finger-finger gate (top left) and split-finger gate (top right). A potential energy cut along y = 0 m for the finger-finger gate is shown on the bottom left, it has a maximum at the finger gate at x =0 m. While that for the split-finger gate is shown on the bottom right, and it has a minimum on the split gate at x=0 m. A contour map of the split-gate potential is in the middle (adapted from [1])**

gate increase with an increase in the RF power [53]. This pump is also robust along the exit gate, meaning the length of the plateau increases with increasing magnetic field [54]. These facts makes the single-gate modulated pump a potential module for a scalable quantised current source [53]. The implication of this is that we can combine the single-gate modulation pump in various ways to implement the Ampere standard. Such an experiment was carried out by Wright [55], who showed that two single-gate pumps could be operated in parallel. Finally, Giblin et al. [25] showed that an arbitrary wave could increase the pumped current due to an increase in the driving frequency, without introducing error. These properties make the single-gate modulated pump a very good candidate in the realisation of the Ampere standard. We used these properties, and along with Giblin's scheme to study the effects of an arbitrary waveform on finger-split gate single-electron pump.

Chapter 4

Sample Fabrication And Instrumentation

4.1 The Growth and Patterning of Low Dimensional Semiconductor Nanostructure Devices

As the demand grew for faster and smaller technology during the past five decades, so did the challenge to create such miniature high performing devices. The ongoing miniaturization of solid-state devices has stimulated the studies of 'new' physical properties in low dimensional solids. In particular, those properties arising from charge quantization and quantum mechanics. In the angstrom scale, these devices are clustering of atoms whose properties can be regulated with external gate contacts. Examples of such devices are two-dimensional electron gas, nanowire, and quantum dots [27]. The studies of the properties of these devices have been possible during the past three decades owing to the huge breakthroughs in nanofabrication technology [43]. This section reviews the relevant technological advancement required to fabricate low dimensional solid-state devices and it is the first step to understanding how they operate. In particular, the section will focus on the growth and patterning of GaAs/AlGaAs low dimensional heterostructure system.

4.1.1 Cleanroom

Nanofabrication takes place in a special environment called a cleanroom, as illustrated in Figure (4.1). The cleanroom houses many high-tech systems, such as deposition systems, lithography systems, wire bonding systems, and many more.

The formal definition of a cleanroom is stipulated by the international organization for standardization (ISO) [57], but simply put, cleanrooms are facilities designed for manufacturing products or conducting research that requires an extremely clean environment [58]. To ensure the reproducibility and reliability of the fabricated devices, various cleanroom techniques are employed to control the number of airborne particles entering the room because these particles can contaminate the sample being fabricated [57][58].

Figure 4.1: **Illustrates a cleanroom environment (adapted from [59])**

Contaminates could arise from various sources: dust, grease, bacteria, light, and many others could be present in the room that could change the dimensions of the device part or dirty the surface of the device, thus reducing the device processing yield, performance, and reliability [57]. Therefore, the allowed contaminants in the cleanroom have to be controlled. The primary way to control these contaminants is to use airflow principles like laminar and turbulent flow. Various filter systems are utilized to filter the air entering and leaving the room. Additionally, strategies such as enforcing a special dress code and washing of hands, pass-thru lockers and chambers, and intensive detail to cleaning are exercised [58]. The quality of the cleanroom is measured by a standard based on the number of particles per cubic meter present in the room and the primary standard is stipulated by the ISO. The standards are called 'grade' or 'class'.

4.1.2 Deposition

Thin-film (coating) is a layer of a material placed on the surface of another material to modify and increase the physical, chemical, and morphological properties of the surface of the material. The material being coated is called a substrate, while the coating is the thin-film on the surface of the substrate. The thickness of the film ranges from several nanometers (monolayer) to several micrometers [60]. The deposition process controls the synthesis of materials as thin films, that is any technique used for depositing a thin layer of materials onto a substrate or surface [60]. In general, deposition processes are in principle divided into two types: first those involving an atom-by-atom transfer mode such as chemical vapor deposition (CVD) and physical vapor deposition (PVD) process of evaporation, etc, and second those involving droplet transfer such as plasma spraying and arc spraying, etc [60]. The difference between PVD and CVD is that the former uses mechanical, electrochemical, or thermodynamic means to produce thin-film on the substrate, while the latter uses a fluid precursor that undergoes a chemical change on the surface of the substrate [60]. Here we focus on the thermal evaporation process called molecular beam epitaxy (MBE) PVD technique. This technique is used to grow two-dimensional electron gas (2DEG) systems at the interface of gallium-arsenide and aluminum-gallium-arsenide heterostructure.

MBE is an atomic layer crystal growth technique based on the reaction of molecular or atomic beams with a heated crystalline substrate, performed in an ultra-high vacuum (UHV) environment [61]. It makes possible the growth of heterostructures with compositions varying on a spatial scale of one to one hundred crystalline-lattice constants [26][62]. With this technique, it is relatively easy to grow a good interface of AlGaAs on top of a GaAs substrate. Figure (4.2a and 4.2b) shows an actual and detailed schematic of the MBE system respectively. The system contains heated cells (known as Knudsen-cells) which houses the materials to be grown such as tin (Sn), aluminum (Al), gallium (Ga), arsenic (As), and manganese (Mn). A substrate to grow the material, heaters, and shutters. These components are all inside a vacuum chamber attached to a vacuum pump.

MBE is essentially a two-step process as illustrated in Figure (4.3). During the first step, atoms or molecules which are the constituents of the growing material (e.g. atomic Ga and As for GaAs) are evaporated from the solid sources in the heated cells, collimated into beams, and are directed towards a heated substrate

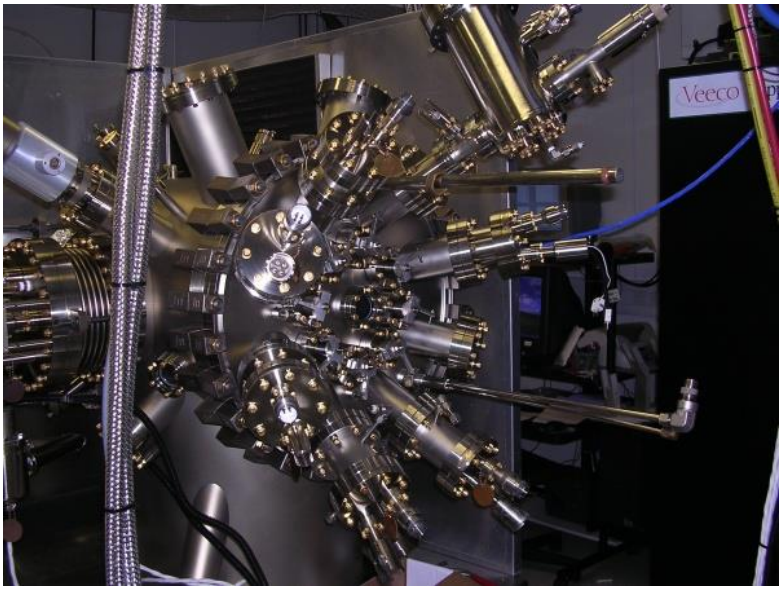

(a) The 3" Veeco Mod Gen II system at Cambridge University

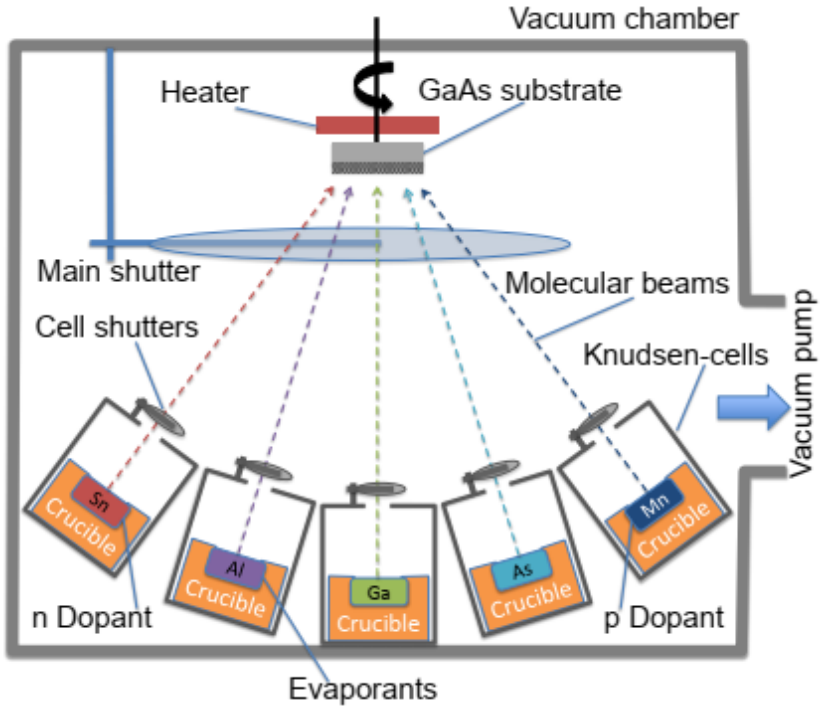

(b) A schematic of the inside of a MBE system

Figure 4.2: **(a) The 3" Veeco Mod Gen II system at Cambridge University. It is used to grow GaAs/AlGaAs high mobility structures on GaAs and InP substrates , and (b) shows that the system has Ga, Al, In, As, Si, Be, and Carbon sources (adapted from [63] [61])**

typically a few centimeters in size. The deposition onto the substrate is ballistic and the particles are said to undergo molecular flow. The substrate is often rotated for more uniform deposition rates across the substrate. The second step takes place on the surface of the substrate, where the deposited species are allowed to migrate on the surface of the substrate prior to their incorporation into the growing material substrate. This migration determines the profile or morphology of the film and its effectiveness depends on various factors such as the deposition rates of elements, surface temperature, and surface conditions to name a few [26][61].

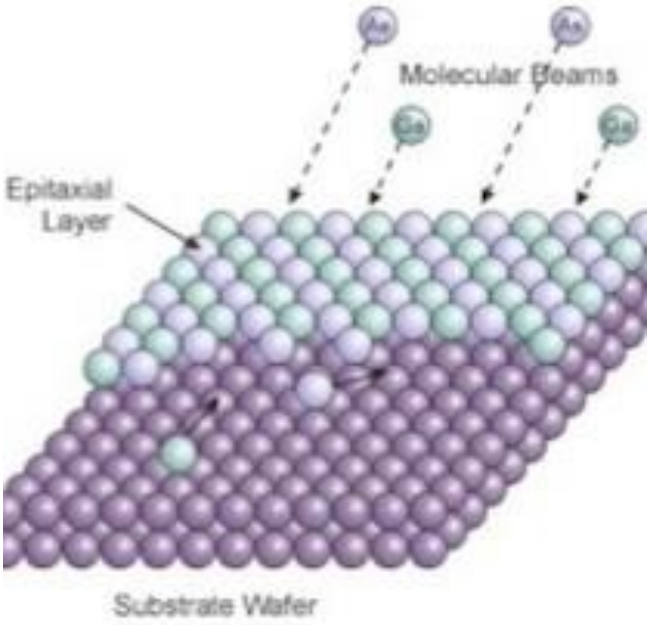

Figure 4.3: **Illustrates the epitaxial growth technique, where materials in the cells are layered one on top of the other to grow semiconductor wafers, and novel material for research development (adapted from [64])**

4.1.3 Lithography and etching

Device growth is the initial step in the nano-device fabrication process. After this initial step, the device is not yet ready for practical use. Further processing is required to make the device practical, such as patterning various geometric shapes, adding contacts and gates on the otherwise smooth cross-section of the grown heterostructure to allow the device to interact with its environment. This patterning

process is called lithography. Lithography is a technique used to transfer a geometric pattern onto a resist such as polymethyl methacrylate (PMMA). Many lithographic methods exist, for example, electron beam lithography (EBL), photolithography, and X-ray lithography to mention a few. Photolithography finds its application mainly in the semiconductor industry to fabricate devices such as microchips. X-ray lithography is utilized in the electronics industry for selective removal of parts of a thin-film. Ion lithography is used to create very small structures such as integrated circuits or other nanostructures [65]. On the other hand, electron beam lithography as shown in Figure (4.4) has long been established as a very flexible and reliable technique for nanotechnology applications. It offers the best resolution compared to other lithography techniques. The current EBL machines allow access to features sizes as small as few nanometers. However, such an ultimate resolution is not easily attained. The process requires a systematic methodology of the sample preparation and optimal system adjustment [65].

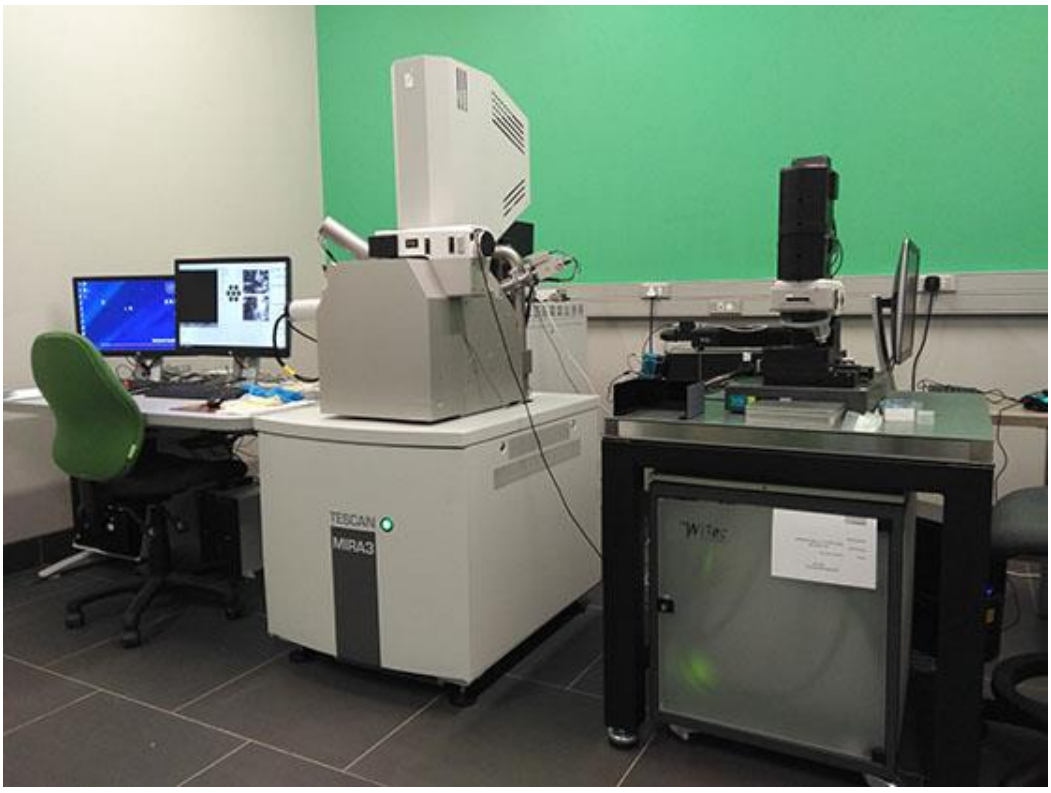

Figure 4.4: **The Tescan MIRA3 Advanced SEM with RISE Microscopy located in the Aaron Klug Centre for Imaging and Analysis at the University of Cape Town (UCT)**

Here we highlight only the general concepts of lithography, that is, the lithography process flow, exposure methods, photo-resist, and pattern transfer. A typical lithography process sequence is shown in Figure (4.5a), where the substrate is spin-coated with PMMA, followed by exposure of the resist with electron-beam, thereafter, the sample is developed, from there Ti and Au are deposited on the sample and finally, the lift-off process takes place. Examples of finished nano-devices are shown at the bottom of Figure (4.5b).

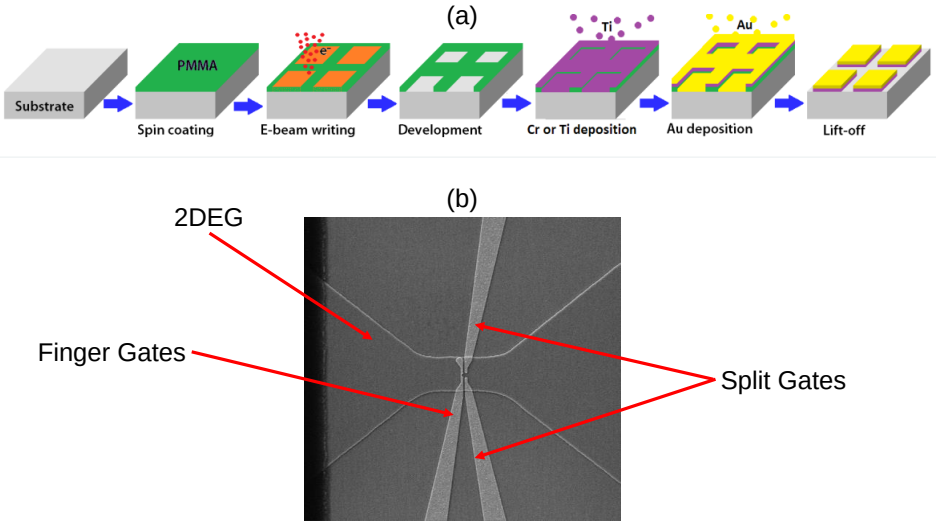

Figure 4.5: **(a) Typical lithographic process sequence (adapted from [66]), and (b) Single electron pump sample**

4.1.4 Inspection

The basics of nano-device growth and fabrication were presented in the previous sections. The follow-up step is to inspect and measure the fabricated structures. The inspection can be done using various methods: The optical microscope method can be used for surface profile, to measure the 'x,y' lateral dimensions of the device. Mechanical probing can be done to the device to measure its thickness. By scanning a probe in contact with the surface of the device one can get information such as the thickness or depth of the device's cross-sectional area. The scanning electron microscope (SEM) results in a higher resolution than visible light and can be used to inspect the surface of the device equally. Finally, the resistance of the sample can be determined by using probes to measure electrical resistance.

4.2 Sample Fabrication and Site

The ideas in Section (4.1) are now used in the fabrication process of the GaAs/AlGaAs single-electron pump samples to be experimentally studied in this report. The fabrication process included the use of a cleanroom, molecular beam epitaxy, optical and electron lithography, etching, and other steps necessary to have a device with the required performance that allows the study of quantisation effects such as charge quantisation. The device is composed of a GaAs/AlGaAs two dimensional electron gas heterostructure, Ohmic contacts, finger gates, and split gates. The devices were fabricated in the cleanroom at the Cavendish Laboratory at Cambridge University by Dr. Hume Howe .

4.2.1 Wafers

The standard GaAs/AlGaAs high electron mobility transistor (HEMT) wafers were used to fabricate the devices. The wafers were grown in the Cavendish by Dr. Harvey Beere and Dr. Ian Farrer using the molecular beam epitaxy process, discussed in Section (4.1.2). The layered structure of the standard HEMT wafer is shown in Figure (4.6). Different layers of GaAs and AlGaAs were grown on top of the un-doped GaAs substrate. The growth sequence began with the growth of the GaAs substrate, which formed the bottom layer. Then a 40 nm layer of undoped AlGaAs was grown on top of the GaAs substrate. This layer called the 'spacer layer' in literature separates the impurities of the doped AlGaAs layer from the GaAs layer, and so it increases the carrier mobility in the 2DEG. Following that, a 40 nm layer of Si-doped AlGaAs was grown on top of the undoped AlGaAs spacer layer. The Silicon-doped (Si-doped) layer has a high carrier density, and at low enough temperature, enough of these carriers will migrate to the interface of the undoped AlGaAs/GaAs to form the 2DEG. Finally, a 10 nm layer of undoped GaAs functioning as a protective layer was grown on top of the Si-doped AlGaAs layer. The wafer used in this report has a carrier density of 1.87×10^{15} m^{-2} and mobility of 101 m^2/Vs in the dark at 1.5 K [47].

4.2.2 Masks

The fabrication process requires 3 to 6 layers to be patterned, depending on whether oxides or top gates are added. Electron beam and optical lithography

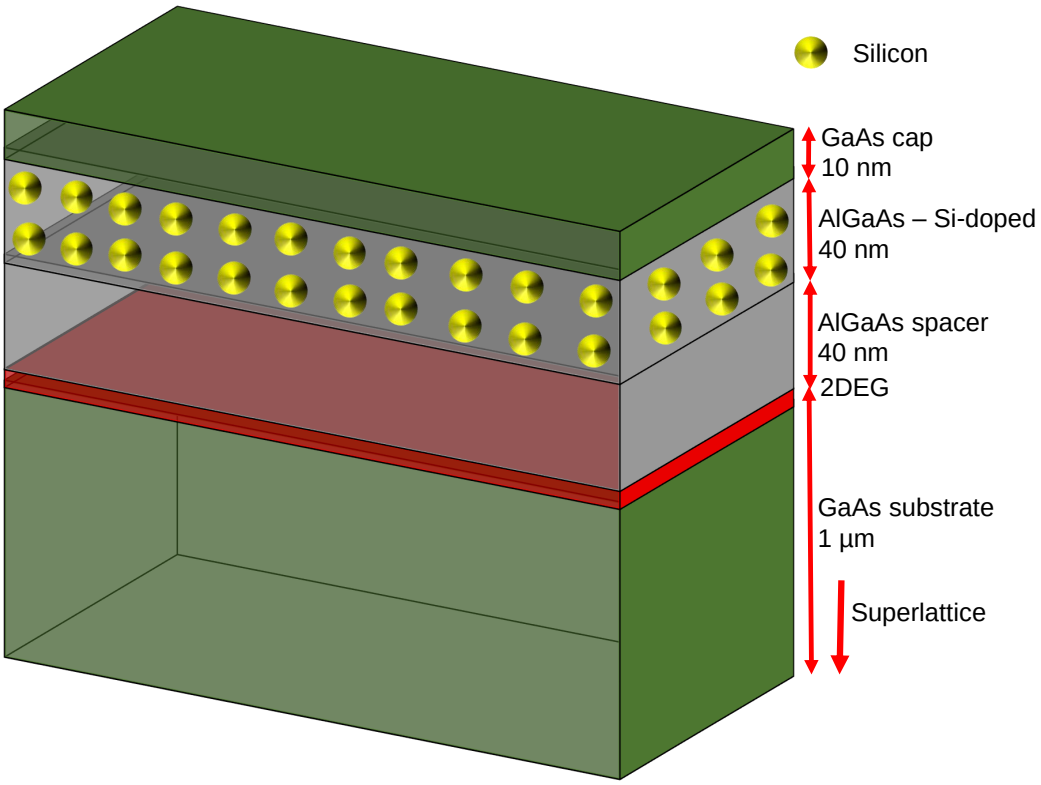

Figure 4.6: **A diagram of the layer structure of the wafers used (adapted from [47])**

were both used to make the patterns. Optical lithography was used whenever possible because it allowed for the patterning of thicker gates, quicker and cheaper processing. The optical lithography process utilizes a mask to pattern the relevant layers. Here masks were used in 3 main optical processing steps: mesa, Ohmic, and gates [47].

The mask used to pattern our devices were adapted from Dr. Masaya Kataoka's NPL mask. It is called the HHH mask, and some of the patterns of the adapted masks are illustrated in Figure (4.7). The mesa is shown in Figure (4.7a), where the large central region has 14 arms to which Ohmic contacts are made. The asymmetry of the mesa makes it easy to align and the spaces on either side of the central region are available to address the chip with an ID. The Ohmic contacts are shown in Figure (4.7b). When the Ohmic contact is combined with the mesa, it gives multiple combinations for 2 terminal and 4 terminal measurements. The Ohmic pads cover both the Ohmics and gates; this design offers more flexibility in terms of which the combination of Ohmics and gates to be utilized in an exper-

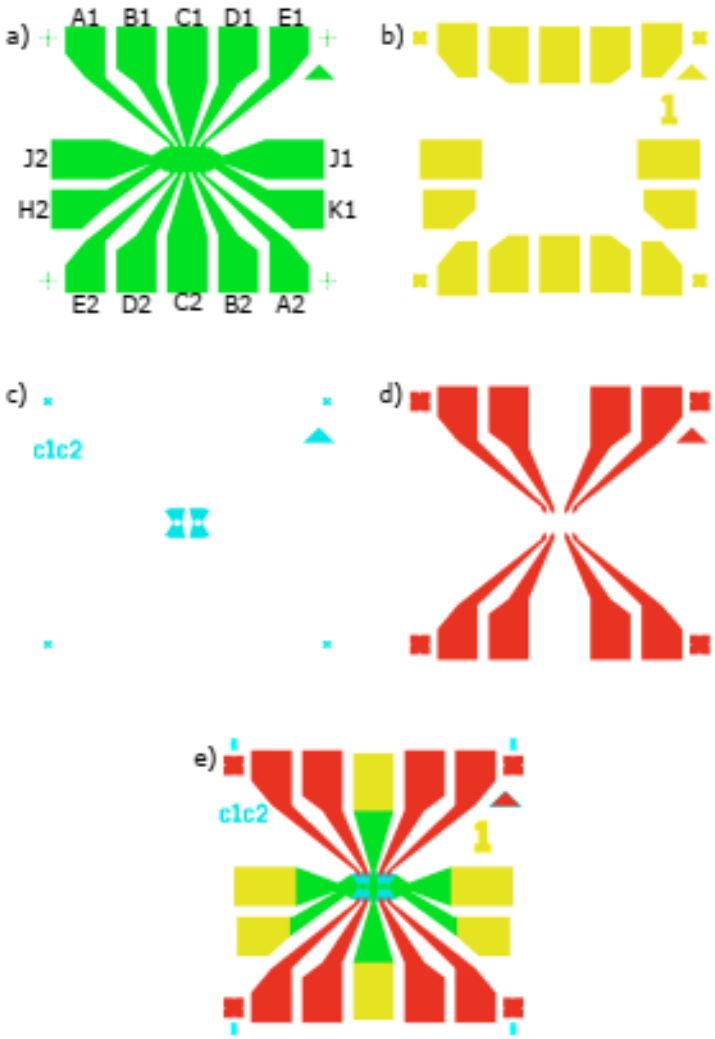

Figure 4.7: **A schematic of the HHH mask, described below, showing the (a) mesa, (b) Ohmics, (c) narrow etch, (d) gates, and (e) the patterns overlaid (adapted from** [47])

iment. Additionally, annealed Ohmics improves the adhesion of the gates. The pads are denoted A1 → J2; conventionally, the combination C1, C2, J1, J2, K1, H2 are used as Ohmics and the rest as gates in a measurement. A secondary etch was done to isolate the gate arms from the Ohmic arms and to create a narrow channel for the pump. Figure (4.7c) shows the secondary etch channel. Electron beam lithography was used for the small region of gates. It is more difficult to bond to EBL gates than optical gates because they are thinner. The optical gates overlap the EBL gates to create one set of electrically continuous gates as shown in

Figure (4.7d). Figure (4.7e) shows the patterns overlaid for this mesa, secondary etch and gate combination. There are additional combinations for different experimental designs [47].

4.2.3 Scribing, cleaving and cleaning

Before the patterning process began, the wafer was scribed into the desired size of the chip. The chip size depends on the design of the optical mask and the number of devices required. A scriber is a machine with a diamond-tipped stylus, used to score the wafer. The wafers were typically scribed into 8 mm by 10.5 mm chips, with a margin for edge-bead removal. The chips were scribed with one edge parallel to the major flat, which was used to align the mesa. Edges (roughly 1-4 mm) were scribed along the major or minor flat. Once the wafer was scribed into chips, it was transferred to a cleaving block, containing a step separating two planes. The wafer was positioned such that the score is parallel to the step. Glass was used to secure the edge not hanging, while the hanging edge was gently pushed down with tweezers on the side with the score. The chip should break off cleanly, with the edges following one plane of the crystal lattice. Finally, the chips were cleaned by placing them in acetone in an ultrasonic bath for about 5 min, rinsed in isopropanol (IPA), and dried with nitrogen (N2) [47].

4.2.4 Optical mesa

The mesa was initially defined optically, then wet etched, leaving only the region of the 2DEG that defines the channel. A yellow room, see Figure (4.1), was used to expose the resist and develop the mesa when exposed to ultraviolet (UV) light. The procedure for creating the optically defined mesa is illustrated in Figure (4.8). The cleaned chip is shown in Figure (4.8a). The chip was first pre-baked on a hotplate at 125°C for 5 min to ensure that it was solvent-free. Next, Shipley Microposit 1805 photoresist (PR) was spun onto the chip, see Figure (4.8b). The resist was hardened by baking the chip at 90°C for 2 min. Then the devices were positioned under a mask in an aligner, and the mesa pattern was aligned such that the mesa channel was parallel to the major flat as shown in Figure (4.8c). The devices were then exposed to UV for 3.5 sec. The exposed resist was then dissolved in MF-319 developer for 35 sec, rinsed in demineralization (DI) water,

and dried with N2 see Figure (4.8d). After that, the etching process takes place. A hydrochloric acid (HCL) oxide removal stage is done before the etching step to ensure that the etching is consistent among the devices. This was done by dipping the devices in a dilute HCL:H_2O (1:5) mixture for 15 sec and then rinsing it in DI water. To etch the devices without etching into the photoresist a mixture of sulphuric acid (H2SO4) and hydrogen peroxide (H2O2) was utilized. The H2O2 oxidizes the surface of the device, while the H2SO4 removes the oxide. The most frequently used etchant was H2SO4:H2O2:H2O (1:8:120), which etches at a rate of about 2 nm/s. The device was etched past the 2DEG, see Figure (4.8e), then it was rinsed in DI water and dried with N2, see Figure (4.8f) [47].

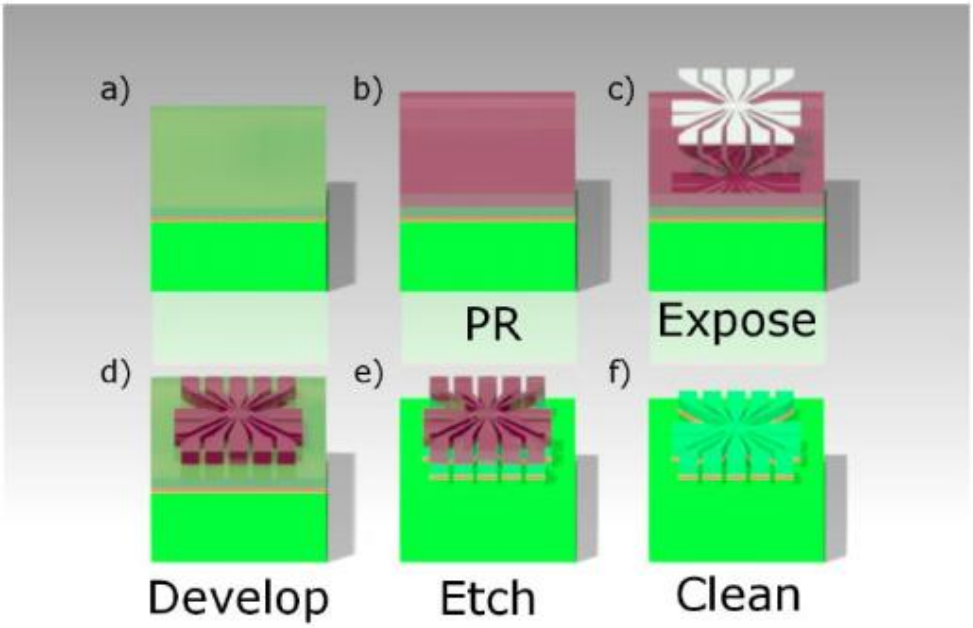

Figure 4.8: **A diagram showing the steps to produce an etched optical mesa (adapted from [47])**

4.2.5 Ohmics

An electrical connection to the 2DEG is made via the Ohmic contacts. The Ohmic contacts were patterned and developed, and then evaporated and annealed from the HHH mask in Figure (4.7b). The steps used to create the Ohmic contacts are illustrated in Figure (4.9). The mesa etched device from Figure (4.8f) is again

presented in Figure (4.9a) as the starting point for the creation of the Ohmic contacts. The device was first pre-baked at 125°C for 5 min, then Shipley Microposit 1813 was spun on it at 5500 rpm for 45 sec. It was then baked at 90°C for 2 min as shown in Figure (4.9b). After that, the device was positioned into an aligner, and the mesa was aligned to the Ohmic pattern using the alignment marks etched into the mesa and exposed to UV light for 6.5 seconds, see Figure (4.9c). Before developing, the top of the photoresist was hardened so that an undercut profile would be created when the photoresist was developed, Figure (4.9d). The hardening was done by putting the device inside chlorobenzene for 1 min then dried using N2. The device was then placed in the MF-319 developer for 55 sec, see Figure (4.9e). The developer takes longer to dissolve the hardened resist than the normal resist does, which creates the undercut profile needed to ensure a good lift-of. It was then rinsed in DI water and dried with N2. An HCL oxide removal was done after inspecting the device under a microscope to ensure the PR was fully developed. This is to ensure that the evaporated metal made good contact and stuck. The oxide removal step was done as close as possible to the time the device was loaded into the evaporator [47].

The type of metal that was used was a gold germanium nickel (AuGeNi) alloy. The gold makes the electrical contact, the germanium helps the gold diffuse, and the nickel smooths the gold diffusion and makes it stick. Figure (4.10) shows the evaporator: it consists of a tungsten boat holding alloy slugs and a metal plate that holds the device above the boat and facing the boat. All of which are housed in a vacuum Bell jar. The alloy heats up and melts when a large current is passed through the boat. The boat itself does not melt because it is made of tungsten. Its melting temperature is twice that of AuGeNi. The thermally evaporated AuGeNi does not scatter in a high vacuum (lower than 10^{-6} mbar for AuGeNi), and so it gets deposited ballistically onto the device. A crystal monitor is used to measure the amount of deposited metal. The quartz crystal is resonated at a known frequency, and the change in the resonant frequency is measured as metal is deposited onto it. The thickness of the metal evaporated should be sufficient for it to diffuse well into the 2DEG and to be easy to bond to, usually this would be around 140 nm, see Figure (4.9f and 4.9i). However, the evaporated metal thickness should be less than the undercut height. Once the required AuGeNi thickness was reached, a shutter that blocks the line-of-sight path from the boat to the device was closed [47].

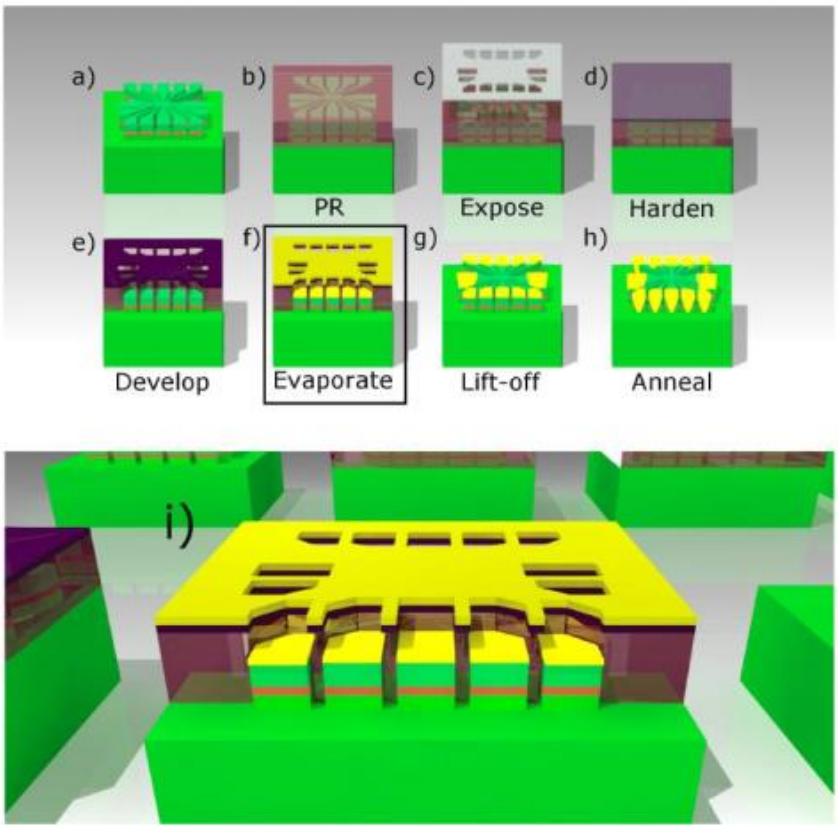

Figure 4.9: **Illustrates the steps required to produce Ohmic contacts. Details of (a) through (h) are provided in the text. (i) is a zoomed in diagram of (f) showing the undercut profile of the photoresist (adapted from [47])**

After the evaporation process, the device was placed inside a sealed jar containing acetone for about an hour. The jar was sealed to prevent leaving the device with incomplete lift-off because acetone evaporates quickly Figure (4.9g). To ensure that the metal Ohmics were in electrical contact with the 2DEG, the AuGeNi pads were annealed using a rapid thermal annealer (RTA), which melts the AuGeNi at a high temperature, allowing it to diffuse into the device, Figure (4.9f). A typical annealing process is KEN01, which heats the device to 430°C for 80 sec. The contacts were tested with a probe station, which is a simple device consisting of two probes that can be controlled with micro-manipulators, attached to a digital multimeter. For the classical 40 nm HEMT with $a > 1800$ μm long and > 80 μm wide channel, the resistance across a 2DEG at 300 K should be $R < 30\,\Omega$ in the light, $R < 50\,\Omega$ in the dark, and $R < 5\,\Omega$ in the dark at 77 K [47].

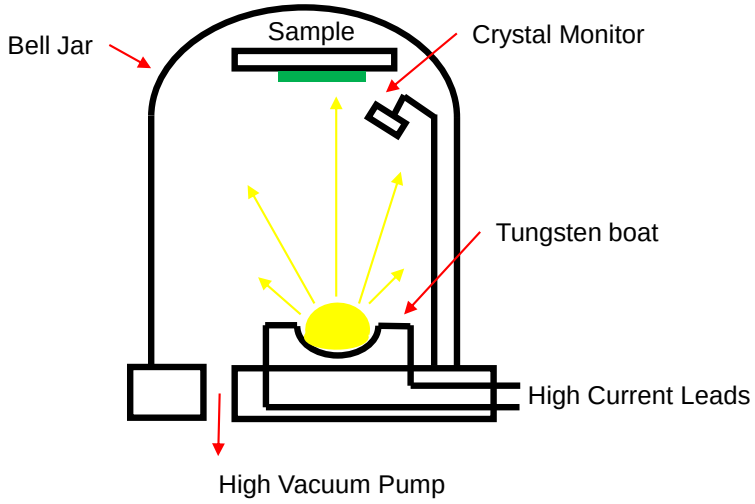

Figure 4.10: **The evaporator (adapted from [47])**

4.2.6 EBL mesa

The mesa was initially optically defined in Section (4.2.4). It was etched to 170 μm wide in the central region and 50 μm wide at the narrowest regions. In this section, the EBL patterning process was used to further etch the fine features on the mesa. Quantum pump devices typically require the conduction channels to be patterned with a width ranging from 700 nm to greater than 2 μm. However, the effective width of the channel is smaller than its actual width because of the sidewall depletion. The free electrons are trapped on the sidewalls due to dangling bonds and DX scattering centers. The depth and roughness of the mesa etch determine the amount of depletion. Such features sizes are too small for optical lithography methods; therefore, they are done with the EBL technique [47].

The device was RF-ashed for 40 sec, and HCL dipped to de-scum and remove any oxide in preparation for EBL. It was then put in the oven for 20 min at 150°C to evaporate any solvents. (PMMA) 950 K A4 Neat was spun on top at 5500 rpm for 1 min, and it was baked for a further 10 min at 150°C to harden before it was submitted for EBL. Once the mesa patterning was done, the device was developed in MIBK:IPA: MEK (5:15:1) fast-feature EBL developer for 8 sec, rinsed in IPA, and dried with N2 [47].

The most challenging stage of processing is perhaps the mesa etch. The problems presented at this processing stage seems to be the major reason for low device yield. Issues such as electrons which are trapped by DX scattering centers and dangling bonds around the edge of the 2DEG are the primary cause. This does not pose a problem for wide channels, but it does for narrowly defined channels. This issue was addressed by etching only partially into the dopant layer as depicted in Figure (4.11). By shallow etching, one could ensure that some dopants are left to fulfill the surface states, and more electrons remain in the channel, which helps the device to conduct [47].

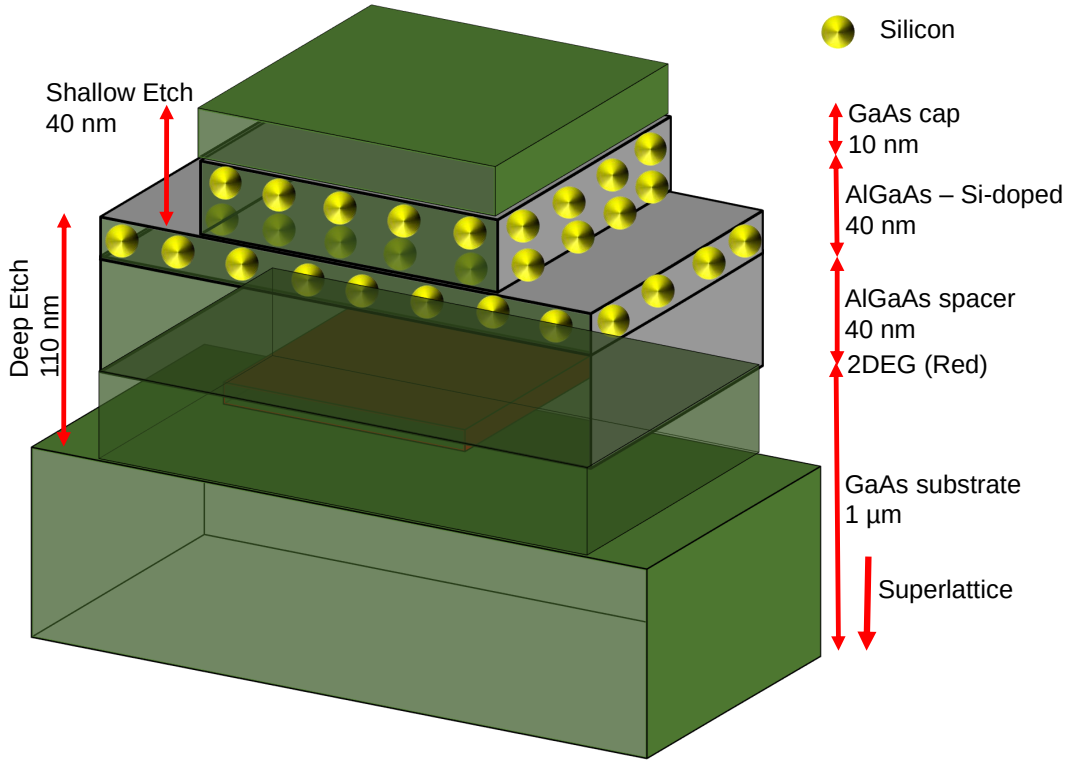

Figure 4.11: **Illustrates the relative depths of an optically patterned deep etch and an EBL patterned shallow etch (adapted from [47])**

The devices were etched 40 nm from the GaAs cap into the doped AlGaAs layer see Figure (4.12c). To accurately etch the correct depth, a row of devices was scribed for calibration. These calibrated chips were HCL-dipped to remove any oxide before etching. A slow etch solution H_3PO_4:H_2O_2:H_2O (1:1:38) with an etch rate of about 1 nm per second was used to better calibrate the etch depth and to minimize the effect that the etch speed can have on the surface roughness.

Heat and light can affect the etch rate, although the rate depends predominately on the percentage of H_2O_2 present and its distribution. Therefore, the solution was left to stabilize for at least an hour before use and the device was etched in the shade. The etching procedure is the same for both optical and EBL etching as described above in Section (4.2.4), only in the case of the EBL, the etching solution was slower. The device was placed in acetone for 2 min after etching to remove the remaining PMMA, rinsed in IPA for 1 min and dried with N2. An Atomic Force Microscope (AFM) was used to check the depth of the etch. Based on the measurements for the calibration devices, the etching time was adjusted accordingly [47].

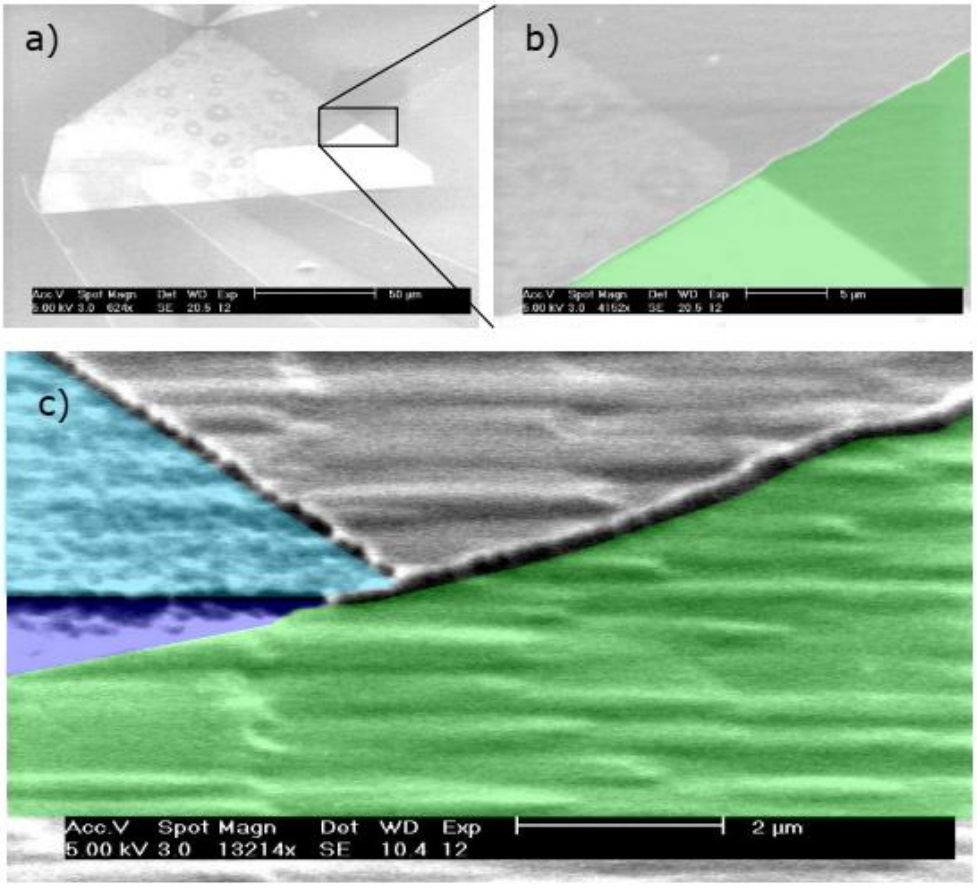

Figure 4.12: **(a) An SEM image illustrating the deep and shallow using surfactant, (b) a zoomed-in false-colour image with the deep etch (green), and (c) A shallow etch with no surfactant added (blue) (adapted from [47])**

After the shallow etch, the devices were inspected on the probe station to see if the shallow etch worked. The etch profile, wafer characteristics such as light and dark conduction, and the level of parallel conduction determines the resistance of the narrow channel. However, it was found that invariably a working channel has a resistance of about 1.5 times that of the wide channel. It is crucial that there must be no conduction between the gates and the Ohmics to prevent gate leakage [47].

4.2.7 EBL gates

The gates, like the mesa, were formed using a two-step process. An optical patterning process was used for the grosser features of the gates, and the EBL patterning process was used for the finer features of the gates. The method to prepare the device for EBL gates was similar to that for EBL etch, except a bilayer PMMA was used to create an undercut profile, which assists in lift-off. The device was first RF-ashed for 40 sec, then it was HCL-dipped to de-scum and remove any oxide. It was then pre-baked in the oven for 20 min at 150°C to evaporate any solvents. PMMA 100 K A6 Neat was spun on at 8000 rpm for 1 min, and the device was baked on a 180°C hot plate for 3 min. The second layer of PMMA 950 K A11:MIBK (1:5) was less viscous than the 100 K A6 Neat, so it spun thinner, but required a higher e-beam dosage to pattern, thus creating the undercut profile [47].

The solvent in the second layer PMMA will dissolve the PMMA on the first layer. Hence, the device must be spun within a couple of seconds of pipetting the second layer PMMA. The device was finally oven-baked for a further 10 min at 150°C to harden the PMMA and then submitted to EBL. After patterning the gates, the device was developed in MIBK:IPA: MEK (5:15:1) fast-feature EBL developer for 8 sec, rinsed in IPA, and dried with N2. After the EBL gates were developed, there were very small delicate regions of PMMA that may be traded-off if left exposed. So, the devices were developed as close as possible to the time they were loaded into the evaporator. The gates evaporation is similar to the Ohmics evaporation, but it is a two-layer Ti/Au evaporation. To form a sticking layer between the gold and the GaAs, a thin layer of Ti (5-15 nm) was first evaporated since the adhesion of Ti is much better than that of Au. Evaporating gold requires a much lower vacuum (10^{-5}mbar) than titanium (10^{-7}mbar). Consequently, a thin layer of gold (20-40 nm) was evaporated, determined by the etch depth. Devices

were left overnight in a sealed bottle of acetone. This is required for small feature sizes because the acetone takes more time to dissolve the PMMA in the areas between the pump gates. Figures (4.13a and 4.13b) illustrate the SEM images of the gates with a correct amount of Ti/Au deposited, enough to climb the shallow etch but not too much that they short. After evaporating EBL gates, the device is very sensitive to static; therefore, great care was taken in handling the device [47].

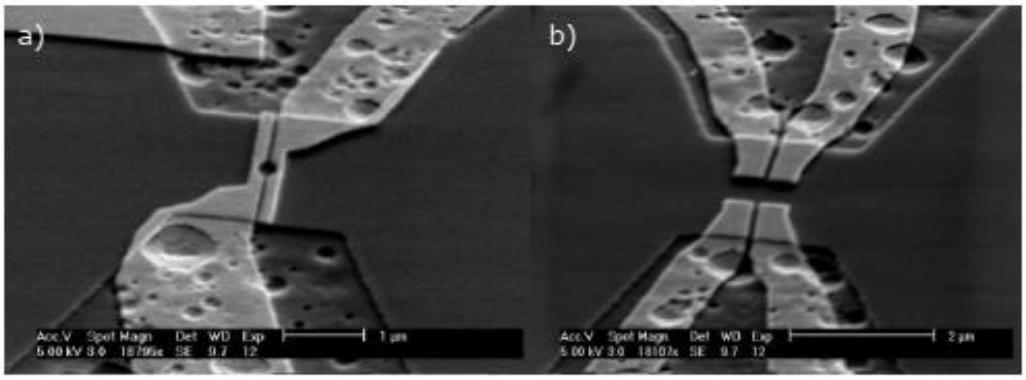

Figure 4.13: **SEM image of a device with desire EBL-gates (adapted from [47])**

4.2.8 Optical gates

The optical gates are an extension of the EBL gates to the bonding pads. The processing of the optical gates are similar to that of the Ohmics described in Section (4.2.5), except the gate pattern of the mask was exposed instead of the Ohmic pattern. Ti/Au (20 nm/100 nm) was then evaporated onto the device using the evaporation process described in Section (4.2.7). Figure (4.14) shows the optical gate Lilly padding (red oval), caused by the undercut profile of the photoresist. This can be avoided by taking alternative steps such as lift-of resist (LOR). However, layering the optical gates after the EBL gates work too. Furthermore, even without Lilly padding, the gold deposited for the EBL gates is about a third of the thickness of the gold deposited for the optical gates. This makes the layering easier to ensure electrical contact [47].

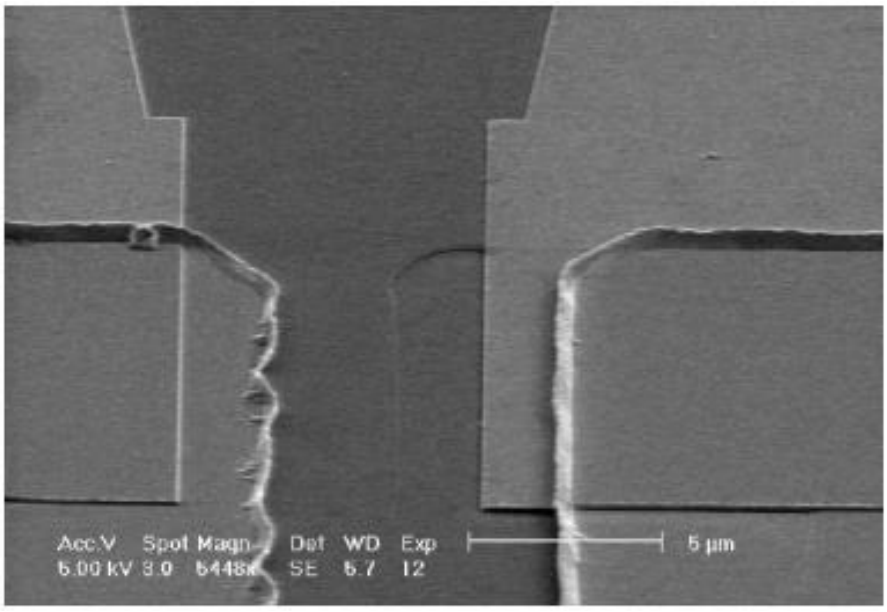

Figure 4.14: **SEM image illustrating lillypadding of the optical gates (adapted from [47])**

4.3 Instruments: their Reliability and Validity

4.3.1 The dilution refrigerator

To observe the quantum properties of a miniature device, not only is it necessary for one to be concerned with the size and dimensions of the devices, but also the environment in which the devices will be measured. Good electron transport measurements at a nanoscale necessitate a low-temperature environment for several reasons: quantum effects do not persist at high temperatures; the Fermi-Dirac distribution is sharp at low temperatures; other forms of energy become dominant, leading to phenomena such as Coulomb blockade; lattice vibrations (phonons) are much weaker at lower temperatures, resulting in low electron-phonon interactions. The environment of interest here is a refrigerator at less than 10 K. The development in low-temperature technology has led to three refrigeration techniques that dominate low-temperature physics today. Temperatures in the Kelvin range down to about 1 K are reached by the evaporation of liquid ^{4}He. The millikelvin range is entirely dominated by the ^{3}He -^{4}He dilution refrigeration technique, which typically reaches a minimum value of 10 mK; the present record is about 2 mK. Finally, in the microkelvin temperature range, the nuclear adiabatic demagnetization method is used; this technique can reach temperatures below 1.5 μK [67] [68].

Phase diagram of liquid ^{3}He -^{4}He mixture:

The ^{3}He -^{4}He dilution refrigeration method will be the focus of this report. It is the only continuous refrigeration technique for temperatures below 300 mK. Furthermore, magnetic fields, which are often needed in low-temperature experiments have negligible effects on its performance. Today this method is the most important refrigeration technology for the temperature range between about 5 mK and 1 K, and it is the base from which lower temperatures can be reached [67] [68].

The cooling of a dilution fridge can be understood by studying the phase diagram of the mixed Isotope of liquid ^{3}He and ^{4}He. The ^{3}He concentration x vs the temperature T phase diagram of liquid ^{3}He -^{4}He mixtures at saturated vapour pressure is illustrated in Figure (4.15). It reveals several remarkable features of the mixed isotopes. Let us consider the pure liquids; one can see that ^{4}He becomes a superfluid at 2.177 K. By contrast, the Fermi liquid ^{3}He does not show any phase transition in the temperature range of interest. We see that eventually, the ^{4}He superfluidity terminates for ^{3}He concentrations higher than 67.5 per cent. At this concentration and temperature of 867 mK, the Lambda-line meets the phase separation line. This implies that below this temperature, the two isotopes only form a homogeneous mixture for certain limiting concentrations, which is temperature-dependent [67].

This forbidden region is the region where there is no combination of temperatures and concentrations allowed for the helium mixtures. Therefore, if one cools a helium mixture (with $x > 6.6$ %) to temperatures below 870 mK, then the liquid will eventually separate into two phases, one rich in ^{4}He and the other rich in ^{3}He. The ^{3}He rich liquid floats on top of the ^{4}He-rich liquid because it is less dense. If the temperature is decreased close to absolute zero, then we notice that the ^{3}He-rich liquid becomes pure ^{3}He. What occurs on the ^{4}He-rich side is astonishing. Here the concentration of the dilute isotope ^{3}He does not approach zero even though the temperature is approaching zero. It reaches a constant concentration of 6.6 per cent ^{3}He in ^{4}He at saturated vapour pressure even for T = 0 K. This finite solubility is of the utmost importance for ^{3}He -^{4}He dilution refrigeration technology, without which, it would not work [67].

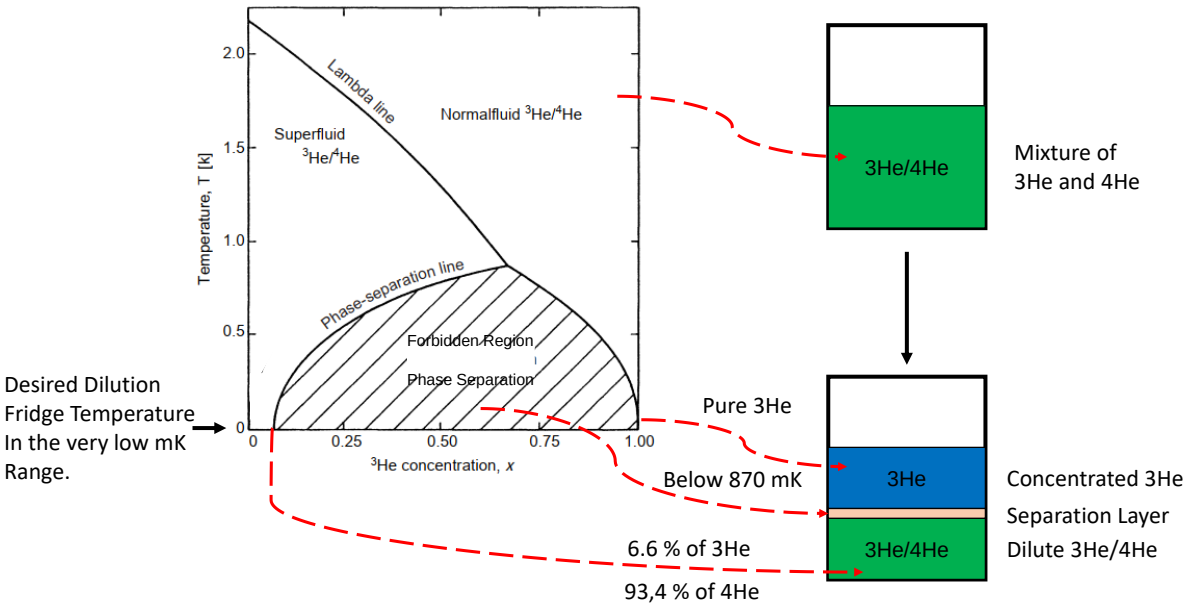

Figure 4.15: **Phase diagram of liquid ^{3}He -^{4}He mixtures at saturated vapour pressure. The diagram shows the lambda line for the superfluid transition of ^{4}He, the phase separation line of the mixtures below which they separate into a ^{4}He-rich and a ^{3}He-rich phase (adapted from [67])**

4.3.2 Dilution refrigerator at the University of Cape Town

System description:

The nanoelectronics research laboratory at the University of Cape Town houses a Leiden Cryogenics CF-CS81-1600 cryogen-free dilution refrigerator as depicted in Figure (4.16). It consists of a dilution cryostat unit, a gas handling system (GHS), and a compressor for the pulse tube (PT). Consider the dilution cryostat unit, when it is assembled, externally it has a large Dewer called the outer vacuum can (OVC), see Figure (4.17), which contains the evacuated cold regions of the fridge. The OVC is bolted onto the top flange via an O-ring. The flange hosts many components such as a manifold of interconnected lines, valves and gauges, the pulse tube insert, several clear-shorts for insertable probes, leads to the magnet below, leads to the high-power heaters and pumping outlet to the OVC. This flange rests on top of two wooden planks which in turn sits on the platform of a lifting table operated by a motor shown in Figure (4.18). The manifold couples the lines coming from the GHS to the cold part of the dilution refrigerator via the

appropriate standard valves. The valves are electric, mechanic, and pneumatic. The manifold also contains connector heads for electrical wiring coming from the cold region below. The PT insert has a cold head that sits on the top flange. The Helium gas inlet and outlet enter this cold head via a motor that operates a valve that controls the motion of the Helium gas between the compressor and the cold head. A cold-insertable probe can also be bolted on the top flange and it offers the advantage to change the sample quickly during operation [69].

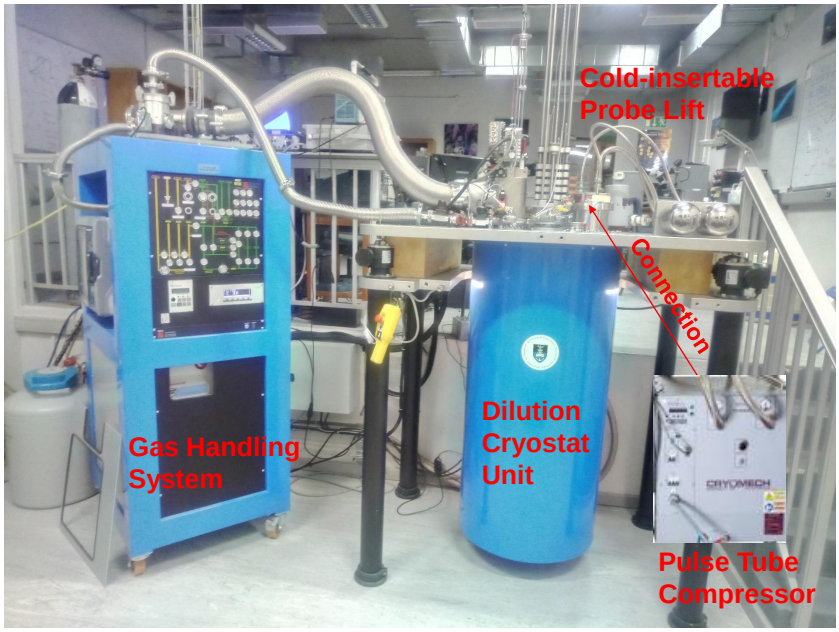

Figure 4.16: **UCT's Leiden Cryogenics Cryogen-free CF-CS81-1600 Models dilution refrigerator. The typical components are: The gas handling system, the dilution cryostat unit, and the pulse tube compressor**

Internally the cold regions of the fridge are defined by several cylindrical flanges, see Figure (4.19). These flanges get colder the further they are from the top flange. A cylindrical can is bolted onto the 50 K flange and acts as a radiation shield. The inner vacuum can (IVC) is bolted onto the 3 K flange via a Kapton O-ring (hermetically). These two flanges are pre-cooled by the two stages of the pulse tube to temperatures of about 50 K and 3 K. The temperature of 50 K plate is measured with a 1 kOhm Platinum thermometer (pt1000). The temperature of the 3 K plate is measured with a pt1000 thermometer and with a 10 kOhm RuO2 thermometer. These two plates also accommodate high power heaters for quick warm-up as well as charcoal-based sorption pumps. The IVC contains the dilution refrigerator unit and corresponding flanges along with the 10 Tesla Mag-

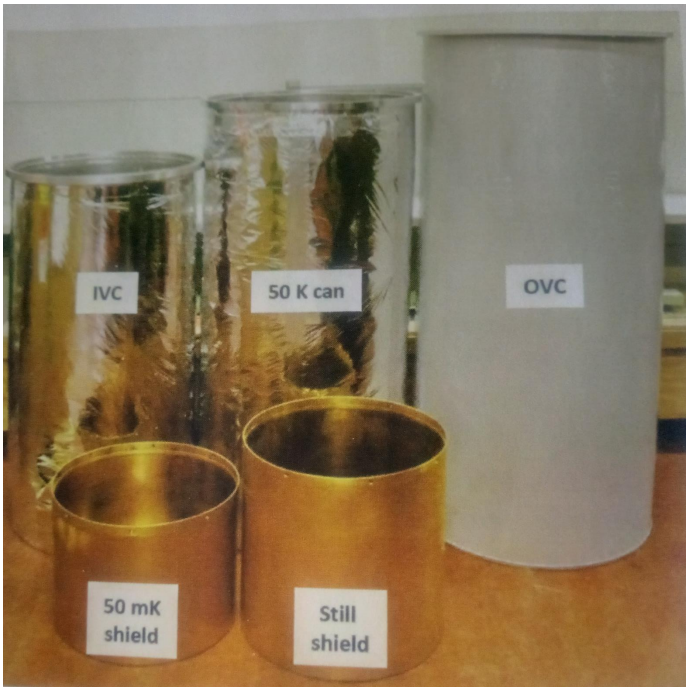

Figure 4.17: **The cylindrical cans with their respective labels (adapted from [69])**

net. Focusing inside the IVC, the dilution refrigerator unit is attached to the 3 K plate via thermally insulating G10 tubes. The unit has a still, 50 mK cold-plate, and a mixing chamber (MC), and a series of counter-flow heat exchangers between the stages. The still is made of stainless steel with a gold-plated copper bottom, where a copper radiation shield is attached. A capacitive level gauge, a heater and a 10 kOhm RuO2 resistance thermometer are all fitted and submerged in the liquid in the still. A Joule-Thomson heat exchanger is installed between the 3 K plate and the still to help condense the ^{3}He -^{4}He mixture. Typically, a cylindrical can is screwed onto the still flange and acts as a radiation shield [69].

Furthermore, a 50 mK plate is fitted between the still and MC for thermal anchoring and extra radiation shielding of the mixing chamber. A continuous heat exchanger and one or more silver sinter heat exchangers are placed between the still and the cold plate. The mixing chamber is made of gold-plated copper, and it has a silver powder heat exchanger of a large surface area. Many samples can be fastened to the mixing chamber. There are one or more silver sinter heat exchangers fitted between the cold-plate and the MC. The mixing chamber is fitted with a calibrated resistance thermometer, pt1000, and a 100 Ohm metal-film

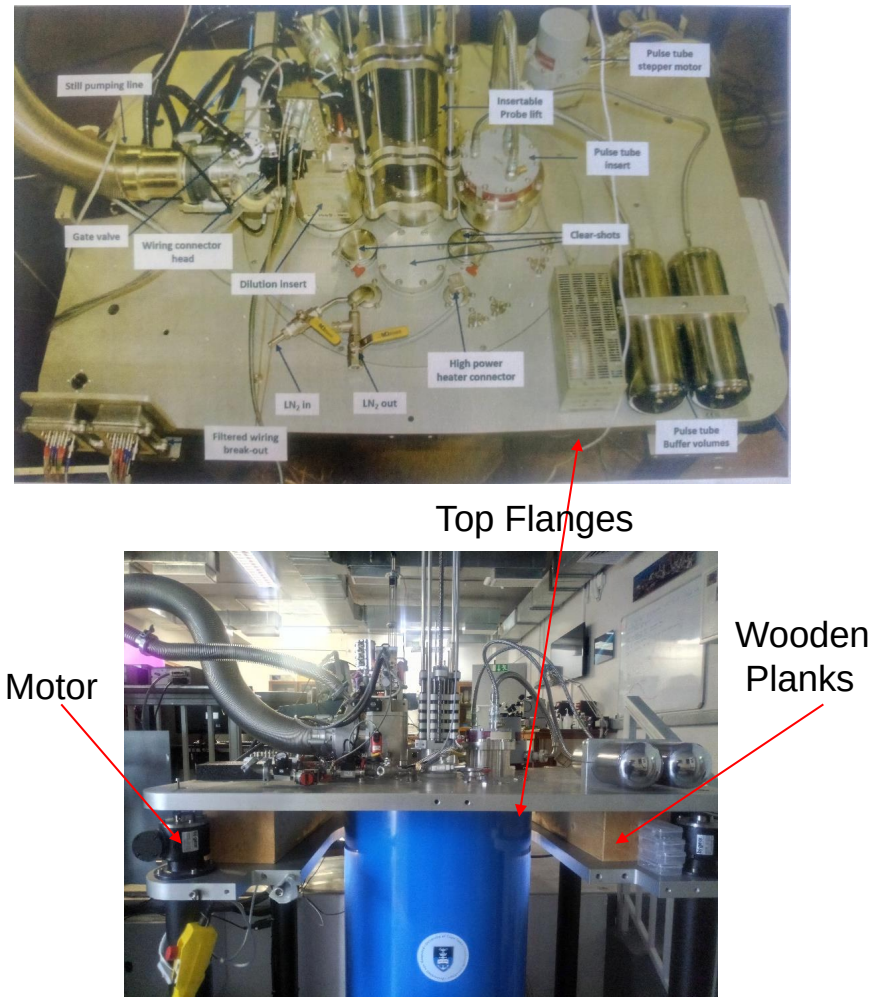

Figure 4.18: **Illustrates the top flange housing a manifold of components, top image (adapted from [69]). The top flange rests on wooden planks and the motor used to lift the flange, bottom image**

heater to monitor cool down. The cylindrical gold-plated copper radiation shield attached to the still plate also contains a simple 30 kg, 10 Tesla solenoid magnet made of NbTi wire, as shown in Figure (4.20). The electrical connections to the sample and data acquisition unit consists of a 24×2 phosphor-bronze wires in a twisted pair going right down to the MC with thermal anchoring at all stages. These typically end up as two 24 pin Fischer connectors on the top flange. Additionally, there is a 10 pin Fischer connector on the top flange for the heaters. Additionally, 12 coaxial cables reach the MC as MMCX connectors and come out at the top flange as Lemo connectors. This basic wring is highly customisable [69].

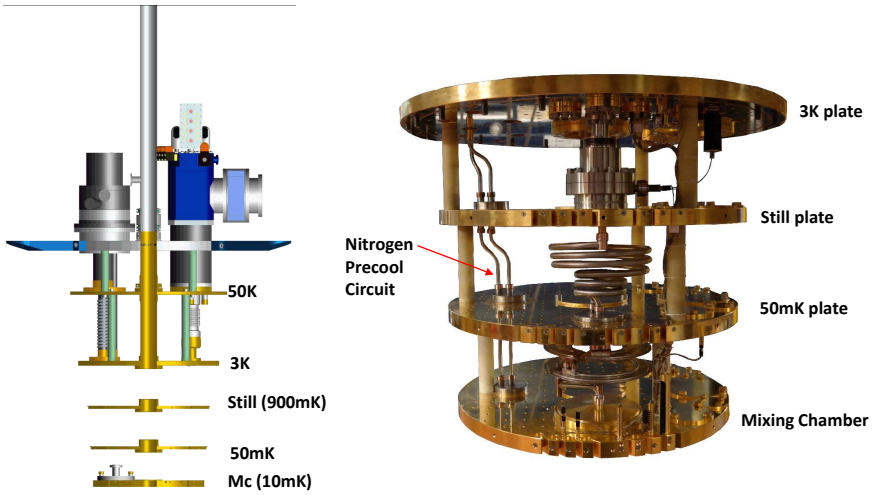

Figure 4.19: **The cold regions of the dilution cryostat unit defined by the five cylindrical flanges. The temperature each flange can reaches upon the operation of the fridge is indicated in the diagram (adapted from [69])**

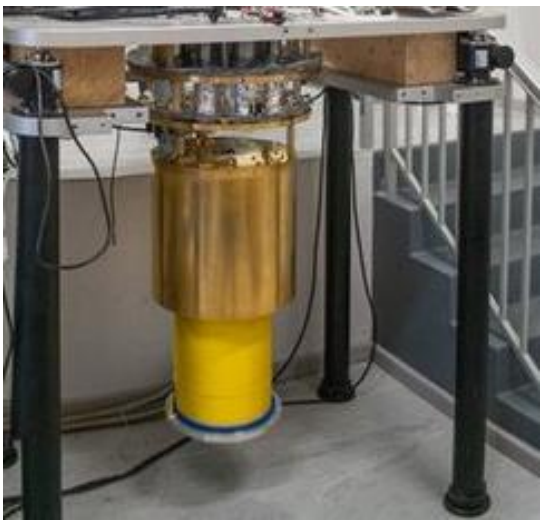

Figure 4.20: **A 30 kg, 10 Tesla solenoid magnet made of NbTi wire**

The next component in the dilution refrigerator system in the gas handling system; the standard GHS is shown in Figure (4.16). The ^{3}He -^{4}He gas mixture used in the dilution unit is stored inside the GHS; from there it is circulated using one or more turbo-molecular drag-pumps and backed by a dry primary pump. A double-membrane compressor is used to condense the mixture. The GHS frame houses many pumps. The scroll pump is specifically used to create a pre-vacuum in the inner and outer vacuum chambers. The stainless-steel frame is made of hol-

low square tubes welded to make two leak-tight reservoirs. The upper one stores the ^{3}He and has a typical volume of 36 liters. The lower one store the ^{4}He-rich mixture and has a typical volume of 144 liters. The front side of the GHS contains the valve and pump control panel, controllers for the turbo pump, maxigauge vacuum gauge controller, quad current source, and high-power heater. From the side doors, one can access all the internal parts of the GHS like the RS-232 to USB multiplexor, power sockets, pumps, compressors, dump valves, the valve board relay box, 24 V supply, etc [69].

A pulse tube cooler, cryomech PT 415 typically with 1.5 W cooling power at 4.2 K, is integrated with the dilution refrigerator unit Figure (4.16). It has a powerful compressor (typically 5 to 10 kW) which compresses and expands helium gas. The compressor is located a significant distance away from the cryostat unit and is connected to it via two flexible stainless-steel hoses, typically 12 m long. It is cooled by a suitable 12 kW water chiller. Leiden provides LabVIEW-based control programs to control and monitor the operation of the fridge and probe. The front panel program controls the valves, pumps, read out the pressure gauge, flowmeter, and the operation of the pulse tube compressor. It keeps a continuous log of the system parameters on the computer, and one can set operation limits for and perform automatic condensation and circulation of the helium gases. A temperature controller program is provided to control and read out the AVS resistance bridge and the LCR bridge. It can read out the resistance thermometer sensors from the AVS bridge. It can also read the resistance sensors, CMN mutual inductance sensor as well as the still level gauge, which is a capacitor sensor. The quad current source powering the various heaters is also controlled by this program. A program is also provided to control the operation for the probe-lift see Figure (4.21). The water chiller, water tank and UPS in Figure (4.22) all sit at a remote location from the fridge. The chiller is outside the lab, and the tank and UPS are in the generator room inside the building [69].

Cooling down sequence:

Upon assembly and closing up the dilution refrigerator, one can start pumping out the IVC. The pumping is done using a turbo pump backed by a scroll pump. A leak detector is used to detect any leaks of the IVC through the Kapton O-ring. While the IVC is being pumped the 50 K shield can and the OVC can is then

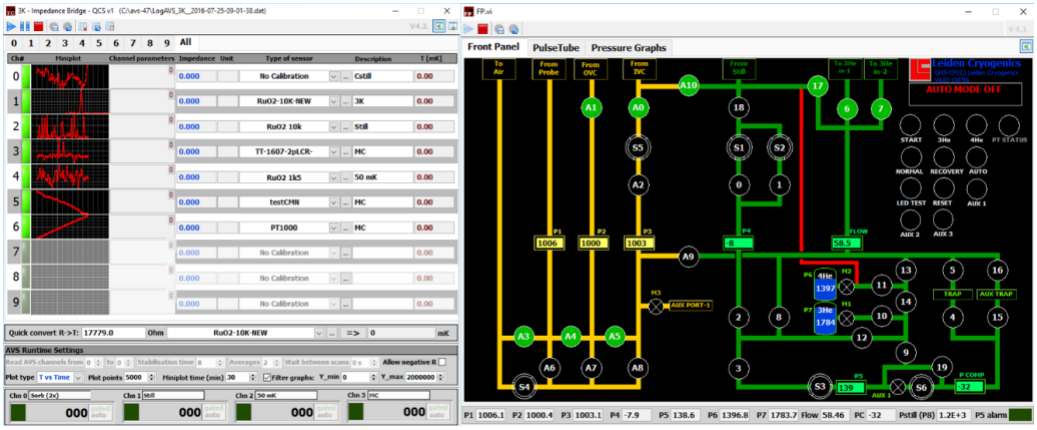

Figure 4.21: **The LabView based control program provided by Leiden. The temperature controller program reads the temperature of the fridge via the impedance bridge, left image, and the front panel of the gas handling system, the pulse tube, and pressure gauges are monitored by the control program on the right image**

Figure 4.22: **Shows the water chiller, ups and water tank**.

assembled. The IVC should be pumped to about a tenth of a mbar. The IVC is flushed 3 to 4 times with helium to remove most of the remaining air. After flushing the IVC, about 10-12 mbar helium is left in the IVC. This helium will be used to cool the flanges below the 3 K flange via convection. The rest of the Dilution Unit, and ^{3}He and ^{4}He traps are then pumped out. The still or dilution unit are pumped to about 10^{-4} mbar. This must be done for several hours (we usually leave it overnight), to remove moisture that could have crept in and could cause a partial or total blockage of the impedances of the lines placed at the still

level. These impedances line typically have small diameter capillaries that cause a pressure drop so that the mixture can condense at a convenient temperature. The OVC is then pumped out via the scroll and small turbopump and leak checked, we keep pumping on the OVC [69].

The pulse tube is then switched on, after ensuring that the cooling water is circulating. The pulse tube is used to pre-cool and liquid nitrogen (LN2) pre-cooling is not used. The IVC and 50 K flanges are in thermal contacts with the cold finger of the Pulse tube. After a sufficient amount of time, the pulse tube will cool these plates by a two-stage process to temperatures of about 3 K and 50 K respectively. The 3 flanges below the 3 K flange will cool down via the 12 mbar exchange gas left in the IVC to about 4 K. At this point, the pressure in the IVC will become lower than 5×10^{-4} mbar due to the charcoal sorption pumps. Sorb pumps are very fast and can absorb a large quantity of gas, typically 300 cc of Helium per gram charcoal. For their operation, such sorb pumps need to be cooled to below the temperature corresponding to the binding energy of the gas to be pumped. For helium this is about 40 K, and the sorb heater is capable of heating the sorb efficiently. The Pt1000 on the mixing chamber and all the other thermometers besides those of the 3 K plate will be stable at some higher temperature to 4 K because there is no exchange gas to equalize the temperatures. At this point, the sorb pumps are heated with about 45 mA through the QCS using the temperature controller program. This releases enough exchange gas, and the IVC pressure rises to 2×10^{-2} mbar to equalise the temperature of all the stages to close to 4 K. The sorb heater is turned off when the resistance is stable and close to 4 K. The IVC pressure will again fall below 5×10^{-4} mbar and the system is ready for mixture condensation [69].

The mixture is condensed automatically. The condensation sequence begins, with first the condensation of ^{4}He and then ^{3}He. At this point, the cooling is governed by the principles given in [67] for the realisation of a dilution refrigerator. The dilution unit consists of the still, a 50 mk cold-plate, and a mixing chamber plus a series of counter-flow heat exchangers between the stages. A Joule-Thomson heat exchanger is installed between the 3 K plate and the still helps to condense the ^{3}He -^{4}He mixture. A continuous heat exchanger and silver sinter heat exchanger is also placed between the still and the cold plate; one or more silver sinter heat exchangers is also fitted between the cold-plate and the MC; all of which helps to

condense the mixture. The still should start cooling as soon as the mixture enters the DR unit circuit. When operating the magnet, one must make sure that it is not operated at a temperature higher than 4.2 K. Upon warming up the fridge, the mixture should be recovered first, the mixture is recovered automatically [69].

The cold-insertable probe:

Our dilution refrigerator was ordered with a cold-insertable probe. Leiden provided an automatic bellow-based probe lift, the cold-insertable probe, and a radiation shield. The cold-insertable probe prevents the experimentalist from having to open the fridge every time a new sample needs to be inserted into the fridge. The probe is highly customizable in terms of the wiring. Besides the standard twisted pairs, coaxial cables with up to hundreds of GHz capability, optical fibres, and a wide variety of connectors, filters, and cold-fingers can be mounted to this probe. The probe has five stages that correspond to the five cooling stages or flanges in the fridge. Each stage on the probe has clamping arms that can be tightened against the flanges in the fridge. The probe is lowered into the fridge by a bellow-based probe lift automatically using a motor-driven mechanism see Figure (4.23) [69].

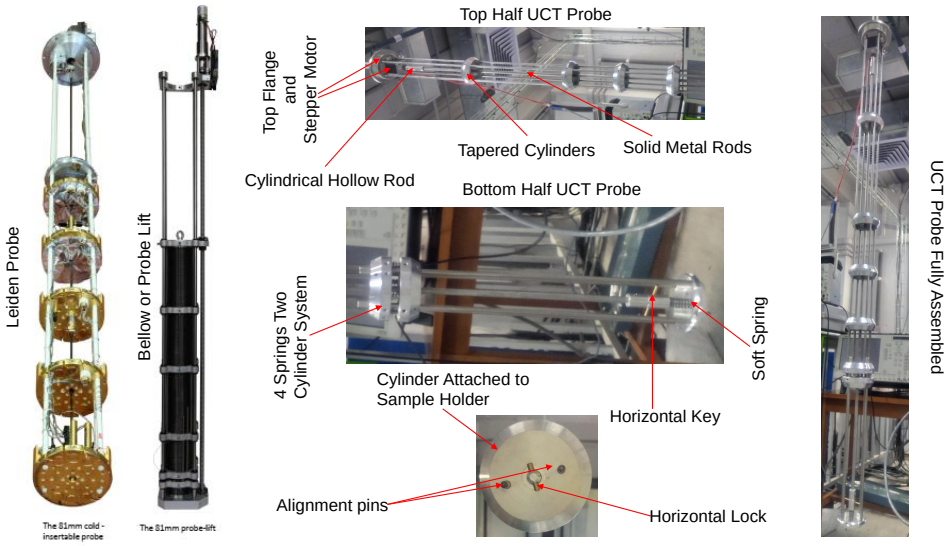

Figure 4.23: **Illustrates the bellow (probe lift) and probe provided by Leiden, and the probe designed by UCT, which is divided into two parts with different components**

The probe we obtained from Leiden introduces a massive heat load into the fridge, and so it does not allow us to cool down to the desired base temperature. We resolved this issue by manufacturing an in-house probe instead of ordering another probe. Leiden's probe is used for its spare parts in other experiments. UCT's probe is composed of two parts: the top and bottom of the probe specially designed to accomplish the functions to follow. The top part consists of a top flange, which is made up of two concentric cylindrical disks, with the thinner disk being the top part of the flange, and a horseshoe bolt is attached to the top disk, it was machined as one entity to form the top flange. A stepper motor is attached to the thicker disk and is electrically connected to the computers via a small Fischer connector protruding through the top disk on the flange. The shaft of the motor is inserted into a thin collar of a cylindrical hollow rod. At the other end of the hollow rod, a solid metal rod is inserted, and this rod goes through 3 tapered concentric cylinders. The centre rod extends through the full length of the top part of the probe. The stepper motor will rotate the rod which rotates the small hollow cylindrical rod attached to it, in doing so it will lock or unlock the sample holder at the bottom part of the probe. All those parts are held together by four additional rods that also go through the tapered cylinder and are in turn held in place by screws. The tapered cylinders are made of aluminium and the solid rods are made of stainless steel because they are less thermally conductive than copper, from which the sample holder is made. The hollow cylindrical rod piece is there to prevent the dock mounted on the cold-tale attached to the MC plate from poping out of place if the probe is lowered too much.

The bottom half of the probe has two tapered cylinders. The lower cylinder is designed to be attached to the sample holder or shuttle. It has the center rod going though its center via a spring system to a small metal rod that sits horizontally at its bottom. This small rod acts as the key to lock or unlock the sample holder to the probe. The center rod then extends to the upper part of the bottom half and it goes through a four spring two chamfered cylinder system. The function of this system is to provide some play when loading the sample holder into the fridge. To ensure that a proper electrical connection is made between the sample holder or shuttle on the probe, and the dock on the tail attached to the MC plate, this spring system gives the experimentalist a play of about 9 mm. If we go beyond that, the spring system will have compressed to its maximum, and the sample holder and the dock will be pushed off the tail, however, as mentioned earlier, this

is prevented by the small hollow rod attached to the stepper motor. The top and bottom halves of the probes are attached by screws. An attractive feature of this probe design is that it has no wires going into the fridge. Its only function is to deposit the sample holder into the fridge, thereafter it is removed, the radiation shield is then used when measuring a sample. This is in contrast to the Leiden probe that contains all the wiring and stays in the fridge for measuring since the sample is attached to it directly for measurements.

Sample holder, dock and cold-tail:

Our sample holder or shuttle system consists of two leadless chip carrier (LCC) sockets that house the actual samples see Figure (4.24). The two sockets are soldered to the printed circuit board (PCB) and they are connected to a pair of two male direct current (DC) connectors and 2 pair of RF Sub miniature push-on (SMP) connectors. Each DC connector is associated with two RF SMP connectors, and these are then connected to one of the sockets. The DC and RF SMP connectors are located at the bottom of the shuttle, and they mate with the shuttle dock in the fridge. The shuttle PCB also has a voltage clamp that prevents the gates from blowing up due to high voltage. Initially, the PCB shuttle was designed to include the alternating current (AC) and DC coupling circuit. This choice was later rejected when we found out the AC signal interfered with the magnetic field measurements. This issue was solved by bypassing this circuit in the PCB and letting the AC and DC coupling happen outside the fridge via a T-shape RF and DC coupler. Mechanically, the shuttle is divided into two halves. The top half is the lid that is attached to the bottom of the probe vai the horizontal rod. The bottom part houses the PCB and all the connectors and it mates with the dock at the bottom of the fridge. The two parts are screwed together by four screws upon closing of the shuttle for loading. The shuttle is also gold-plated copper.

The dock that mates with the shuttle is attached to the cold-long tail bolted onto the MC flange at the bottom of the fridge. The dock has the same pairs of RF and DC connectors associated with the sockets in the PCB. All the wiring has been removed from the probe and it is all done in the refrigerator itself. All electrical connection to the samples in the shuttle is made via the dock. The bottom of the dock makes the required electrical connections with the fridge. RF coaxial and DC wires are used for these connections. The shuttle is then attached

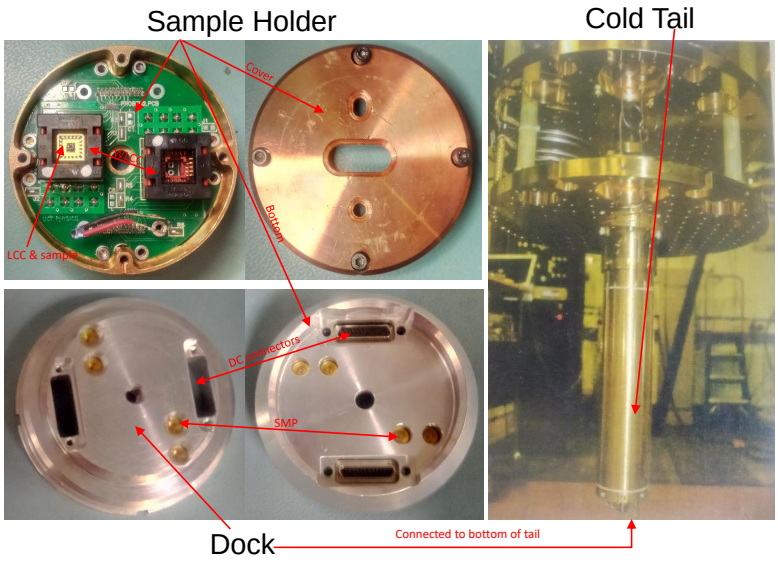

Figure 4.24: **Illustrates the sample holder, the dock which mates with the sample holder, and the cold tail onto which the dock is mounted at the bottom of the fridge**

to the probe by locking it with the program that controls the probe. The probe is inserted into the Bellows and lowered into the fridge until the shuttle mates with the dock. Thereafter, the shuttle is unlocked and the probe is taken out of the fridge while the sample holder or shuttle remains in the fridge ready to be measured.

4.3.3 Source measure unit

The source measure unit (SMU) is an electrical instrument capable of sourcing current and voltage, while at the same time measure voltage or current. It consists of a combination of the useful features of a digital multimeter (DMM), power supply, 'true' current source, electronic loading, and pulse generator, all into a single, tightly synchronized instrument in a compact form. This makes the SMU versatile and highly accurate, making it a more useful instrument than the combination of any of the five instruments [70]. We utilize the model 6430 Sub-Femtoamp SMU depicted in Figure (4.25a). The model 6430's remote PreAmp, shown on top of the SMU in Figure (4.25a), makes it possible for the instrument to have a remarkable measurement integrity. The remote PreAmp offers a very sensitive bi-directional amplifier with sensitive feedback elements for measuring or sourcing currents at

the device under test [71]. The SMU has three terminals: the IN/OUT HIGH and SENSE which connects to the device via triax connectors shown in Figure (4.25c). The other terminal is the MAINFRAME also shown in Figure (4.25c), the high-level signals output by the remote PreAmp are sent from this terminal to the SMU via a two-meter cable. This allows users to make a direct or very short connection to the signal, and thus minimize the effects of cable noise. The front panel of the SMU in Figure (4.25a) shows the controls and display of the SMU: measurement and source function keys, operation keys, range keys, annunciators, source control, and handle. The rear panel of the SMU in Figure (4.25b) shows the connectors of the SMU: Source/measure connectors, remote PreAmp connector, digital I/O, power module, trigger link connector, RS-232 and general purpose interface bus (GPIB) connectors [71].

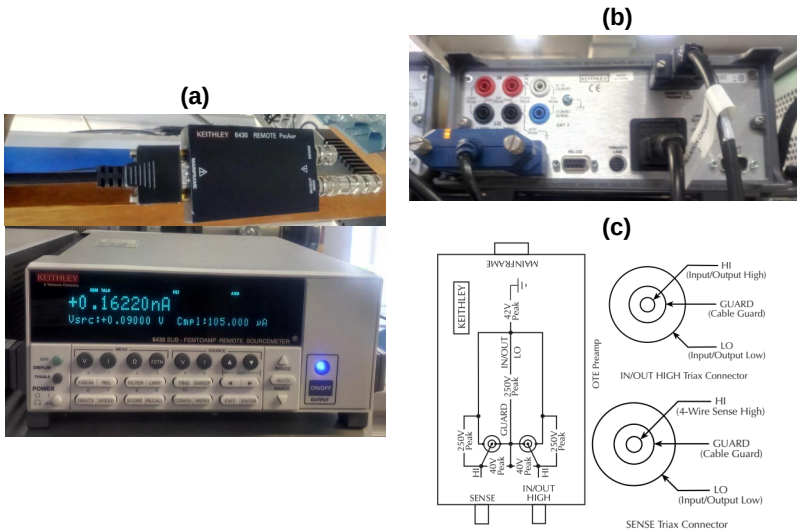

Figure 4.25: **(a) The front panel of the SMU, and the remote PreAmp, (b) the back panel of the SMU, and (c) the schematic of the remote PreAmp along with the Triax connectors (adapted from [72])**

The Model 6430 is extremely useful for single electron and quantum-dot research because it has a typical noise of just 0.4 fA peak to peak (p-p), and it uses a technique similar to lock-in to measure current with a 1 aA sensitivity (10^{-18}A = 6 electrons/second). This Unit has a four-quadrant source and sink operation up to 2.2 W. The unit has a broad source and measurement range: it can source current from 0.5 fA to 105 mA, and measure current from 10 aA to 105.5 mA. It can source voltage from 5 uV to 210 V, and measure voltage from 1 uV to 211

V. Lastly, it can measure resistance from 100 μOhm to 21.1 TOhm. The SMU consists of four filters for averaging or noise reduction. In particular, the repeat filter has a stack with a maximum count of 100. The Model has 0.012 per cent basic accuracy with 5 and a half digit resolution. At 5 and a half digit resolution, the SMU delivers 520 readings/second over the IEEE-488 (this is the GPIB) bus and can store 5 000 readings in its internal memory buffers (two 2 500 point buffers). The NanoElectronics lab at UCT has two Model 6430 and they are both used to measure two samples in the sample holder without having to disconnect and reconnect any of the two samples [71] [72].

4.3.4 Arbitrary waveform generator

A signal generator is any device that creates electronic signals. There are many different types with diverse purposes and applications. Function generators (FG), arbitrary function generators (AFG), and arbitrary waveform generators (AWG) are common types of specialized signal generators. Function generators allow one to generate periodic standard functions such as sine, square, triangle, ramp up/down, DC, and noise. Figure (4.26) shows an analog RF signal/function generator used in this thesis for data acquisition. It offers a frequency range of 250 kHz to 1000 MHz with a 0.01 Hz resolution and +13 to -136 dBm standard output power [73]. An arbitrary function generator is a function generator that has Direct Digital Synthesis (DDS) card and can generate a periodic, user-defined waveform which typically consists of exactly 16 348 points. In contrast to this, arbitrary waveform generators allow one to generate a user-defined waveform of any size [74].

Figure (4.26) shows AWG7122C Tektronix model used in the experimental design of this thesis. It has a maximum sampling rate of 12 GS/s (24 GS/s by interleaving) with a waveform length of 32 M or 64 M (option 01). The amplitude resolution is selectable between 8 bits and 10 bits. The maximum analog amplitude is 2 Vp-p (standard model) 1 Vp-p (option 06). It has two analog output and four marker output connectors. These connectors supply analog and marker signals. The connectors are 50-ohm Sub-Miniature A (SMA) termination, male with DC to 18 GHz operating bandwidth. A handy feature of the AWG is the display screen that shows you an approximate picture of the waveform. The display on the touch screen makes it easier for the user to interact with the AWG without the

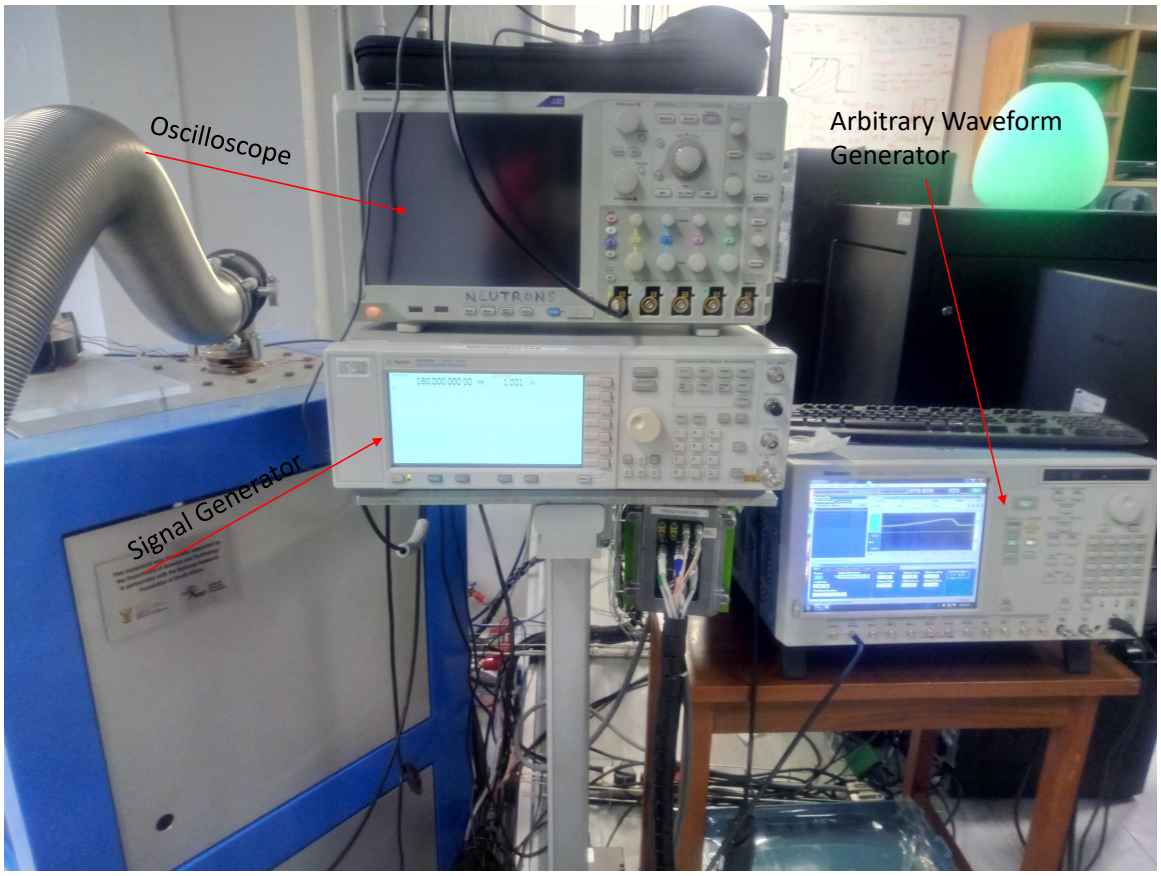

Figure 4.26: **The Agilent E4400B function generator and the AWG7122C Tektronix model arbitrary waveform generator**

use of peripherals such as the keyboard and mouse. The user can typically load the instrument's memory with an arbitrary waveform in several ways: using the equation editor in the AWG to define the waveform and then generate the wave from it. Use an external application such as MATLAB, Excel or other programs to create the waveform and load it to the memory of the AWG in the right file format [75].

4.3.5 Trapezoidal waveform

The trapezoid-shaped pulse waveform in Figure (4.27) is commonly used to approximate a digital clock or data signal. Each pulse is described by an amplitude A, a pulse rise time τ_r, a pulse fall time τ_f, a pulse width τ and the period T. Since the trapezoidal waveform has multiple harmonics of significant amplitude, unlike a sinusoidal signal, it is important to consider the effects of the pulse parameters on the spectrum of the waveform. If we assume that the rise and fall times are

equal, then [76] [77] [78]:

1. At precisely 50% the duty cycle, the spectrum will contain only the odd harmonics.

2. The rise and fall times contribute to the high-frequency spectral content of the waveform. That is, pulses having short rise/fall times have larger high-frequency content than do pulses with long rise/fall times. The level of RF emissions is strongly dependent on the these parameters.

3. Reducing the signal amplitude will reduce the spectral content over the entire frequency span.

4. Reducing the fundamental frequency (at constant duty cycle) will reduce the high-frequency spectral content of the waveform, but does not affect the low frequency content.

5. Reducing the duty cycle (pulse width) while maintaining the fundamental frequency, reduces the low frequency content of the spectrum, but does not affect the high-frequency content.

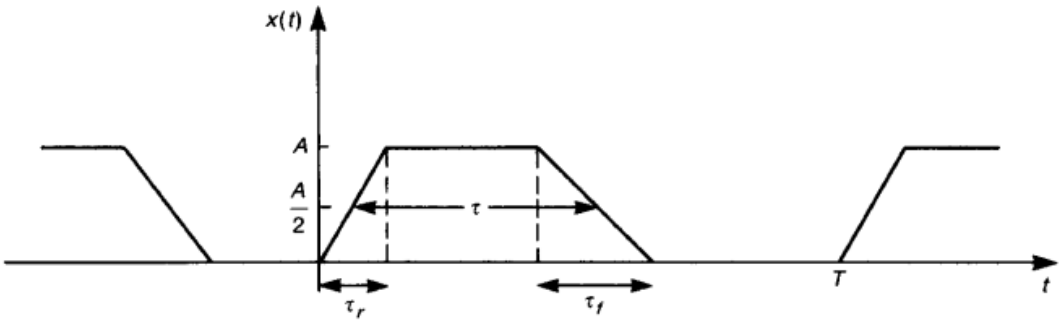

Figure 4.27: **The periodic, trapezoidal pulse train (adapted from [76])**

4.3.6 RF components and wires

The RF components, communication protocols, wires and cables used in the experiments of this report are presented in Figure (4.28). An SMA shorting plug and SMA to SMA male plug and SMA to SMA female socket coaxial adaptors with a 50 Ohm terminations and frequency range of up 18 GHz and 3 GHz are denoted by 1 and 2 respectively. A flexible SMA plug to SMA plug coaxial cable with 50

Ohm and up to 18 GHz is denoted by 4. Adapters N plug to SMA sockets (female) and plugs (males) with 50 Ohm impedance and up to 11 GHz; SMA socket or plug to BNC plugs with 50 Ohm; and a BNC coaxial plug shorting terminator at 50 Ohm with up to 1 GHz are denoted by 3, 7 and 6 respectively. 8 denotes the RG58 BNC plug coaxial cable 50 Ohm matched. The IEEE-488 24 bus line or GPIB is denoted by 11, 12, and 13, which are the GIPB to USB, GPIB adapter, and GPIB to GPIB cable. The USB 2.0 and USB to RS-232 protocols are denoted by 9 and 10. A ZFBT-282-1.5A+ coaxial BIAS TEE SMA sockets and plug with 50 Ohm wideband 10 MHz to 2800 MHz is denoted by 5. 14 shows the 24 pin Fischer connector cable which connects to the refrigerator and the breakout box. Finally, 15 shows the RC low pass filters used at the gates of the pump.

Figure 4.28: **RF components, communication protocols, wires and cables used in the experiments**

Figure (4.29) shows a breakout box and a data acquisition DAQ device. The breakout box consists of various BNC connectors which are labeled alphabetically. These labels correspond to and are mapped to the LCC pads that houses the sample, the gates and Ohmic contacts of the sample. In this way, one knows what is connected to what. It also has a Fischer adapter which connects to the various BNC connectors by mapping the labels to the correct pin on the 24-pin connector.

When the Fischer cable connects to the breakout box via this connector and the sample holder via the connector of the fridge, it connects the DC connectors to the appropriate BNC connector in the breakout box. The black box houses the 4 channel DAQ hardware from National Instruments. The DAQ is used to supply the DC voltages to the selected gates.

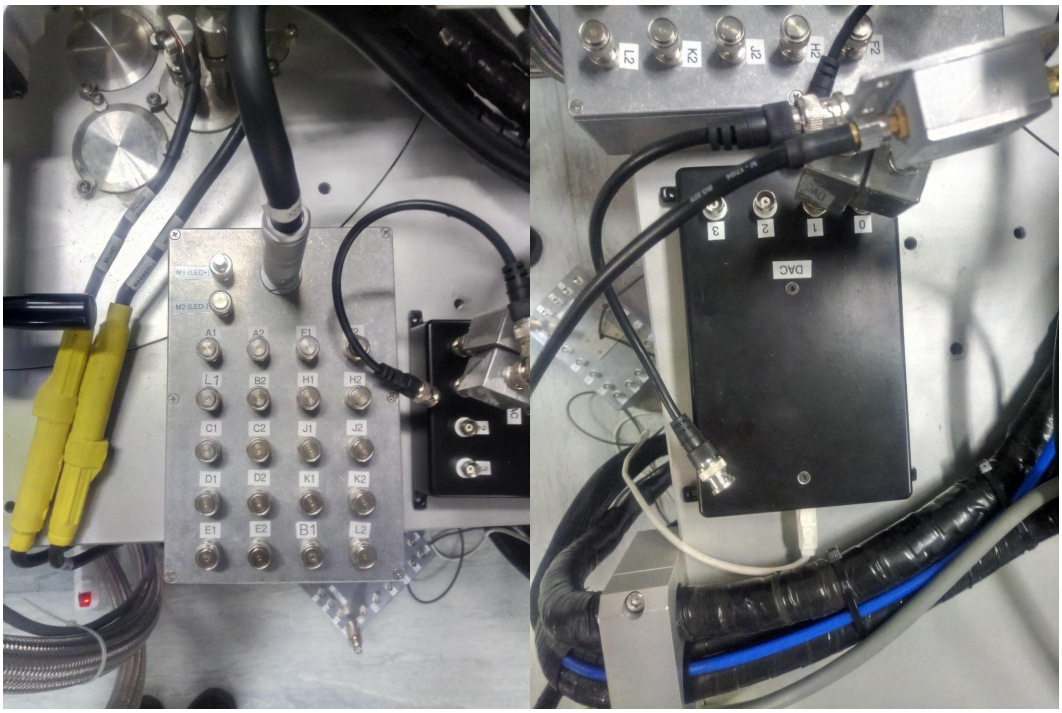

Figure 4.29: **The breakout box, left image and the data acquisition hardware, right image**

4.3.7 Ball bonder optical microscope

The sample is bonded to the LCC via the ball wire bonder shown in Figure (4.30). The system consists of a main head, spotlight, microscope, digital display, area light, right panel, keypad, work table, work-holder, base, and a mouse. The bonder may be equipped with either a Leica MZ6/S6 or stereo zoom microscope. The microscope has a common focus for both oculars. Also, the microscope has an adjustable magnification zoom capability. The wire diameter range is 12.7 to 76 μm gold wire with a 12.7 mm spool. The temperature controller can go up to 250°C plus/minus 0.5°C. The devices are inspected using a Nikon microscope with various zoom modes.

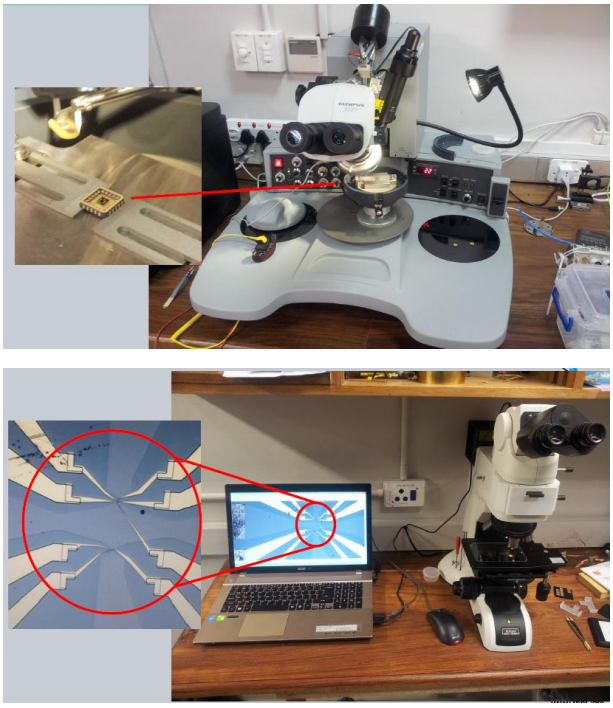

Figure 4.30: **Illustrates the ball wire bonder, top image, and optical microscope, bottom image**

4.4 General Measurement Setup

The fabricated devices were inspected for faults such as damaged gates and impurities trapped in the sample that could potentially alter the resistance of the single-electron pump samples. Those samples that pass this inspection test were thereafter bonded. The samples were then dipped in liquid nitrogen to examine the performance of the gates before inserting the samples in the fridge. The general experimental setup is shown in Figures (4.31) where the instruments discussed in Section (4.3) were interconnected to measure the single-electron pump. The actual setup is shown in Figure 4.32.

The computer (PC) in Figure (4.31) was used to control the data acquisition instruments and the operation of the dilution refrigerator. The computer that was used to monitor the operation of the fridge is on the left, while the remaining two computers on the right were used for the data acquisition. The DAQ PCs were connected to the signal generator, arbitrary waveform generator, source measure unit, and the NI-DAQ devices via GPIB IEEE-488 24, and USB 2.0 respectively. The AWG was in turn connected to the RF port of the Bias TEE device via an

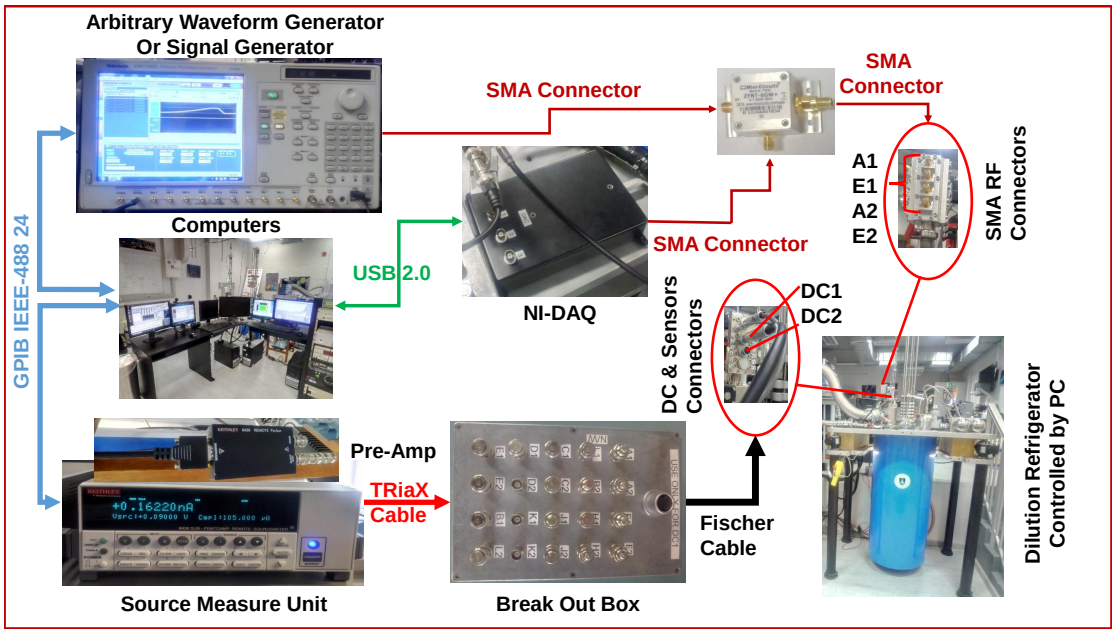

Figure 4.31: **shows the general experimental setup used to measure single-electron pumped current, as setup in the Nano-electronics Laboratory at UCT Physics Department. The signal generators and controllers are on the left (SMU, AWG, and PC), the intermediate components that help to connect to the fridge are in the middle (NI-DAQ and Breakout box) the fridge is on the right where the devices await to be measured. These devices are all connected via the standard interfaces indicated by the arrow lines in blue, green,red, dark red and black**

SMA to SMA adaptor cable, thus providing the required RF signal to modulate the finger gate of the sample to be measured. The source measure unit was connected to the BNC connectors of the breakout box via the preamp and a triaxial cable. The SMU was connected to C2, while K1 was grounded on the box. C2 and K1 are the Ohmic contacts and formed the source and drain part of the sample. The DC voltage supplied by the SMU causes a current drift from the source to the drain (electrons moves from drain to source), which is from C2 to K1. We recall that the preamp is used to allow one to measure the current at the pA scale and that due to such a large resistance, the guard was not used.

Channel 1 of the Ni-DAQ was connected to a T-type BNC connector which was in turn connected to two BNC to BNC cable and these cables were connected to D1 and B2 on the breakout box via gate filters. The gate filters are needed to prevent any high-frequency voltage spikes from damaging the gates on the sample.

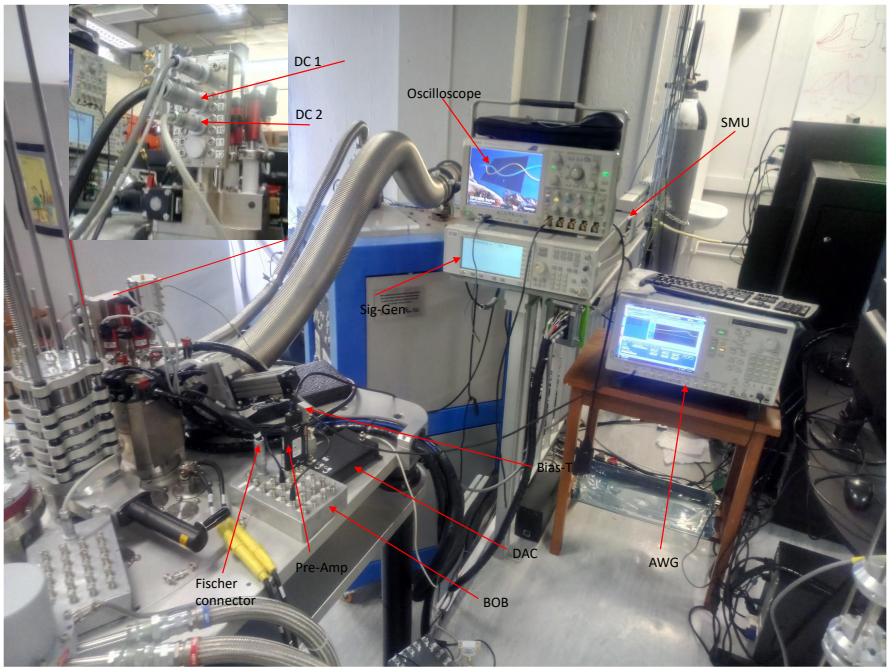

Figure 4.32: **The actual measurement setup**

D1 and B2 supplied the split gate of the pump with a negative DC voltage. The other BNC connectors of the breakout box were either grounded or floating. The Ohmic contacts not used were left floating to prevent current from flowing to the Ohmic and thus creating an ambiguous path for the current. The unused Schottky gates were grounded so that it had a definite reference voltage and thus prevented the gates from blowing up. The breakout box was then connected to the fridge via a Fischer cable either to the DC1 or DC2 Fischer connectors on the fridge, depending on the sample to be measured.

Channel 2 of the NI-DAQ was connected to the Bias TEE via an SMA to SMA connector cable, and the bias TEE combines the DC and the RF signal and sends it to the finger gate of the sample in the fridge through rigid SMA connectors. These terminals are connected to the sample in the fridge via the internal wiring as explained in Section (4.3). These wirings terminate on the tail of the cylinder attached to the mixing chamber, where the sample awaits to be measured. The sample was connected as illustrated in the schematic of Figure (4.33). The schematic clearly shows which voltages are applied to which gate on the sample inside the fridge. Figure (4.34) shows the Auto CAD design of the sample and the scanning electron microscope (SEM) image of the device. The gate pinch-off characteristic of the sample in Figure (4.34) is illustrated in Figure (4.35). The

finger-gate pinches-off at -374 mV and the split-gate pinches-off at -750 mV, as illustrated.

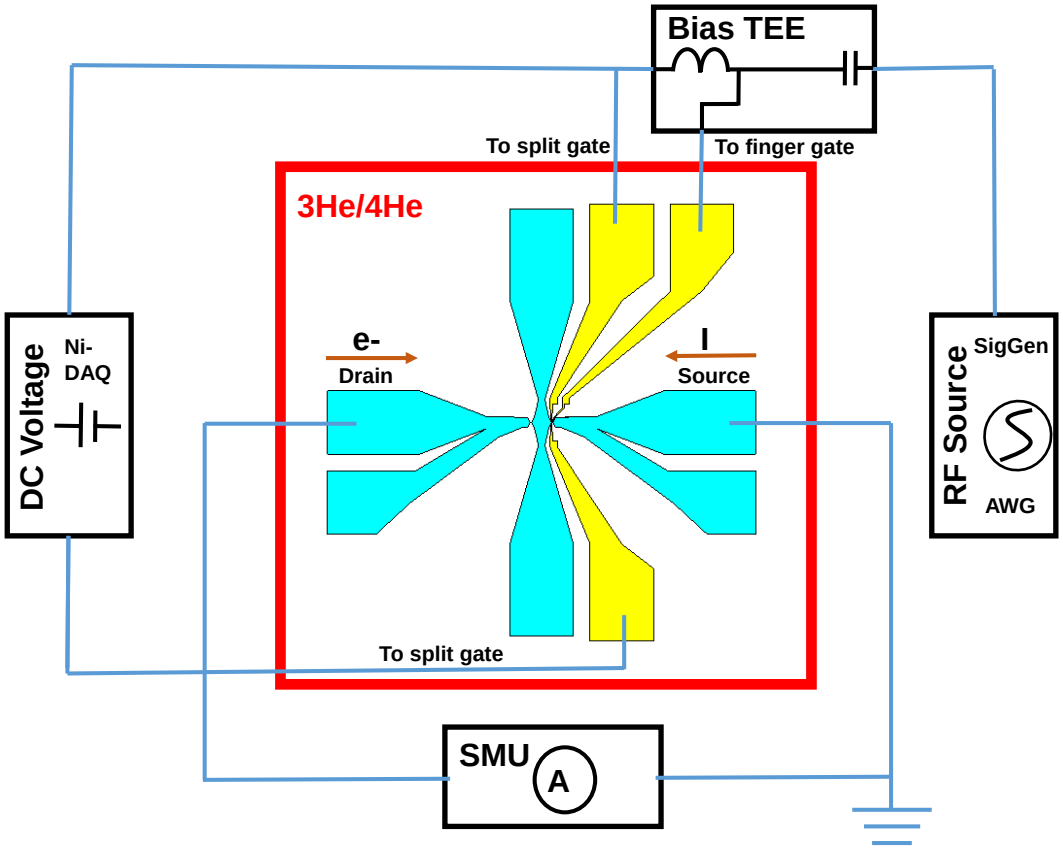

Figure 4.33: **Illustrates the schematic of the sample in the fridge as its gates are connected to the external RF source, SMU, NI-DAQ, and Bias TEE. The Bias TEE connects the finger-gate, the SMU connects to the Ohmic contacts (source and drain) and the split-gate is connected to the DC sources (NI-DAQ).The actual sample is shown at the bottom of Figure (4.30)**

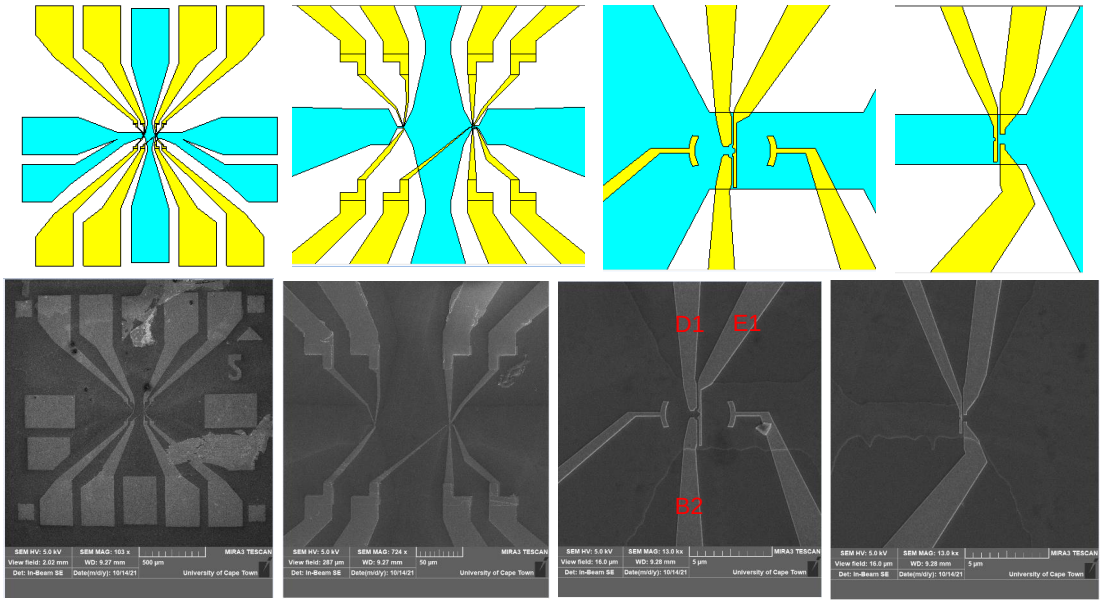

Figure 4.34: **Illustrates the Auto CAD design of the device on top and the actual scanning electron microscope (SEM) device on the bottom**

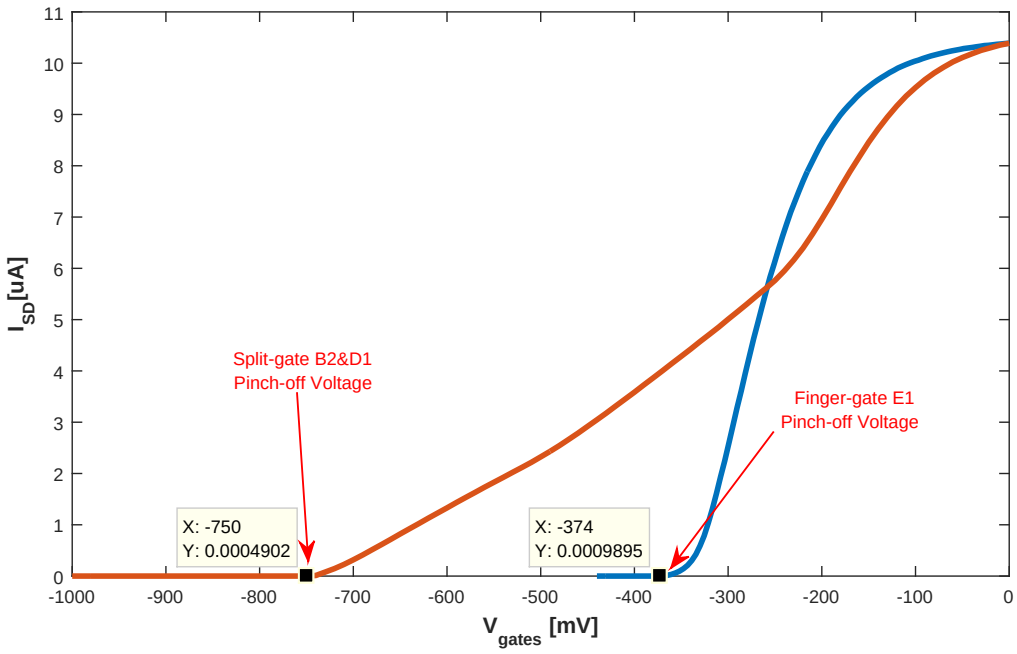

Figure 4.35: **Show the finger-gate and split gate characteristic of the device illustrated in Figure (4.34). The finger-gate E1 pinches-off at -374 mV and the split-gate B2 and D1 pinches-off at -750 mV**

Chapter 5

Data Collection Procedure, Results And Discussions

In Section (4.1), we presented an overview of the techniques required to grow and pattern low dimensional semiconductor heterostructure devices at the nanoscale. Using this information, we described the process used to fabricate the GaAs/AlGaAs single-electron pump sample in Section (4.2). Furthermore, in Section (4.3), we reviewed the instruments required to detect single-electron phenomena due to charge and energy quantisation. The chapter concludes with the experimental setup that we used to measure the quantised current through the sample depicted in Figure (4.33), of Section (4.4). We studied the effect of different waveforms on the sample and present the outcomes of the experiments in Sections (5.1), (5.2) and (5.3), in this chapter. The waveform sources are the signal generator and an arbitrary waveform generator. In particular, Section (5.1) discusses the effect an AWG sinusoid has on the pumped current by comparing it to the conventional pumped current produced by a signal generator sinusoid. Section (5.2) discusses the effect a trapezoidal waveform with different rising edge slopes has on the pumped current. The rising edge slopes are sinusoidal segments of different frequencies. Finally, Section(5.3) discusses the tuning of the pumped current plateaus with a source-drain bias voltage.

5.1 Experiment A: The Effect of the AWG Sinusoid on the Conventional Pumped Current

This experiment compares the pump maps produced by a sinusoidal waveform from a signal generator and an arbitrary waveform generator. We configured the signal generator to output an RF sine wave with an amplitude of 353.55 mV RMS (1 Vp-p) at a frequency of 180 MHz. These are the necessary parameters used to describe a waveform on the signal generator. An arbitrary waveform generator is different because we have to specify the record length and sampling frequency, then calculate the signal frequency from these parameters. We configured the AWG to output a sinusoidal signal with an amplitude of 1 Vp-p (353.55 mV RMS), a sample rate of 9 GS/s and a record length of 50 points in one cycle, resulting in a waveform with a frequency of 180 MHz and zero phase shift. A 10 GS/s oscilloscope display the output signals in Figure (5.1a and 5.1b). It is difficult to tell which instrument the waveforms belong to in the time domain analysis.

However, the frequency domain analysis gives more insight into the difference between the two signals. Figure (5.1c and 5.1d) shows the fast Fourier transform spectrum of the two signals, and there is a clear difference between them. The signal generator only produces three tones, and it drastically suppresses the higher-order harmonics, as shown in Figure (5.1c). By contrast, the AWG produces highly pronounced higher-order harmonics spanning the entire 6 GHz of the spectrum analyser, as shown in Figure (5.1d). Some of its higher-order harmonics are greater than -50 dBm, dominating even some of the lower-order harmonics. The difference is attributed to the way the instruments synthesis their waveforms. The signal generator is by design a more specialised instrument than the AWG. It produces very stable standard waveform shapes such as the sine and square waves-that are both accurate and agile [79]. By contrast, for the AWG, the sample rate and the record length affect the frequency and fidelity of the main output signal [79]. Figure (5.2) presents the pump maps of the sinusoids. The numbers 0, 1, 2 and 3, inside the coloured rectangles on top of Figure (5.2a), denotes the number of plateaus. The colour of the rectangles corresponds to the colours of the pump map. For example, the number 1 inside the light blue rectangle means the first plateau, and the colour tells us which regions on the pump map corresponds to the first plateau. The same applies for number 2, 3, etc. The dark red region on the pump map is saturation of the current because of the 100 pA range of

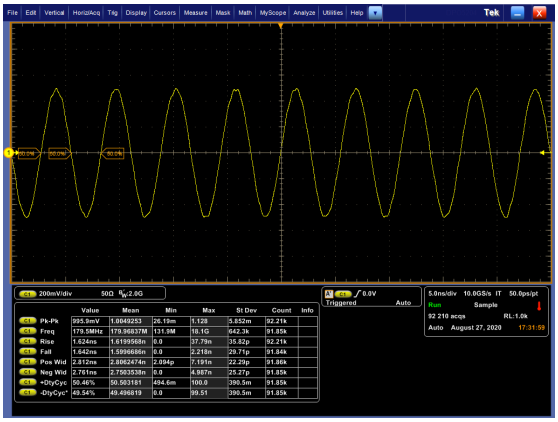

(a) The sine wave from the signal generator at 1 Vp-p and 180 MHz

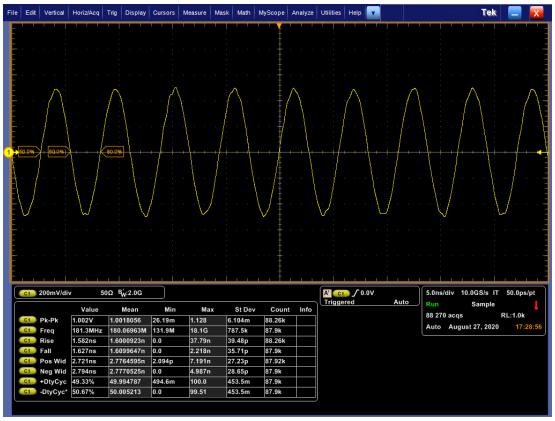

(b) The sine wave from the arbitrary waveform generator at 1 Vp-p, 9 GS/s and 50 sample points (180 MHz)

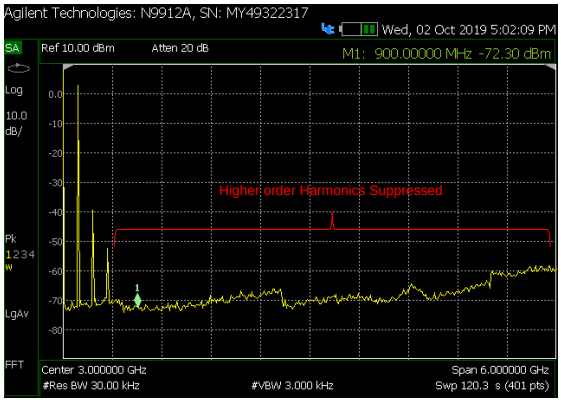

(c) The fast Fourier transform of the signal generator sinusoidal waveform

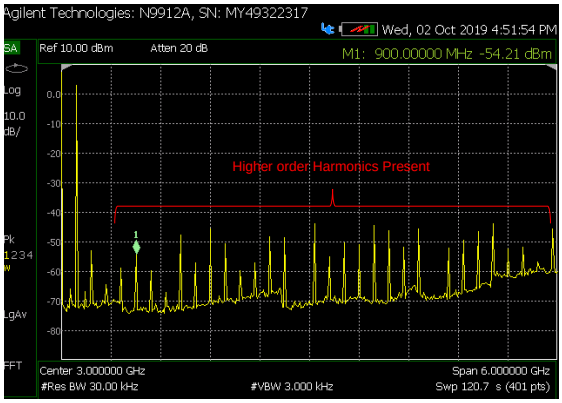

(d) The fast Fourier transform of the arbitrary waveform generator sinusoidal waveform

Figure 5.1: **The time and frequency domain analysis of the AWG and SG sinusoids. The sinusoidal waveform of (a) the signal generator and (b) the arbitrary waveform generator as monitored on a 10 GS/s oscilloscope. The sinusoidal spectrum of (c) the signal generator and (d) the arbitrary waveform generator as monitored on a spectrum analyser. The higher-order harmonics are suppressed in (c) but are present in (d)**

the electrometer. We will indicate the use of this notation throughout this chapter.

5.1.1 Robustness of the pump maps in entrance voltage

Figure (5.3) shows the numerical derivative of the pump maps. An obvious difference between Figure (5.3a and 5.3b) is the span of their plateaus along the interval

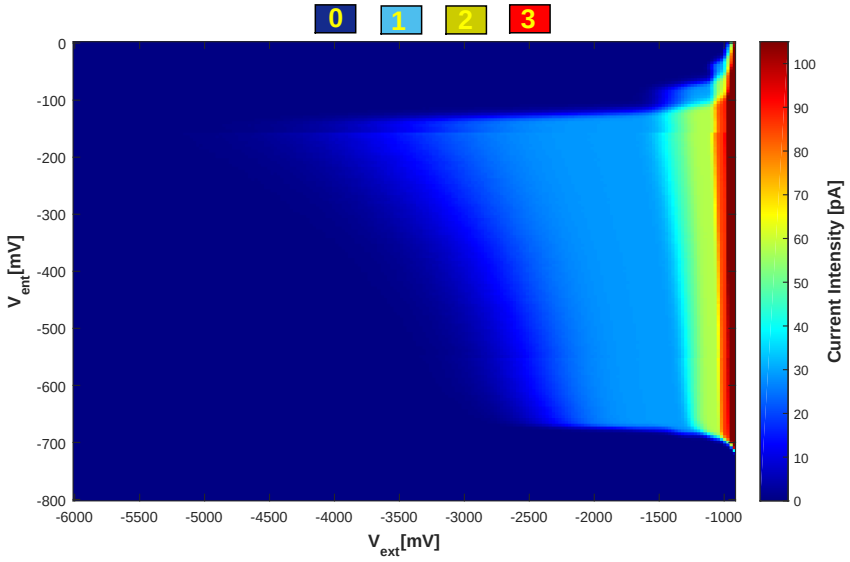

(a) Signal generator pump map for a 1 Vp-p sinusoid at 180 MHz

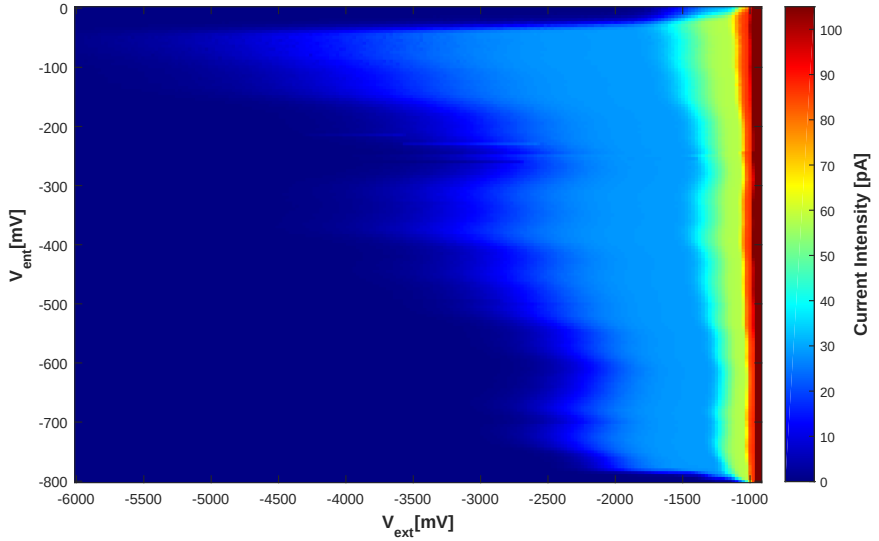

(b) AWG pump map for a 1 Vp-p sinusoid at 180 MHz due to a rate of 9 GS/s and 50 sample points per cycle

Figure 5.2: **Shows the difference in the pump maps of the signal generator (a), and the arbitrary waveform generator (b). For both maps, the first plateau is approximately 28.8 pA, the second is 57.6 pA and the third is 86.4 pA. Each data point on the map was acquired by averaging over 10 data points**

of the entrance gate voltage (Y-axis). We indicated this span with a double-sided red arrow line. The pump map of the AWG spans almost the entire entrance

voltage range. By comparison, the pump map of the signal generator spans approximately six-eighths of the entrance voltage range. If we use the length of the first plateaus to measure the robustness[1] in the entrance gate voltage of each map, then Figure (5.3a) spans a range of 600 mV from -100 mV to -700 mV, and Figure (5.3b) spans a range of 760 mV from -30 mV to -790 mV in entrance gate voltages. We emphasise this point further in Figure(5.4), which is a plot of a vertical line cut at an exit voltage of -1700 mV, through the first plateau of both maps. Where $< \mathrm{N} > = I_p/ef$ on the Y-axis is the average number of electron(s) pumped per cycle; I_p is the pumped current referenced to the first plateau ef. Notice the wider robustness window of the AWG.

5.1.2 Ripples on the onset lines of the pump maps

The other difference between the pump maps in Figure (5.3) manifests as ripples on the onset line (yellow line) of Figure (5.3b). In Section (3.1.5), we defined the onset line as the vertical line boundaries (only for the ideal pump map, practical pump maps have slanted lines), which is set by the outcome of the charge capture process. That is, the onset line is the boundary between the average number of electron(s) captured. The onset line of Figure (5.3a) is smooth in comparison to Figure (5.3b). There are ripples on the onset lines between plateaus 0 and 1 as well as plateaus 1 and 2, in Figure (5.3b). We visualise the degree of the ripples in Figure (5.5). It plots the average number of electron(s) versus the entrance voltage at the exit voltages of -3000 mV and -1400 mV for each pump map. The purple and orange curves have extreme ripples in comparison to the yellow and blue curves. Furthermore, we plotted an onset line for each pump map between plateaus 0 and 1, in the exit voltage interval of -4000 mV to -2000 mV in Figure (5.6). Notice the severity of the ripples on the onset line (orange curve) due to the AWG, compared to the smoother onset line (blue curve) due to the signal generator.

The discrepancies in the robustness and ripples between the pump maps of Figure (5.3a and 5.3b) can be attributed to the different ways the two RF sources

[1]The term 'robust' is adapted from [53]. It is the range of entrance voltages, along which the number of loaded electrons equals the number of unloaded electrons ($\mathrm{n}_u = \mathrm{n}_l$). It is also the range of exit voltages, along which the number of the pumped electron(s) remains the same. Therefore, the larger the range of these voltages, the more robust the pump is.

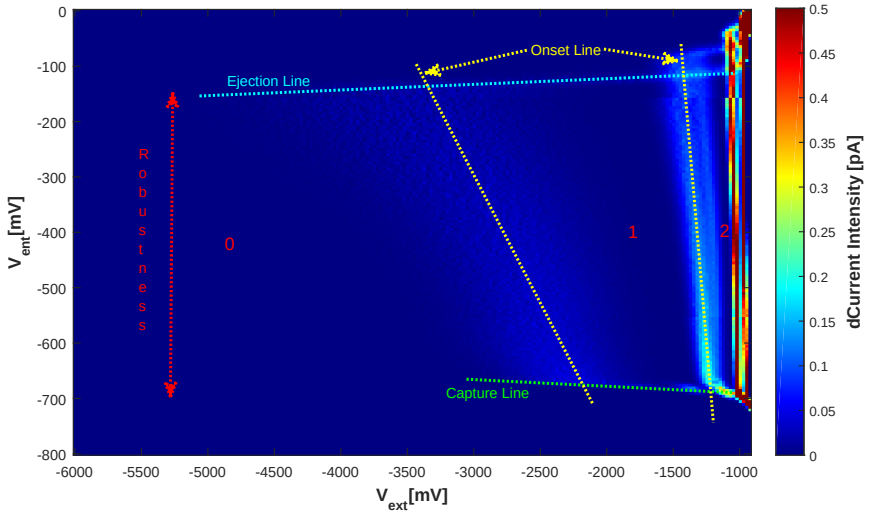

(a) The numerical derivative of the signal generator pump map

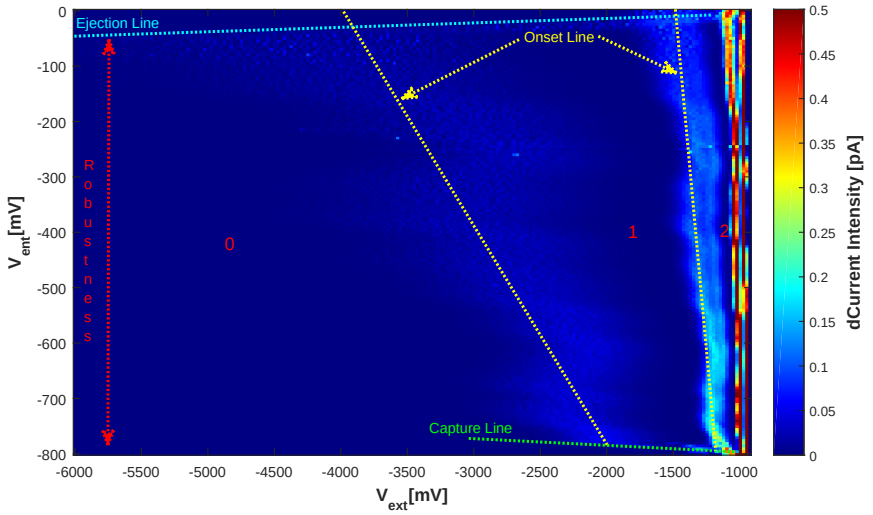

(b) The numerical derivative of the AWG pump map

Figure 5.3: **Illustrates the difference in the numerical derivative of (a) the SG and (b) the AWG pump maps**

synthesise their waveforms. Figure (5.1c and 5.1d) shows the difference in the spectrum of the two output signals. The signal generator produces an accurate sinusoid, and it is conventionally used as the RF source in single-electron pumps. Hence, its pump map looks very similar to those discussed in the literature. By contrast, the arbitrary waveform generator produces a spectrum that contains many higher-order harmonics, which might be the cause of the extreme ripples we

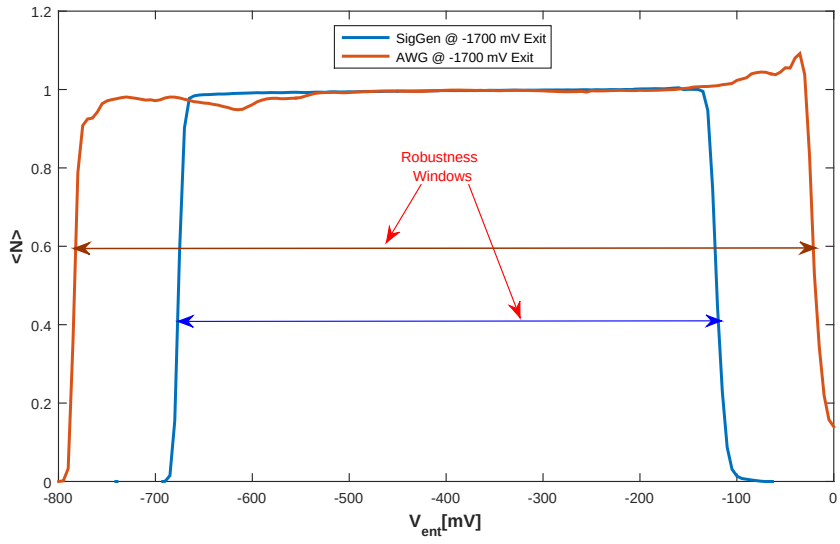

Figure 5.4: **Shows the difference in the robustness window of the first plateau for an exit voltage of -1700 mV due to the signal generator (blue) and the AWG (orange). The AWG has a wider robustness window**

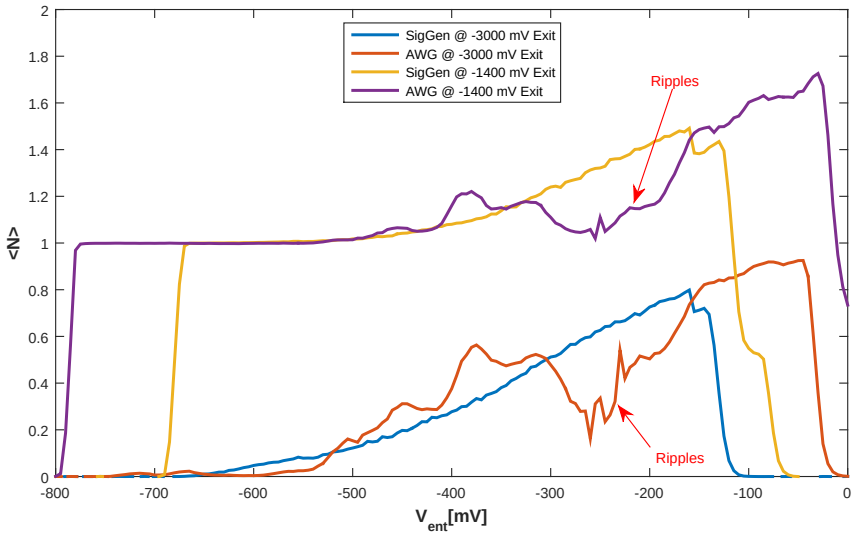

Figure 5.5: **Compares the degree of ripples on the vertical lines cutting the onset lines of the AWG pump map (purple and orange curves) and the SG pump map (yellow and blue curves) at exit voltages of -3000 mV and -1400 mV. The vertical lines of the SG pump map is fairly smooth**

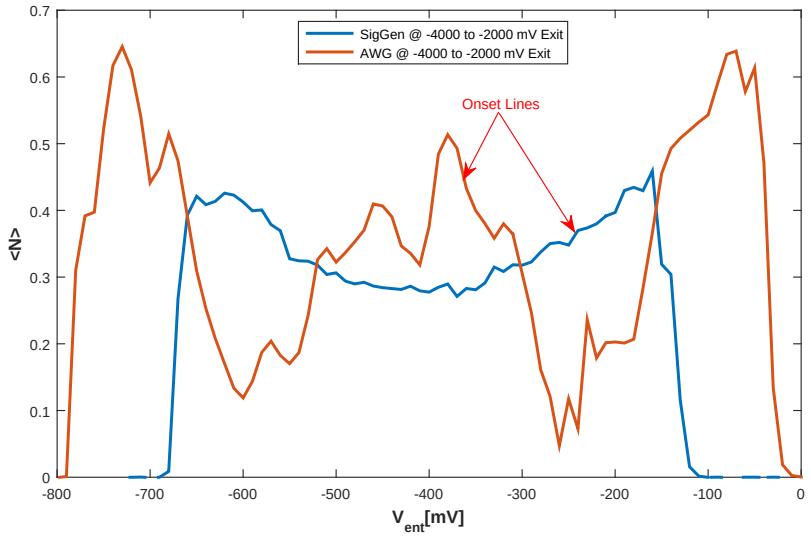

Figure 5.6: **Compares the ripples on the onset line (between plateaus 0 and 1) of the AWG (orange) to the smoother onset line of the SG (blue) in an exit voltage interval from -4000 mV to -2000 mV. The AWG pump map has extreme ripples on the onset line**

observed on the onset line of Figure (5.3b). Furthermore, the fact that the arbitrary waveform generator produces a more robust pump map in entrance voltages suggests that it outputs a higher power at the sample end compared to the signal generator. Even so, we have to conduct further analysis of the nature of these waveforms to enhance our understanding of how they couple to the pump sample.

5.1.3 Pumping in the long plateau regime

Additionally, we observed and plotted plateaus in the long plateau regime (LPR), as discussed in Section (3.2.2), in Figure (5.7) at different entrance voltages. We measured the length of these plateaus to be approximately 500 mV in the exit voltage interval from -2250 mV to -1750 mV, as indicated by the red box. The AWG stretches and shifts the long plateaus, making them a bit more robust in the exit voltage, for the entrance voltage interval from -80 mV to 50 mV compared to the selected plateaus of the signal generator in the same entrance voltage interval. Below an exit voltage of -3000 mV, we notice fluctuations in the transition line between the 'tails' and 'shoulders' of these long plateaus caused by the higher-order harmonics discussed in Section (5.1.2). The reason we are observing these

long plateaus for both sinusoids is because we are using a split-finger gate pump geometry, and the potential of the split gate is much lower than that of the entrance gate, even at very high voltages on the split gate as described by the model in Section (3.2.2).

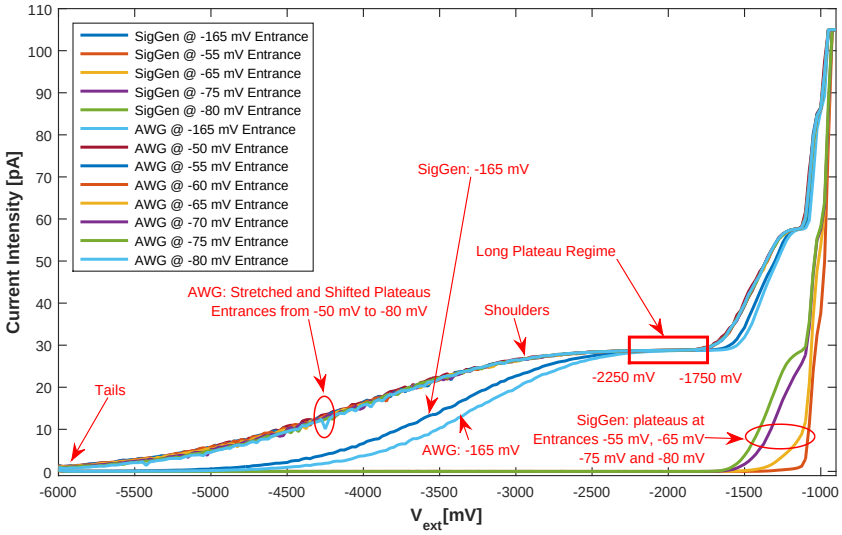

Figure 5.7: **Illustrates the differences in the pumped current for the signal generator at -165 mV and the AWG at -165 mV and from -80 mV to -50 mV in entrance voltages. We see pumping in the long plateau regime in the exit voltage interval from -2250 mV to -1750 mV (a 500 mV window). Notice how the plateaus in the interval from -80 mV to -50 mV are stretched and shifted and hence are more robust in the exit voltage due to the AWG, compared to the selected plateaus in the same interval for the signal generator**

5.2 Experiment B: The Effect of a Trapezoidal Waveform on the Conventional Pump Map

In Giblin's et al. [25] experiment, he used a trapezoidal waveform to modulate the entrance gate voltage of the standard finger-finger gate sample geometry. His results showed that a sufficiently 'slow' sinusoidal segment on the rising edge of a trapezoidal pulse could 'recover' pumping, where a sinusoid at the same frequency did not pump. In this section, we conducted a similar experiment using the split-finger gate sample geometry shown in Figure (4.33). We kept the pulse width and rise time of the trapezoids constant at 0.5 and 4 ns, respectively. By contrast, Giblin et al. [25] varied these quantities in his experiments. The slopes on the rising edge of the trapezoidal pulses are sinusoidal segments. We varied these slopes by using sinusoids of different frequencies. We used the waveforms in Figure (5.8a), where B.1 to B.5 are the waveforms with sinusoidal segments of periods T = 16, 20, 25, 30, and 40 ns or equivalently frequencies f = 62.5, 50, 40, 33.3, and 25 MHz respectively. The slopes decrease from B.1 to B.5, shown in blue to green in Figure (5.8a). The output pulses of the AWG have an amplitude of 1 Vp-p, sampled at 12 GS/s, with 66 sample points per cycle, to give a frequency of 181.81 MHz. Appendix A contains the waveforms monitored on a 10 GS/s oscilloscope. We measured the sample inside a dilution fridge at a temperature of no more than 150 mK. We applied a source-drain bias of 10 mV to the ohmic contacts. Then we stepped the entrance gate voltage in increments of 5 mV in the interval from 0 mV to -800 mV and swept the exit gate voltage from -900 mV to -6000 mV in steps of 25 mV.

5.2.1 Robustness of the pump map in exit voltage

Wright et al. [54] observed that the quantised current is robust along the exit voltage when an applied magnetic field is perpendicular to the sample. Our experimental results show that the quantised current is extremely robust in exit voltage at zero externally applied magnetic field. We observed this effect for all five waveforms in Figure (5.8a). In some cases, such as the one in Figure (5.8b, 5.8c and 5.8d), plateaus 1, 2 and 3 are all elongated over a 4 V range in the exit voltage. In other cases, such as those of Figure (5.8e and 5.8f), the first plateau is elongated over a smaller range similar to that in Section (5.1). This means that we

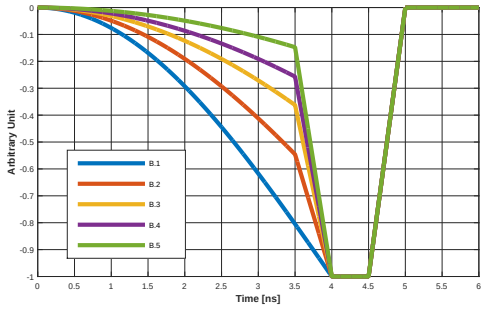

(a) Trapezoidal Pulse waveforms: B1 to B5 with sinusoidal segment of different frequencies or slopes

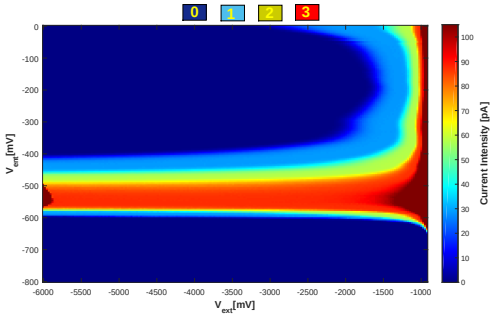

(b) Pump map of pulse B.1 (blue) with 62.5 MHz sinusoidal segment

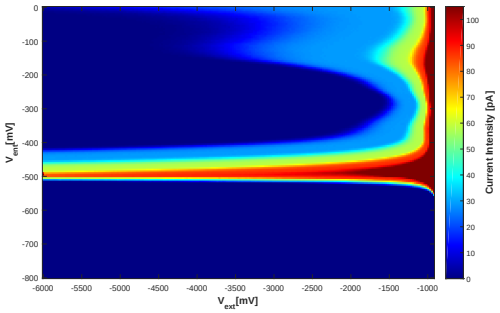

(c) Pump map of pulse B.2 (orange) with 50 MHz sinusoidal segment

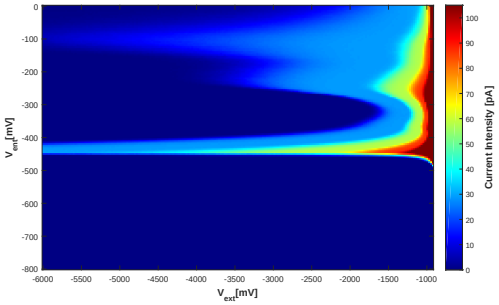

(d) Pump map of pulse B.3 (yellow) with 40 MHz sinusoidal segment

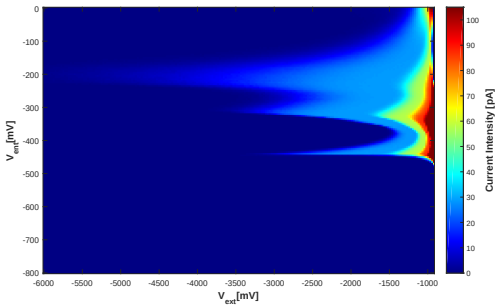

(e) Pump map of pulse B.4 (purple) with 33.3 MHz sinusoidal segment

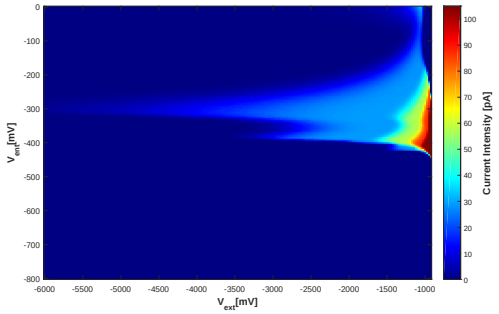

(f) Pump map of pulse B.5 (green) with 25 MHz sinusoidal segment

Figure 5.8: **Shows the Trapezoidal waveforms with sinusoidal segments of different frequencies, B.1 to B.5 in (a) and their corresponding pump maps in (b) to (f). These pulses were operated at a frequency of 181.81 MHz and an amplitude of 1 Vp-p. The first, second, and third plateaus of the pump maps have numerical values of 28.8 pA, 57.6 pA, and 86.4 pA on the colour bar, respectively**

are pumping in the long plateau regime discussed in Section (5.1.3). The results therefore, suggests another way to improve the accuracy of the pumped current. A probable cause to this effect is the induction of a local magnetic field at the sample due to the modulating pulse waveforms. However, subsequent modelling[2] of the RF signal on the finger-gate predicted that the magnetic field strength $B = \mu_0 \times H$ is approximately 2.5 uT at best. In the work done by Wright et al. [54] and Kaestner et al. [56] we notice that the external magnetic fields applied in their experiments are at least 5 orders of magnitude larger than the locally induced magnetic field. This field is not nearly strong enough to create magnetisation worth considering seriously. Thus, it might not account for the effect being observed.

5.2.2 Fast slope restored pumping

From the results of Figure (5.8b to 5.8f) it is immediately apparent that the pump map deteriorates[3] as the slope of the sinusoidal segment of the pulses decreases. That is, some plateaus begin to disappear, and they become less robust in exit voltage, in the entrance voltage interval from -400 mV to -600 mV. This observation seems contradictory to the conclusion reached by Giblin et al. [25], who showed that the pumped current is restored by a slower sinusoidal slope. However, this might not be the case since there are key differences between our experiment and Giblin's. We used a split-finger gate geometry as opposed to a finger-finger gate geometry. We modulated the pump with five pulses instead of two and operated our pumps over wider entrance and exit voltage ranges. Furthermore, Giblin et al. [25] does not show a pump map, making it difficult to determine the entrance voltage value at which he chose the pumped current. Even though the pump maps are degrading in the entrance voltage interval from -400 mV to -600 mV, it simultaneously restores in the lower entrance voltage intervals from -50 mV to -250 mV in Figure (5.8c and 5.8d) and from -200 mV to -300 mV in Figure (5.8e and 5.8f). Giblin et al. [25] might have considered the quantised current in an interval of the entrance voltage where the plateaus restored. Thus, it is challenging to compare

[2]The modelling was done in an Electromagnetic Field Simulation software called CST STUDIO SUITE [80].

[3]In the context of this thesis, the terms 'deteriorate' and 'degrades' will be used synonymously to mean that the pump map loses its plateaus or that the plateaus are becoming less robust in exit and entrance voltages.

the two experiments. Our results indicate that the pumped current restores with a steeper slope from pulses B.5 to B.1 in the entrance voltage intervals from -400 to 600 mV.

5.2.3 The dynamics of the pumped current

Let us turn our attention to the pump map in Figure (5.8b) of pulse B.1 and inspect it more carefully. This pump map is interesting because the first, second, and third plateaus remain very robust over the exit voltage range for the entrance voltage interval from -400 mV to -600 mV. The shape of this pump map is very different from the conventional pump map driven by a sinusoidal signal (see Figure 5.1a). We show the pump map of pulse B.1 again in Figure (5.9) along with its derivative. The dynamics of the pumped current changes in an interesting way. We can get a better idea of how the pump map changes by plotting a surface projection of the pump map (see Figure 5.10) to help us emphasise the first, second, and third plateaus and to better track the dynamics of the pumped current. Additionally, we plotted the number of plateaus versus the exit gate voltage for different entrance voltages to emphasise the clustering of the pumped current at plateaus 1, 2 and 3 in Figure (5.12).

We can keep track of the pump dynamics by partitioning the pump map into different regions. These regions correspond to the range of entrance gate voltages in which plateaus 1, 2, and 3 or a combination of them are either present or are all absent. Essentially, there are four regions, denoted by the coloured rectangles brown, yellow, green, and pink corresponding to regions 1, 2, 3, and 4 respectively in Figure (5.10). Figure (5.11) is a companion to Figure (5.10), and it makes it easier to visualize the different regions. The first region, in brown, is where the pumped current is zero for the entrance voltage interval from -800 mV to -650 mV across the span of the exit gate voltage. This happens because the large DC voltage on the entrance gate prevents the RF signal of pulse B.1 from lowering the entry barrier into the source reservoir to capture the electron(s). This behaviour is the same for conventional pumps.

The pump enters the second region (in yellow) in the entrance voltage interval from -650 mV to -600 mV, where plateaus 1, 2, and 3 begin to appear in the exit voltage interval from -2000 mV to -900 mV. This happens because the DC voltage

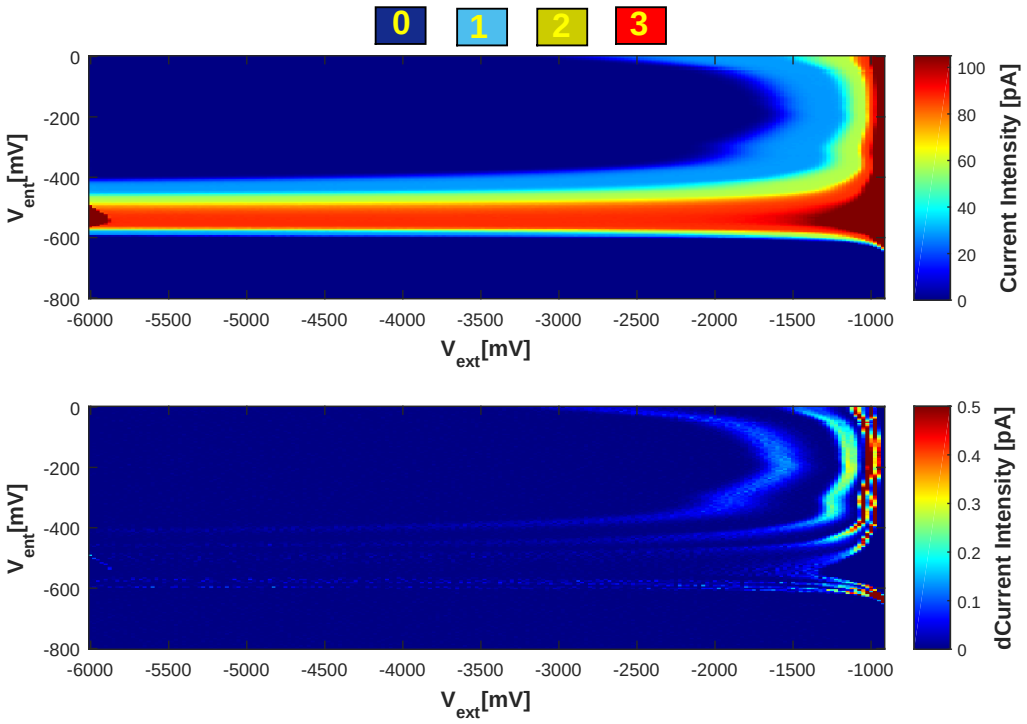

Figure 5.9: **The top figure is a replot of Figure (5.8b). The first, second and third plateaus have numerical values of 28.8 pA, 57.6 pA and 86.4 pA on the colour bar, respectively. The bottom plot is its numerical derivative. The plateaus 0, 1, 2 and 3 are approximately 0 pA on the colour bar**

on the entrance gate is small enough to allow the RF signal to pull the barrier below the Fermi level and form a dot. The capture line in Figure (3.7) of Section (3.1.5) is the line where the transition from no pumping to pumping occurs as the entrance voltage decreases. In the conventional pump map, the capture line appears shared by all plateaus. However, in this AWG pump map, the transition is further quantised. If we take a cross-section in the entrance voltage (see Figure 5.13), we see that the current increases from 0, 1, 2 and 3 ef in the specified exit voltage interval. This effect might be a result of the coupling between the entrance and exit barrier. Usually, we expect the size of the dot to depend mainly on the exit gate voltage. However, because of the longer time spent in the capture portion of the pump cycle, the size of the dot at the point it decouples from the reservoir may be dependent on the entrance voltage as well due to the irregularity in the rise speed of the AWG waveform. If the dot has not decoupled by the time it reaches the irregularity, the dot will decouple very quickly. We would expect to see the same behaviour for the conventional pump, but the relative influence of

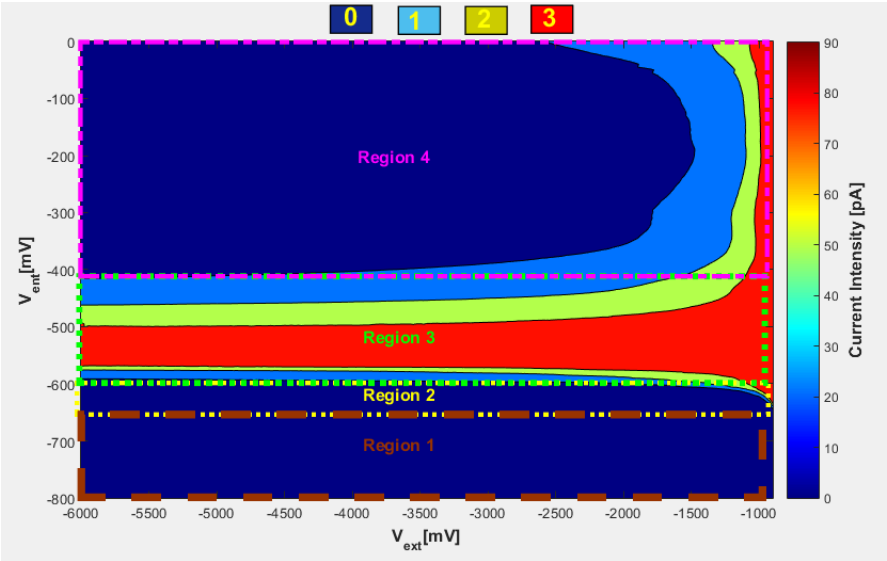

Figure 5.10: **Illustrates the contour pump map of Figure (5.8b). The first, second and third plateaus have numerical values of 28.8 pA, 57.6 pA and 86.4 pA on the colour bar, respectively. This contour map emphasizes plateaus 1, 2 and 3 in light blue, green and red, respectively. It also shows the different regions used to track the pump dynamics**

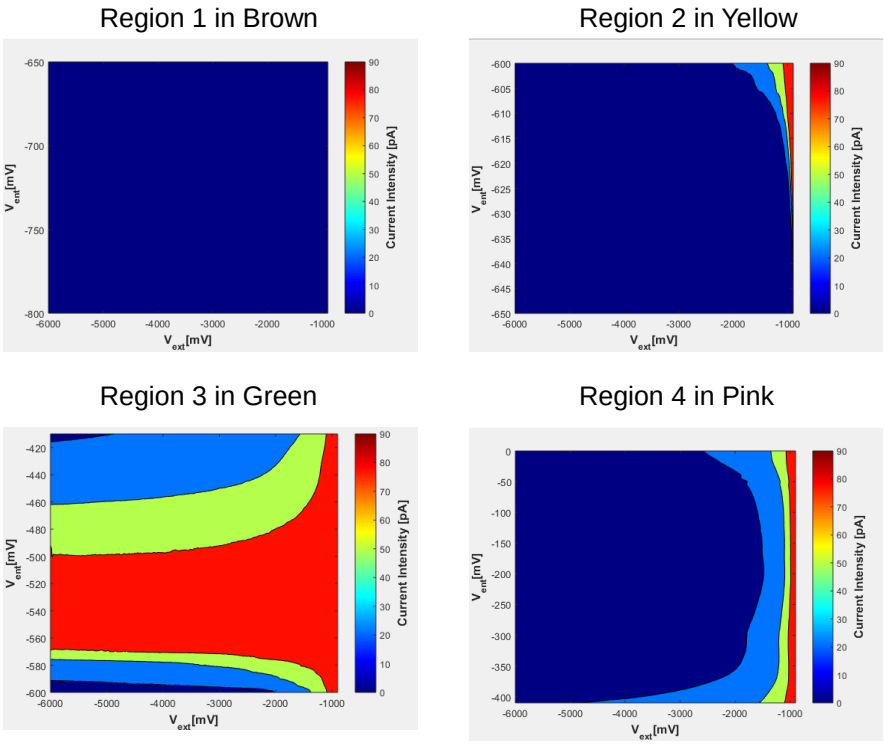

Figure 5.11: **Illustrates the four regions of Figure (5.10) plotted separately**

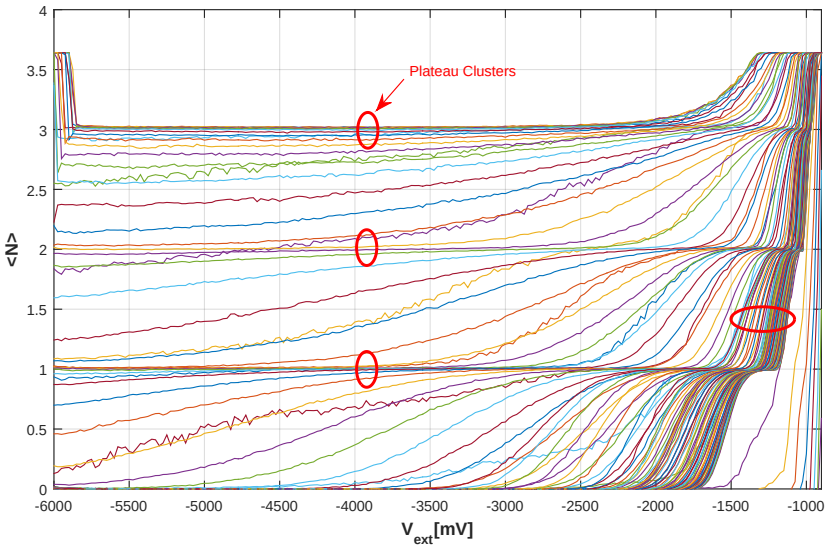

Figure 5.12: **Illustrates the number of average electrons of Figure (5.8b) versus exit gate voltage. The clustering of the first, second and third plateaus is apparent in this plot. These clusters form for some ranges of the entrance voltage. The clusters are seen in the pump map where the colour remains the same for a plateau. Notice the robustness of the 1, 2 and 3 plateau over a large range of the exit voltage. The different regions can also be given in the exit voltage as: region 1 (no pumping), region 2 (-1500 to -1000) mV, region 3 (-6000 to -2500) mV, and region 4 (-2500 to -900) mV**

the entrance and exit voltages on the dot size may make it harder to observe.

We then transition to the more interesting third region (in green), in the entrance voltage interval from -600 mV to -410 mV, where the first, second and third plateaus remain robust over the exit voltage. We call this region 'the long plateau region'. In this region, we notice that the pumping happens peculiarly as the entrance voltage decreases. Starting at an entrance voltage just above -600 mV in Figure (5.10), we pump the first plateau (light blue), followed by the second plateau (light green) as the entrance voltage decreases, we then pump the third plateau (red), we return to pumping the second plateau, and lastly, we pump the first plateau again (see Figure 5.14). In this region, the entrance voltage is low enough to withstand the influence of large exit voltages. Thus, the entrance barrier can couple to the source reservoir. The dot forms as the barrier rise from the reservoir, capturing the electron(s). Upon ejection, one electron is ejected

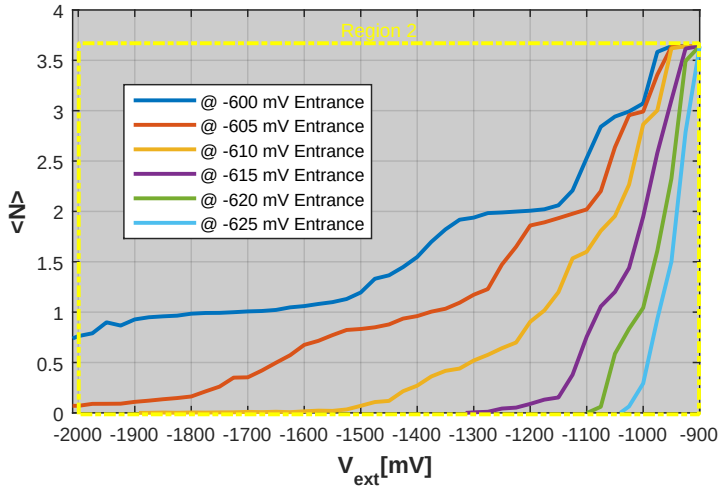

Figure 5.13: **The cross-section through region 2 at the selected entrance voltages,showing the current increasing from 0, 1, 2, and 3 ef, in the exit voltage interval from -2000 mV to -900 mV**

just above -600 mV in entrance voltage. This is because the entrance voltage is still quite high, and we can only capture one electron. As the entrance voltage decreases further, the barrier is now low enough to capture two electrons and eject two. If we decrease the entrance voltage further, we can capture three electrons and eject three electrons. Any further increase in the entrance voltage makes it harder to eject the electrons over the barrier, similar to the conventional pump. Thus, we eject two electrons, then one and finally no electrons are ejected for exit voltages above -2500 mV.

Usually, we do not expect the ejection lines to occur at such negative entrance voltages. Compared to the conventional pump, this pump appears to have been squeezed down in the entrance voltage and stretched in the exit voltage in region 3. We do not have a complete understanding of how this occurs, but we suspect a few mechanisms that might contribute to it. We know that in this split-gate pump, the RF amplitude and the bias voltage affect both the height and length of the pumped current region. Experiment A in Section (5.1) showed that the pump map due to the signal generator differs from the pump map due to the AWG for a sinusoidal excitation because these instruments synthesise their waveform differently. The RF signal of the AWG might be coupling differently to the 2DEG compared to the conventional sinusoid. The higher-order hamonics of the AWG signal might help to excite the captured electrons over the exit barrier. We know

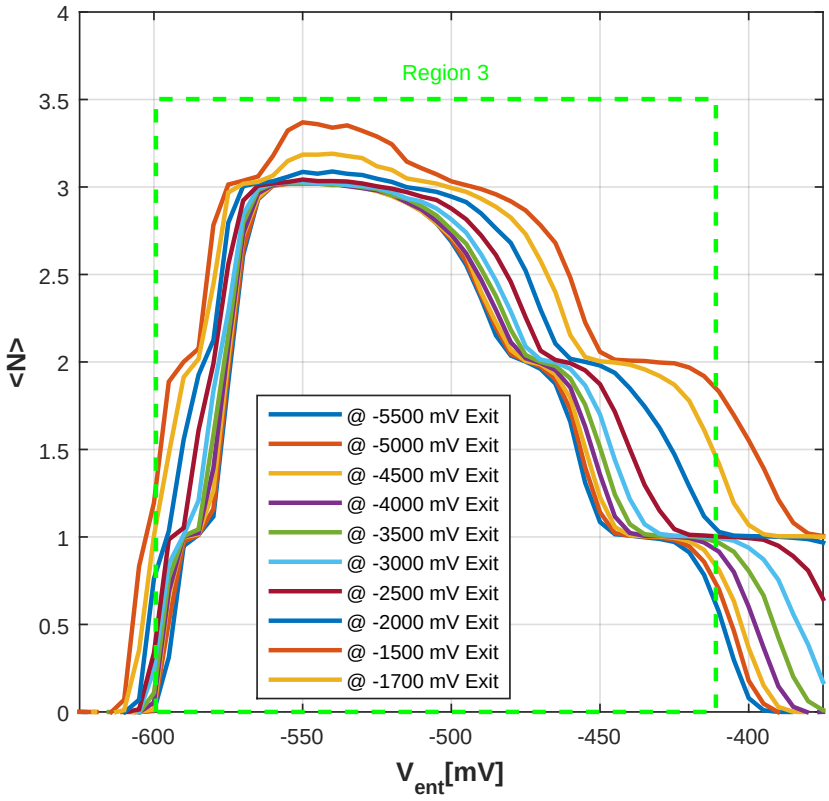

Figure 5.14: **Illustrates the peculiarity in the dynamics of the pumped current in region 3, where we pumped plateaus in the strange sequence 1, 2, 3, 2 1**

that measuring pumps in a magnetic field stretches the plateaus in the exit voltage. The AWG signal might be inducing local magnetic fields in the dot. Lastly, we enter the fourth region (pink) in the entrance voltage interval from -410 mV to 0 mV, where the plateaus are short and bundled over the exit voltage interval from -2500 mV to -900 mV (see Figure 5.12).

5.2.4 Analysis of the pumped current plateaus 1, 2 and 3

Figure (5.15) shows the plot of the pumped current for pulse B.1 (blue) in Figure (5.8a). From this plot, we estimated the accuracy and precision of the first, second and third plateaus by calculating the mean and standard deviation for a set of data points in a range of exit voltage and at selected values of entrance voltages. We focused on the robust plateaus in the entrance voltage interval from -400 mV to -600 mV and performed the analysis on plateaus 1, 2 and 3, corresponding to the

entrance voltages of -425 mV, -470 mV and -560 mV. These are the values of the flattest and longest plateaus along the exit voltage range in each plateau cluster. We selected them by visual inspection. We plotted the selected pumped current data, used descriptive statistics on the data, fitted the decay cascade model to the data, and plotted the error graph for each plateau.

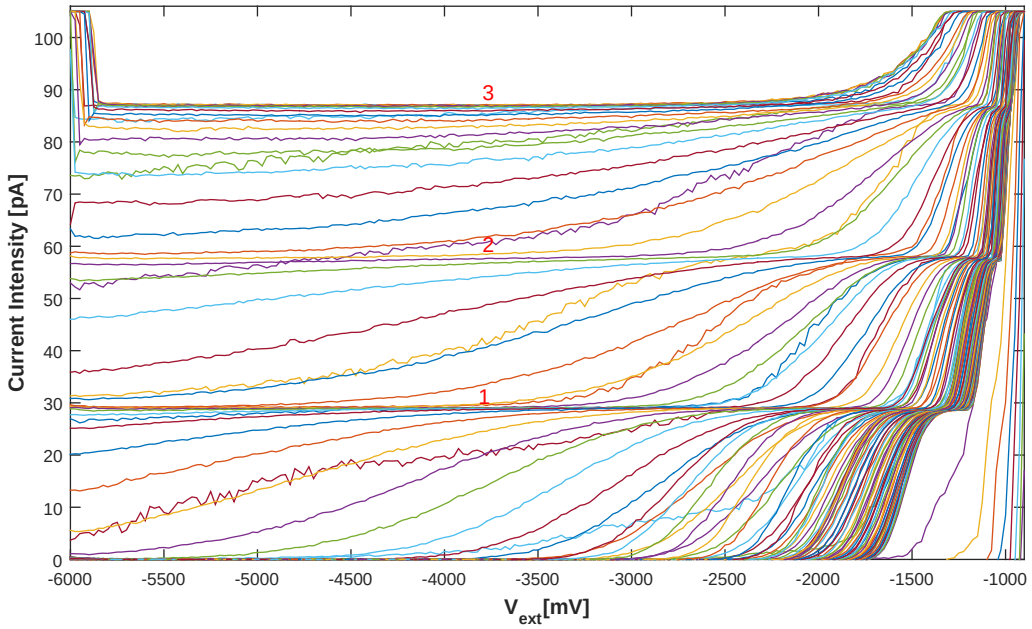

Figure 5.15: **Illustrates the pumped current of Figure (5.8b) versus the exit voltage. The first, second and third plateaus have numerical values of 28.8 pA, 57.6 pA and 86.4 pA, respectively**

We present the analysis of the first plateau in Figure (5.16). The red rectangle in Figure (5.16a) indicates the robustness of the first plateau in the interval from -6000 mV to -2450 mV of the exit voltage, at an entrance voltage of -425 mV. We fitted a normal distribution to the data points bounded by the rectangle (see Figure 5.16e) and calculated the mean and the standard deviation presented in Figure (5.16b). The data points are in red circles, the mean current is in brown, the standard deviation is the vertical line in yellow and the reference ef value from the Codata is plotted in green dashed line. The mean value is 28.6550 pA with a standard deviation of 0.5125 pA, and the reference ef value is 28.8392 pA. We fitted the decay cascade model of Section (3.1.6) to the selected data in Figure (5.16c). Lastly, in Figure (5.16d), we plotted the fractional deviation of

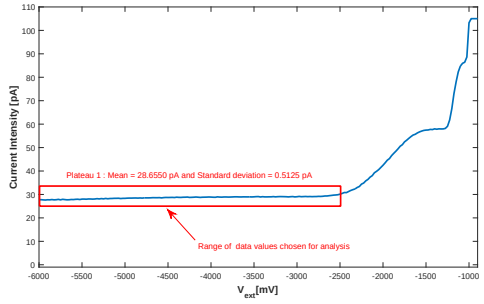

(a) Pumped current Ip versus the exit voltage for an entrance voltage of -425 mV for plateau 1

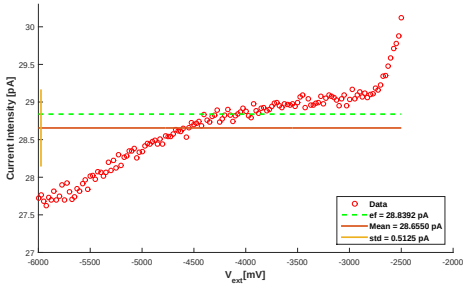

(b) The mean and standard deviation of the pumped current at a selected data interval from -6000 mV to -2500 mV in exit voltage

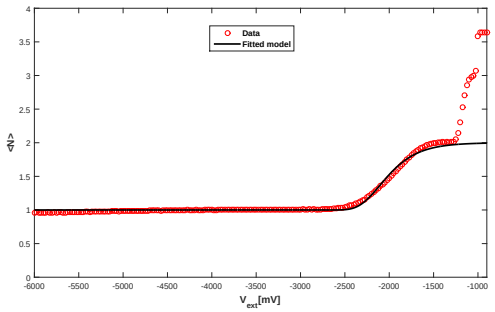

(c) The cascade decay model fitted to the pumped current data of plateau 1

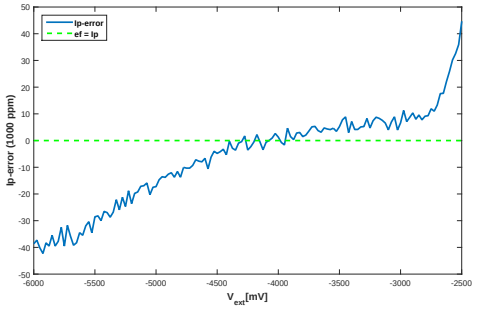

(d) Show the distance each data point is from the ideal ef value. This distance is the error.

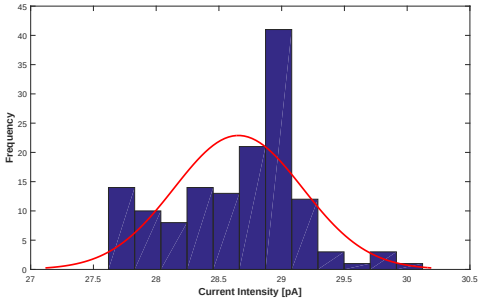

(e) The histogram for the selected data of plateau 1

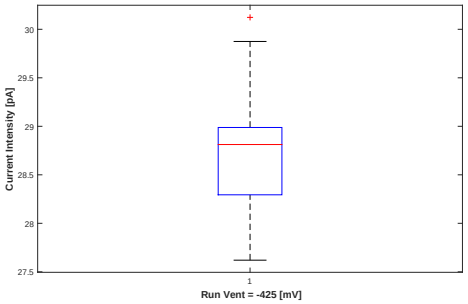

(f) The boxplot for the selected data of plateau 1

Figure 5.16: **Shows the analysis of plateau 1 to determine its mean and standard deviation. We also show the data fitted with the decay cascade model, the error graph, a histogram and a box plot of the data. We selected the data in the exit voltage interval from -6000 mV to -2500 mV**

the pumped current relative to the ef on a 1000 ppm scale.

We followed the same procedure above to analyse the second and third plateaus. Figure (5.17) presents the analysis of the second plateau. We selected the data points in the exit voltage interval from -6000 mV to -2625 mV, at an entrance voltage of -470 mV. This plateau has a mean current of 57.3167 pA and a standard deviation of 0.5974 pA. Likewise, Figure (5.18) presents the analysis of the third plateau for an exit voltage interval from -6000 mV to -2000 mV, at -560 mV entrance voltage. Its mean current is 86.9449 pA with a standard deviation of 0.1555 pA. We summarised these results in Table (5.1). From this table, we notice that plateau 1 is the most accurate, with a difference between the Codata and the mean of 0.1842 pA. Then plateau 2, with a difference of 0.3617 pA. Lastly plateau 3, with a difference of 0.4274 pA. However, the standard deviation of the third plateau is the smallest with a value of 0.1555 pA, followed by the first plateau with a value of 0.5125 pA, and ending with the second plateau with a value of 0.5974 pA. Table (5.1) also provides the relative error and error interval of each plateau. The third plateau has the lowest relative error of 4 940 ppm and error range of 8 000 ppm, while the second has a relative error of 6 271 ppm and error range of 40 000 ppm, and lastly, the first plateau has a relative error of 6 387 ppm and error range of 80 000 ppm. It is clear from these results that plateau 3 is the flattest and most accurate. Plateau 1 is the second flattest and least accurate. While plateau 2 is the least flat, but second most accurate. The relative accuracy obtained for plateaus 1, 2 and 3 are at least 4 orders of magnitude larger than that obtained in literature such as [25] and [81]. The reason for this discrepancy is due to the range of data chosen for analysis. In this thesis, we have chosen the following exit voltage ranges of 3.5 V, 3.3 V and 3.925 V to analyse plateaus 1, 2, and 3 respectively due to their length. Thus, this has resulted in a much larger relative error compared to [25] and [81]. A smaller voltage range for the plateaus would reduce this error significantly.

Another method to analyse the plateaus is to use the UDC model as shown in Figure (5.16c), (5.17c) and (5.18c). An attempt to use the UDC model show that the UDC model is not a suitable model for the long plateaus effects we are observing. An attempt to use the UDC model show that the UDC model is not a suitable model for the long plateaus effects we are observing. For example, if we consider the first plateau on Figure (5.16c), we immediately notice that the

model does not fit the first plateau well, and it was observed that if the first plateaus was fitted well, one could not fit the second plateau at all. Furthermore, the delta value for the first plateau is $\delta_1 = 5368$ and the alpha values are $\alpha_1 \neq \alpha_2$ and $\alpha_1 > \alpha_2$ This result does not correspond to the conventional pumped current result observed in literature. Thus, the UDC model does not apply for the long plateau regime.

Table 5.1: **Shows the mean, standard deviation, relative error and error interval of the first, second, and third plateaus**

Plateau	Mean [pA]	ef [pA]	Std. Dev [pA]	Error [e^3 ppm]	ΔError [e^3 ppm]
1	28.6550	28.8392	0.5125	6.38714	-40 to 40
2	57.3167	57.6784	0.5974	6.270978	- 20 to 20
3	86.9449	86.5175	0.1555	4.94004	2 to 10

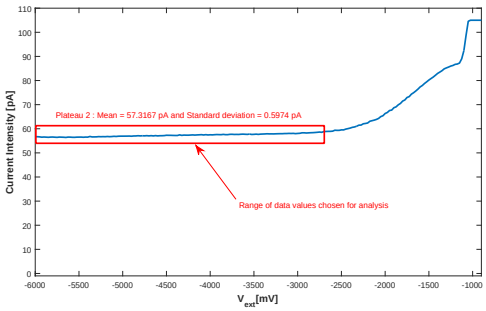

(a) Pumped current Ip versus the exit voltage for an entrance voltage of -470 mV for plateau 2

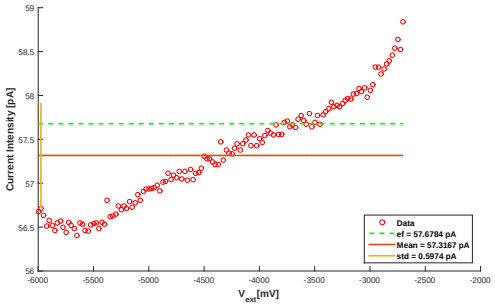

(b) The mean and standard deviation of the pumped current at a selected data interval from -6000 mV to -2700 mV in exit voltage

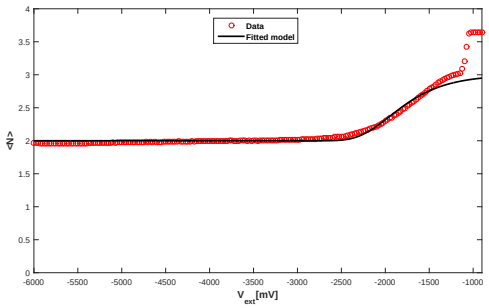

(c) The cascade decay model fitted to the pumped current data of plateau 2

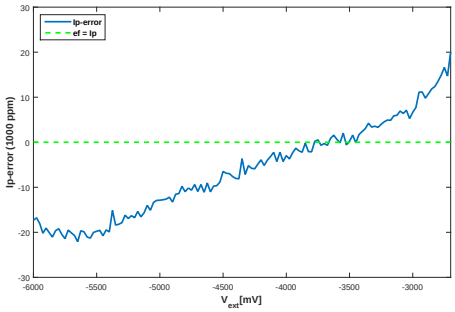

(d) Show the distance each data point is from the ideal ef value. This distance is the error

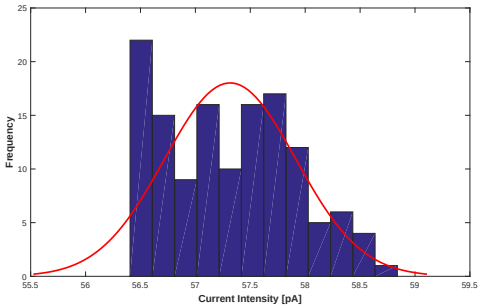

(e) The histogram for the selected data of plateau 2

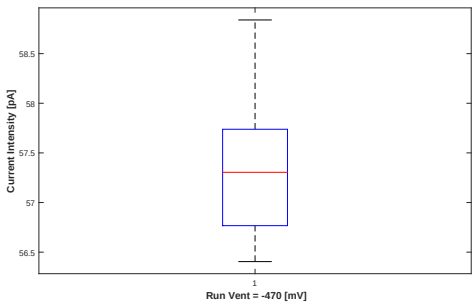

(f) The boxplot for the selected data of plateau 2

Figure 5.17: **Shows the analysis of plateau 2 to determine its mean and standard deviation. We also show the data fitted with the decay cascade model, the error graph, a histogram and a box plot of the data. We selected the data in the exit voltage interval from -6000 mV to -2700 mV**

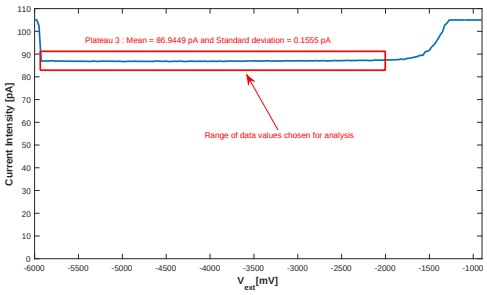

(a) Pumped current Ip versus the exit voltage for an entrance voltage of -560 mV for plateau 3

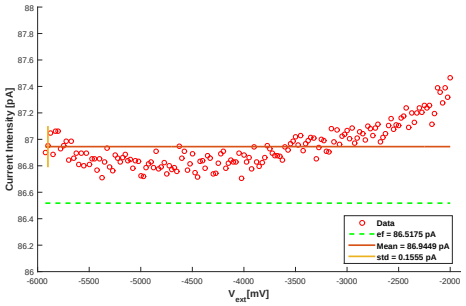

(b) The mean and standard deviation of the pumped current at a selected data interval from -5925 mV to -2000 mV in exit voltage

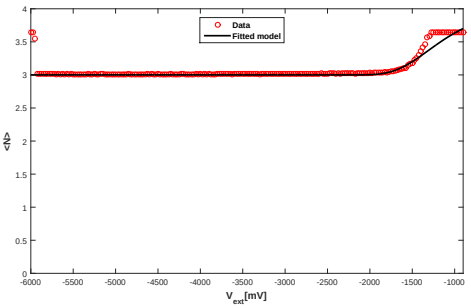

(c) The cascade decay model fitted to the pumped current data of plateau 3

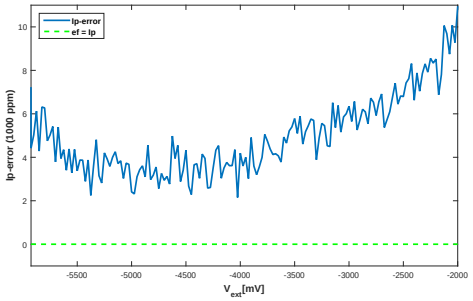

(d) Show the distance each data point is from the ideal ef value. This distance is the error

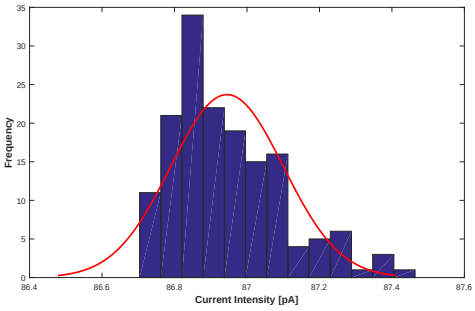

(e) The histogram for the selected data of plateau 3

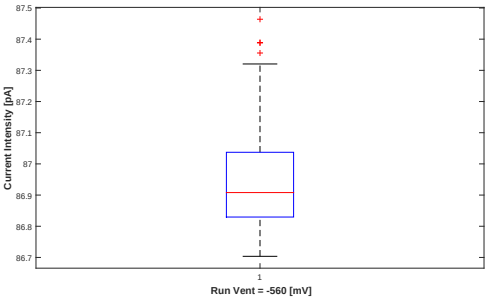

(f) The boxplot for the selected data of plateau 3

Figure 5.18: **Shows the analysis of plateau 3 to determine its mean and standard deviation. We also show the data fitted with the decay cascade model, the error graph, a histogram and a box plot of the data. We selected the data in the exit voltage interval from -5925 mV to -2000 mV**

5.3 Experiment C: Tuning the 3rd Plateau of Pulse B.1 with Source-Drain Bias

Howe et al. [1] observed that the source-drain bias had the effect of 'aiding' the electrons over the split-gate potential barrier. He showed that the first plateau elongates along the exit voltage with increasing source-drain bias. In this experiment, we used the source-drain bias to tune the third plateau of the pump map in Figure (5.8b). Our experiment differs slightly from that in [1], because we kept the entrance gate voltage constant at -530 mV. We chose this value to ensure we are on the third plateau. In Figure (5.19), we present the pump maps showing the migration of the third plateau at different source-drain bias intervals. We stepped the source-drain bias from -100 mV to 200 mV in increments of 1mV. In Figure (5.19a), the source-drain bias was stepped from 151 mV to 200 mV, in Figure (5.19b), the source-drain bias was stepped from 0 mV to 150 mV, and finally, in Figure (5.19c), the source-drain bias was stepped from -100 mV to 0 mV. We swept the exit gate voltage from -9000 to -600 mV in all three cases.

The pump maps of Figure (5.19) clearly shows the effect on the third plateau due to the source-drain bias. We call this effect 'tuning'. Nevertheless, it is difficult to discern how the third plateau is affected directly from these pump maps. To get a better picture of the tuning effect, it is useful to plot the average number of electrons versus the exit gate voltage (see Figure 5.21). From this figure, it is clear that the third plateau migrates from plateau zero and progressively makes its way up to the eighth plateau as the source-drain bias increases from -100 mV to 200 mV in increments of 1mV. Notice how all these plateaus are still elongated. This means that the third plateau remains robust in the exit gate voltage as we tune it with the source-drain bias. However, below the first plateau, we do notice that the third plateau begins to lose its robustness in the exit gate voltage. The migration from the first to the eighth plateau happens smoothly because of the 1 mV source-drain bias increments. Thus, we can tune to any long plateau between one and eight by selecting the appropriate source-drain bias, even if the plateau is not in the quantised regime. Moreover, the formation of the ninth plateau is also visible, indicating that with a further increase in the source-drain bias, we can tune the third plateau past the eighth plateau to the ninth, tenth, etc. Another important feature we see in Figure (5.21) is the clustering of the plateaus around their quantised value. This effect can be explained with a potential land-

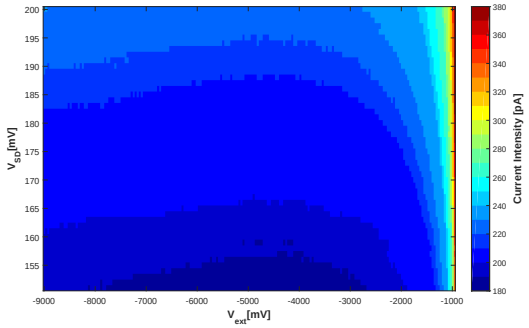

(a) Illustrates the tuning of the third plateau in the source-drain bias interval from 151 mV to 200 mV

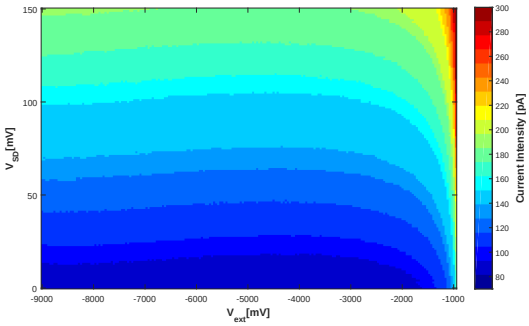

(b) Illustrates the tuning of the third plateau in the source-drain bias interval from 0 mV to 150 mV

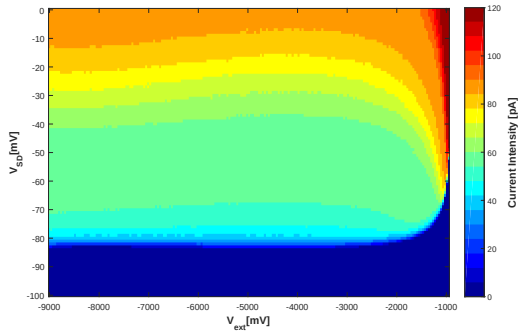

(c) Illustrates the tuning of the third plateau in the source-drain bias interval from -100 mV to 0 mV

Figure 5.19: **Shows the tuning of the third plateau in the source-drain bias interval from -100 mV to 200 mV**

scape model provided by Hume et al [1] and [82]. Firstly, the reason we enter into the long plateau regime over the exit voltage or split-gate is explained by the potential model provided for the finger-split gate configuration in Figure (3.23) by [1]. Additionally, Hume et al. [82] provides an Electrostatic potential model

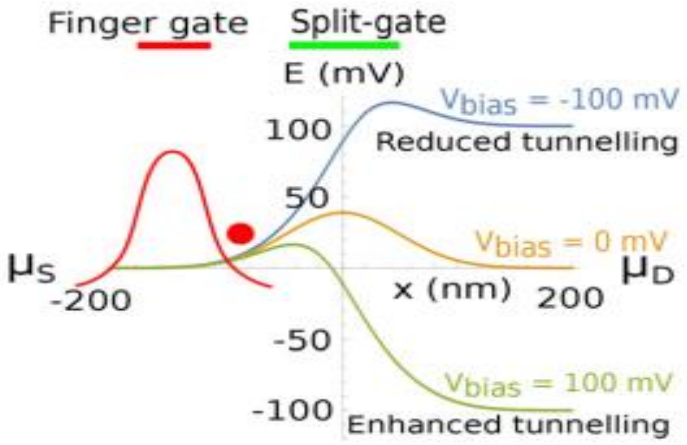

Figure 5.20: **Electrostatic potential model of the source-drain bias effect on split-gate potential (adapted from [82])**

of the source-drain bias effect on the split-gate potential which is shown in Figure (5.20). It shows the variation of the potential energy of the spilt-gate with the source-drain bias voltages for – 100 mV (blue), 0 mV (yellow) and 100 mV (green). As the electrostatic potential of the drain is lowered, the effective barrier height lowers in response, and the size of the dot gets bigger, making it easier to accommodate more electrons of the dot. Thus, we can pump electrons where otherwise the dot would be too small to pump, and it also allows pumping over a larger range of exit gate voltages.

Figure (5.22) is the plot of the average number of electrons versus the source-drain bias interval from 0 mV to 150 mV, at an exit voltage of -5000 mV. It shows that the clusters correspond to the robustness of the plateaus along the source-drain bias. Notice also that the adjacent plateaus are spaced at quantised values of the source-drain bias, which is approximately 40 mV. Figure (5.22) is very similar to Figures (3.8b [17] and 3.9c [51]), and since one can calculate the energy of the dot in the latter figures in turnstile operation, we will investigate the implication of the former figure for the enegy of the dot in a split-finger gate pump operation.

In Figure (5.23), we plot the derivative of Figure (5.22) of the average number of electrons versus the source-drain bias interval of 0 mV to 150 mV, at an exit

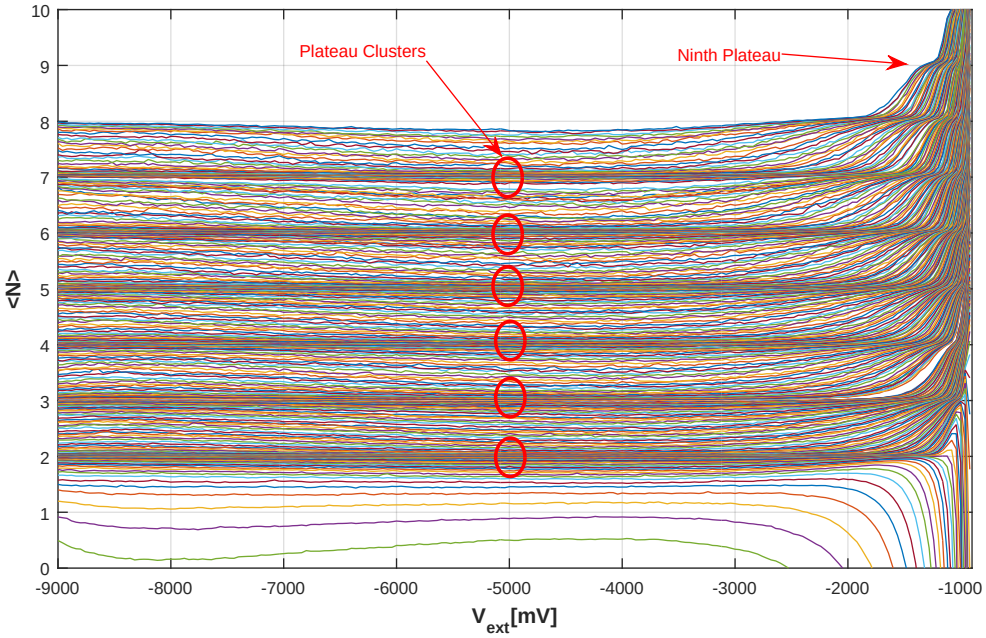

Figure 5.21: **Shows the source-drain bias tuning of the elongated third plateaus selected at an entrance voltage of -530 mV in Figure (5.8b). The tuning is done from -100 mV to 200 mV in source-drain bias, in increments of 1 mV. The third plateau migrates from the first to the eighth as we change the source-drain bias voltage. Notice that all the plateaus are elongated and robust in exit voltage**

voltage of -5000 mV. The corresponding plateaus 3, 4, 5 and 6 are clearly indicated by the red texted arrow. Notice that all adjacent plateaus are still spaced at a quantised value of the source-drain bias, which is approximately mV.One can also as estimate the range of source-drain bias voltage for which the above mentioned plateaus are robust, in this case the plateaus are robust over a source-drain bias voltage of approximately 6 mV.

In Figure (5.24), we plotted select plateaus corresponding to the source-drain bias indicated on each plateau. We selected the flattest plateaus from their clusters by visual inspection. Figure (5.25) shows the pumped current of each source-drain bias. We indicated the mean and standard deviation on each plateau. We calculated these quantities for the data points in the interval from -9000 mV to -2000 mV in exit voltage. In Table (5.2), we summarised these results and sorted them in order of highest precision to the lowest. From it, we can see that plateau 2 is the

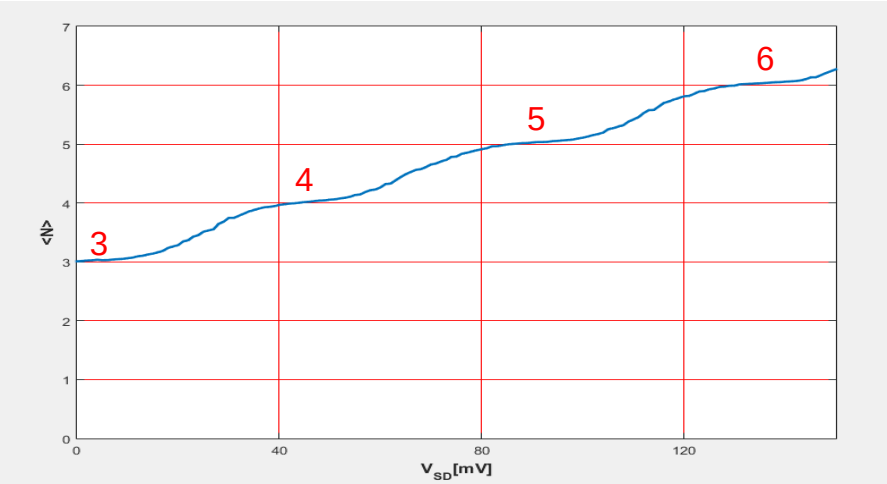

Figure 5.22: **The plot of the average number of electrons versus the source-drain bias interval from 0 mV to 150 mV, at an exit voltage of -5000 mV. It shows that the clusters correspond to the robustness of the plateaus along the source-drain bias. Notice also that the adjacent plateaus are spaced at quantised values of the source-drain bias, which is approximately 40 mV**

flattest, followed by plateaus 3, 4, 7, 5, 6, 8, and finally 1. In particular, plateau 2 has a precision of 0.1443 pA and a difference between the Codata and the mean values of 0.0378 pA. It is an incredibly flat and accurate plateau compared to the other plateaus. We also observe that plateau 1 has the worst precision of 2.2762 pA and a difference between the Codata and the mean values of 3.1996 pA. These calculations were all done on a very large range of the data set, if we took a smaller range of the data set, we would have improve the accuracy and standard deviation of each plateau.

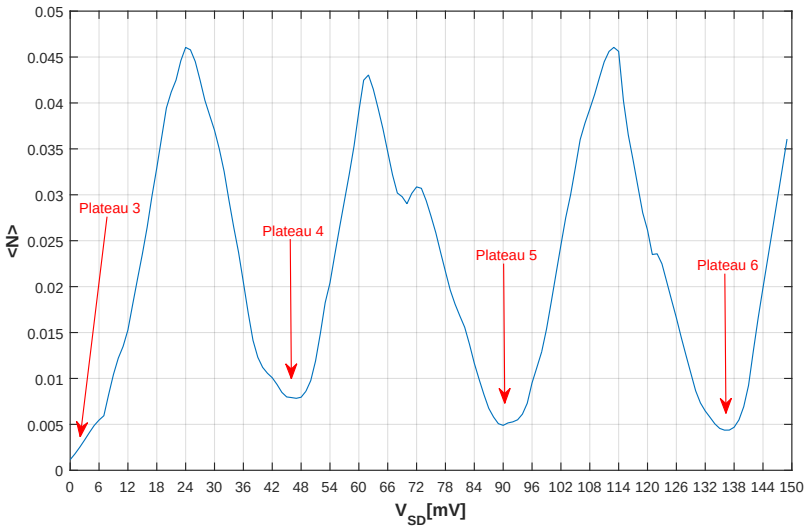

Figure 5.23: **The plot of the derivative of the average number of electrons versus the source-drain bias interval from 0 mV to 150 mV, at an exit voltage of -5000 mV. It shows that the clusters correspond to the robustness of the plateaus along the source-drain bias. Notice also that the adjacent plateaus are spaced at quantised values of the source-drain bias, which is approximately 40 mV. Notice also that the plateaus are robust for an approximate source-drain bias voltage range of 6 mV**

Table 5.2: **Shows the eight plateaus arranged in order of the highest precision based on the standard deviation. The data points were selected in the interval from -9000 mV to -2000 mV**

Plateau number	Std. Dev [pA]	Mean [pA]	ef [pA]
2	0.1443	57.7162	57.6784
3	0.3818	87.1897	86.5176
4	0.8344	114.2975	115.3568
7	0.9177	201.5818	201.8744
5	1.0363	142.5469	144.196
6	1.1714	171.4458	173.0352
8	1.7442	228.0652	230.7136
1	2.2762	32.0388	28.8392

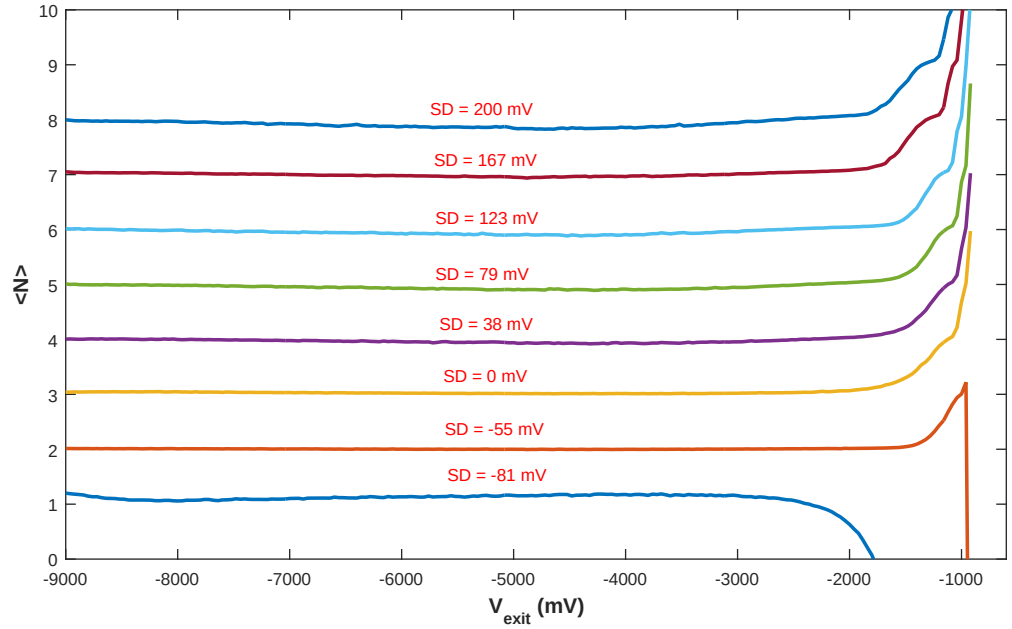

Figure 5.24: **Illustrates the third plateau tuned from one to eight, at selected source-drain bias, as depicted**

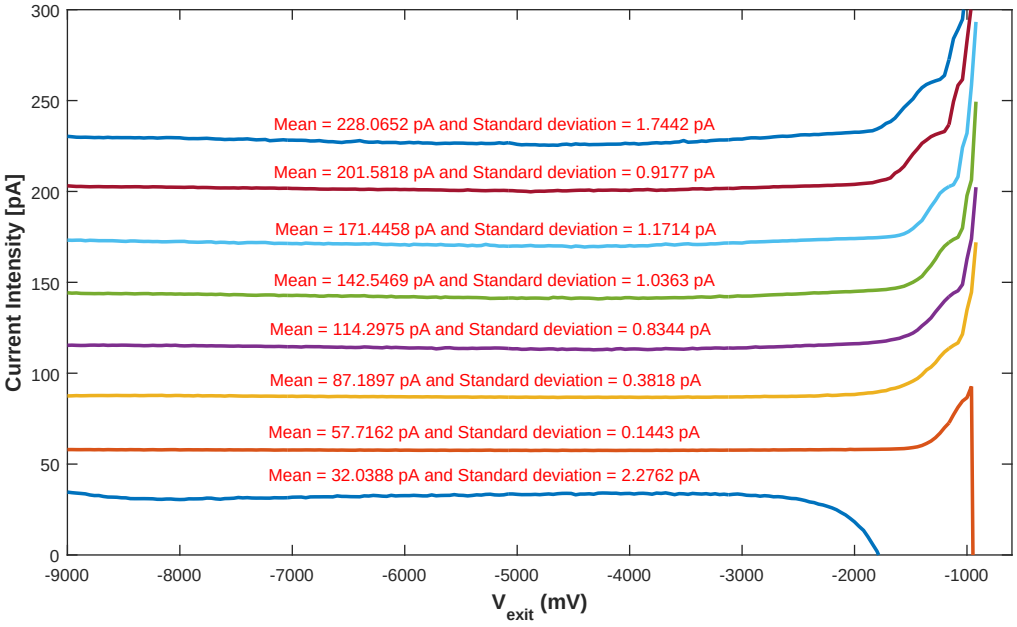

Figure 5.25: **Illustrates the mean and Std. Dev for the selected plateaus of Figure (5.24), as depicted**

Chapter 6

Discussion

We conducted three experiments in Chapter (5). In Section (5.1), we discussed the affect of an AWG sinusoid on the quantised current compared to the conventional quantised current of a signal generator sinusoid. In Section (5.2), we discussed the affect a trapezoidal waveform with different rising edge slopes has on the quantised current. The rising edge slopes were sinusoidal segments of different frequencies. Lastly, in Section (5.3), we tuned the quantised current with a source-drain bias voltage. In Section (6.1) of this chapter, we summarise the major outcomes of the three experiments. We put our results in the context of existing studies and discuss the relationship between them in Section (6.2). Furthermore, we highlight the limitations of our studies and their implication for future research in Section (6.3) and (6.4), respectively. We conclude by stating the overall significance of our studies in Section (6.5).

6.1 Summary of Major Results

6.1.1 Experiment A: the effect of the AWG sinusoid on the conventional pumped current

This experiment compared the pump maps of a signal generator to an arbitrary waveform generator sinusoid. We observed three main differences: firstly, the AWG pump map was more robust in entrance voltage compared to the signal generator. The first plateau of the AWG spanned an entrance voltage interval from -30 mV to -790 mV, while the signal generator only spanned an interval from -100 mV to -700 mV, as depicted in Figure (5.4). Secondly, the AWG produced a pump map that contains a very high degree of ripples on the onset lines compared

to the smoother onset lines of the signal generator, as depicted in Figure (5.6). Lastly, both RF sources produced long plateaus, 500 mV in exit voltage length.

6.1.2 Experiment B: the effect of a trapezoidal waveform on the conventional pump map

In this experiment, we observed the pump behaviour in response to AWG pulses of different rising edge slopes. We found that plateaus 1, 2 and 3 were elongated (robust) over the entire exit voltage range for the entrance voltage interval from -600 mV to -400 mV. For this interval, we also saw that the pump map improved with the steeper sinusoidal segment slope on the rising edge of the pulse, as depicted in Figure (5.8). Furthermore, the dynamics of the pumped current of Figure (5.8a) was very peculiar, the plateaus moved between the short and long plateau regimes. This behaviour was due to the trapezoidal waveform, but the actual mechanism by which it came about requires additional investigation.

6.1.3 Experiment C: tuning the 3rd plateau of pulse B.1 with source-drain bias

In this experiment, we selected a robust third plateau at an entrance voltage of -530 mV in Figure (5.8) and successfully tuned it with the source-drain bias voltage. The third plateau migrated from the first to the eighth plateau as we swept the source-drain bias from – 100 mV to 200 mV in increments of 1 mV. The plateaus were very robust in exit voltage for the source-drain voltages above -70 mV. Below -70 mV, we began to lose robustness (look at plateau number one). This result allows us to tune onto any long plateau between one and eight by selecting the desired source-drain bias voltage, even if the plateau is not an integer multiple of ef.

6.2 Relationship of Results to Existing Studies

The high degree of ripples on the onset line of the AWG pump map, in Section (5.1), has not been observed in the literature. The long plateau pumping regime was first observed by Howe et al. [1]. The difference between our study and Howe's et al. [1] is the mechanism by which these plateaus manifest themselves. Howe showed that by changing the source-drain bias voltage, he could elongate the first plateau. Howe et al. [1] used a signal generator to modulate the entrance gate. By

contrast, we entered the long plateau regime using an AWG source. We were able to elongate as many as eight plateaus along the exit gate voltage. Howe's et al. [1] idea of enhancing the first plateau with the source-drain bias stimulated the idea of tuning the plateaus with source-drain bias, as we did in Section (5.3). Furthermore, Wright et al. [54] observed that the quantised current is robust along the exit voltage when an applied magnetic field is perpendicular to the sample. Our experiement showed that the same effect is present in the absence of externally applied magnetic fields. This suggests that the RF source from the AWG might be inducing a local magnetic field at the sample.

In Section (5.2), we showed that a faster slope on the rising edge of the pulse restored the quantised current in the entrance voltage interval from -400 mV to -600 mV. This experiment is very similar to Giblin's et al. [25] experiment. However, he restored the quantised current with a slower slope on the rising edge of the pulse. This is a seeming contradiction. However, there are key differences between the two experiments, stated in Section (5.2) which could resolve this ambiguity.

6.3 Limitations of the Study

In our research, we did not consider external magnetic field effects, and we used a single sample to conduct the studies. The AWG can output a maximum voltage of 1 Vp-p. Thus, we were limited from doing a comparative power study between the AWG and the Signal generator for the pump maps. Furthermore, we observed all these results on a split-finger gate pump geometry. These results seem to be unique to split-finger gate pump geometry because the LPR has not yet been observed in the finger-finger gate pump geometry in the literature.

6.4 Implications for Future Research

6.4.1 Increased frequency and magnetic field pumping

From the redefinition of the Ampere, we can increase the magnitude of the pumped current either by increasing the operating frequency or the number of pumped electrons. However, for the conventional single-gate modulated pump, if the frequency

is too high, then we face the issue of having insufficient back tunnelling time. Some electrons may not tunnel back to the source. Such a fast waveform contributes to the pump error during the capture phase of the pump cycle. Giblin et al. [25] showed that as long as the capture segment of the waveform is sufficiently slow, then for some entrance voltage interval, we could increase the frequency of the waveform without introducing error to the pumped current. We aim to pump at frequencies greater than 181.81 MHz in future experiments. Furthermore, following Wright's et al. [54] observation, we will conduct experiments in high magnetic fields (up to 10 Tesla) and compare the outcomes to this study.

6.4.2 The frequency-dependence permittivity of GaAs/AlGaAs substrate

An electromagnetic field inside a dielectric material will polarise its atoms. The permittivity or relative permittivity of the material measures the strength of the polarisation. The permittivity depends on various parameters of the field, such as its frequency and amplitude. The electric field passing through the material may be delayed, absorbed, dispersed, etc. Since we have a multiple frequency waveform (the trapezoid), we must investigate how these frequencies go through the dielectric. It might tell us something about how each frequency couples to the 2DEG, thus, help understand how the pulse affects pumping.

6.4.3 Modelling the split-finger gate geometry using an EM simulator

We modelled the finger-finger gate and finger-split gate potential profiles in Mathematica. This model does not take into account the many physical aspects of the gates. We will model these gate geometries with an electromagnetic solver to enhance our understanding of their potential profiles and their relations to the pumped current when we apply arbitrary waveforms to these gates.

6.5 The overall significance of the study

Many of the single-electron pumps we find in the literature focuses on using a sinusoidal waveform to pump. These pumps have shown great promise towards the realisation of the Ampere. The introduction of an external magnetic field elongated the plateaus along the exit voltage and greatly improved the accuracy

of the quantised current. This work brought us closer to the realisation of the Ampere. Giblin et al. [25] built upon this work by using a trapezoidal waveform containing a combination of a sinusoidal segment and a rectangular pulse to modulate the pump. This technique allowed him to increase the magnitude of the pumped current by increasing the operating frequency of the pump. We used the same trapezoidal pulse technique on a split-finger gate pump. We found that the trapezoidal pulse has a significant affect on the behaviour of the split-finger gate pump. In particular, we observed effects such as plateau elongation, pumping up to eight plateaus, the creation of ripples on the onset line, strange pumped current dynamics and highly robust plateaus. These effects are yet to be properly understood and will, when properly understood, have a significant implication on the way we understand single-electron pumps. It might give us a new perspective on single-electron pumps concerning the source-drain bias, split-finger gate pumps, and different modulation waveforms. Moreover, it might bring us closer to the realisation of the Ampere.

Appendix A

The Time and Frequency Domain Analysis of the Waveforms of Experiment B

Figure (1) shows the 3D pump map of pulse B.1 of Figure (5.8a), while Figures (2 and 3) shows the time and frequency domain analysis of pulse B.1 to B.5 of Figure (5.8a).

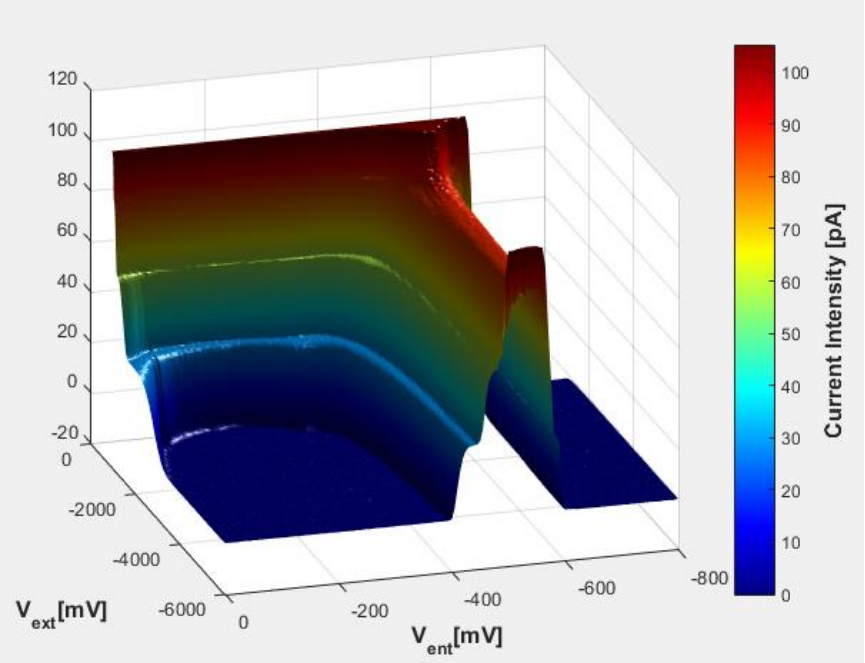

Figure 1: **Illustrates: the 3D pump map of pulse B.1 (blue) of Figure (5.8b) with 62.5 MHz sinusoidal segment. The first, second and third plateaus have numerical values of 28.8 pA, 57.6 pA and 86.4 pA on the color bar respectively.**

(a) Pulse B.1

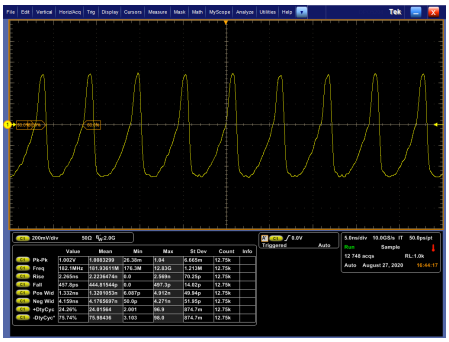

(b) Pulse B.2

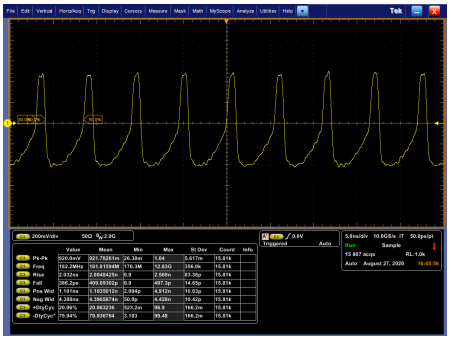

(c) Pulse B.3

(d) Pulse B.4

(e) Pulse B.5

Figure 2: **Illustrates time domain waveforms of the pulse B.1 to B.5 of Figure (5.8a)**

The Effects of rising time or Pulse Width on the pump map of Pulse B.1

The single-gate modulated pump is capture operated. In other words, the entrance gate of the pump gets modulated with an RF signal superimposed on a DC signal. The operation of this pump is explained in Section (3.1.5). We know that during the capture phase, there has to be a relaxation time to allow the electrons to back tunnel to the source and that the capturing should not happen too quickly for one to capture an electron reliably in the first place. This experiment investigated the

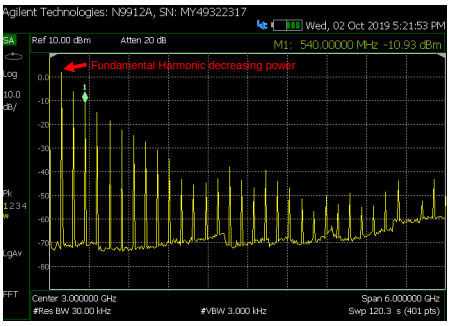

(a) FFT spectrum of Pulse B.1 fundamental harmonic power at 2.044 dBm.

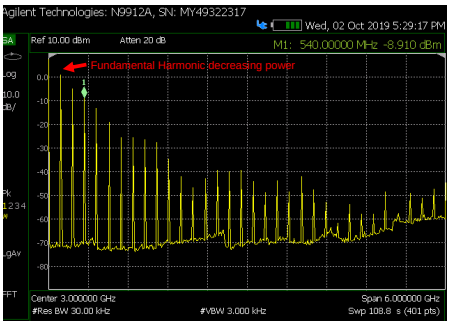

(b) FFT spectrum of Pulse B.2 fundamental harmonic power at 0.7754 dBm.

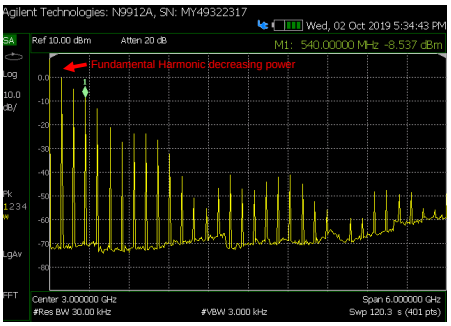

(c) FFT spectrum of Pulse B.3 fundamental harmonic power at -0.1381 dBm.

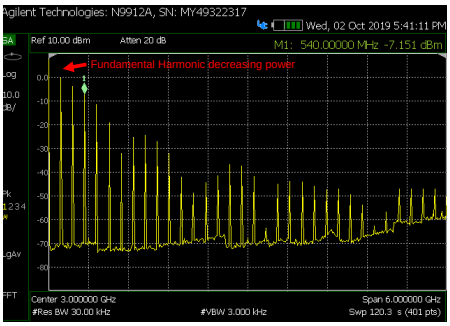

(d) FFT spectrumof Pulse B.4 fundamental harmonic power at -0.4698 dBm.

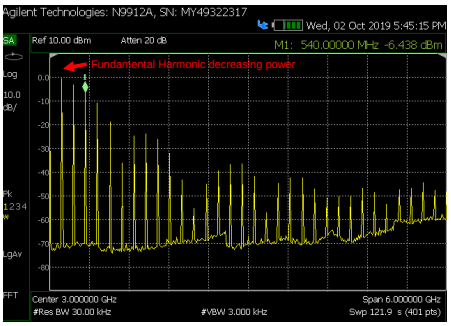

(e) FFT spectrum of Pulse B.5 fundamental harmonic power at -0.8083 dBm.

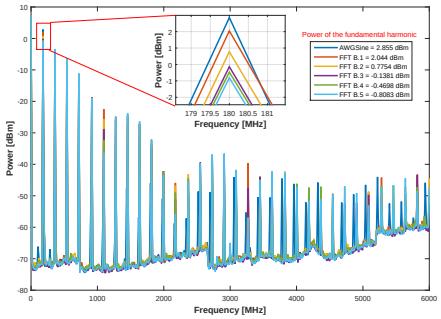

(f) Matlab FFT spectrum comparing the power of AWG Sinusoid to Experiment B.

Figure 3: **Illustrates Fast Fourier spectrum of the pulse B.1 to B.5 of Figure (5.8a). (f) shows the fundamental harmonic decreasing in power from pulse B.1 of Figure (5.8a), the highest power, to pulse B.5 of Figure (5.8a) the lowest power.**

effect that a change in the capture time had on the pump map of Figure (5.8b). The rise time of the pulse or equivalently the pulse width was changed in this experiment to change the capture time. The modified waveform is illustrated in Figure (4a), notice that the pulse is B.1 of Figure (5.8a). In other words, the

capture slope, the sinusoidal segment of the pulse was kept constant, while the width or rise time of the capture was varied, resulting in the waveforms of Figure (4a). There are eight waveforms, each corresponding to different rise times. The fall time and the duty cycle of the waveforms were kept constant.

Our results show that as the rise time decreases from right to left in Figure (4a), we observe in Figure (4a to 4e), that the pump map migrates downwards in the direction of more negative voltages on the entrance gate. The elongated plateaus, 1, 2, and 3 starting at around -400 mV entrance voltage in Figure (4b), have moved down and are now starting at -600 mV in the entrance voltage in Figure (4e). These long plateaus have also progressively deteriorated with smaller rise time or pulse width. Additionally, we see that above -400 mV, the pumping of the shorter plateaus begins to break for lower exit voltage values, Figure (4b to 4e). Decreasing the rise time further results in Figure (4f and 4g), where the third and second plateaus begin to disappear in Figure (4f), and they are eventually almost completely gone in Figure (4g). At the same time, the first plateau begins to migrate and expand, spanning an entrance voltage from -300 mV to -800 mV. Below -300 mV the plateaus are very small. Suddenly, in Figure (4h) the first plateau disappears too! And all the pump happens at very low entrance voltage over the range of exit voltage. The plateau pump happens over 0 to -100 mV of the entrance voltage, above this value, all the plateaus are very small, in a very tiny range of the exit voltage. In Figure (4i), for the shortest rise time, all the pumping essentially stops. Only a speck of pumping is seen on the pump map at the low entrance and exit gate voltages.

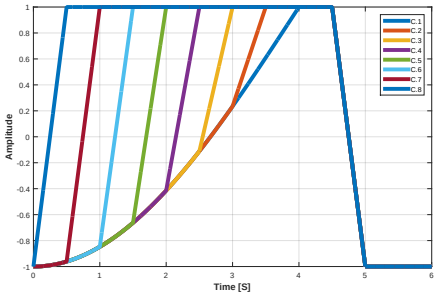

(a) Trapezoidal Pulse waveform: C1 to C5 with sinusoidal segment of the same frequency of 62.5 MHz.

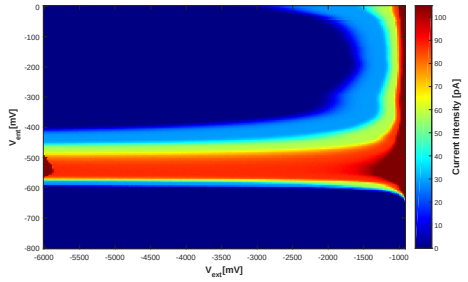

(b) Pump map of pulse C.1 (blue) with pulse width of 0.5 ns.

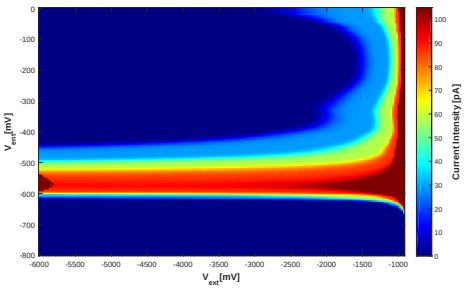

(c) Pump map of pulse C.2 (orange) with pulse width of 1 ns.

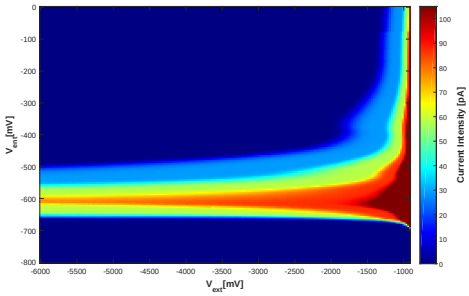

(d) Pump map of pulse C.3 (yellow) with pulse width of 1.5 ns.

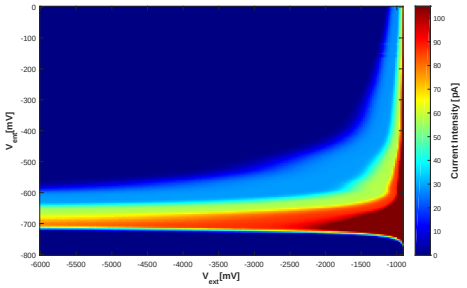

(e) Pump map of pulse C.4 (purple) with pulse width of 2 ns.

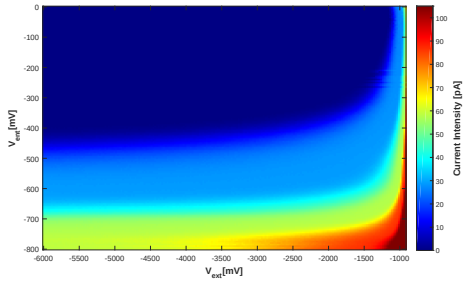

(f) Pump map of pulse C.5 (green) with pulse width of 2.5 ns.

Figure 4: **Shows the trapezoidal pulse waveform with various pulse width in increments of 0.5 ns. The sinusoidal segment has the same frequency. The width increases from C.1 to C.2 in (a) and their corresponding pump maps are shown in (b) to (i) respectively. The pulses were operated at a frequency of 181.81 MHz at 1 Vp-p amplitude. The first, second and third plateaus have numerical values of 28.8 pA, 57.6 pA and 86.4 pA on the color bar respectively**

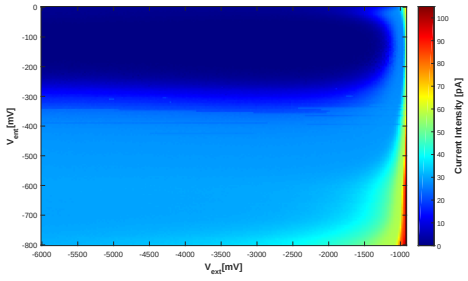

(g) Pump map of pulse C.6 (light blue) with pulse width of 3 ns.

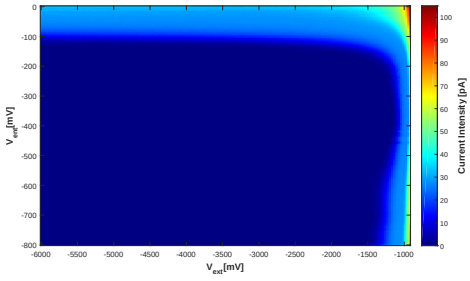

(h) Pump map of pulse C.7 (dark red) with pulse width of 3.5 ns.

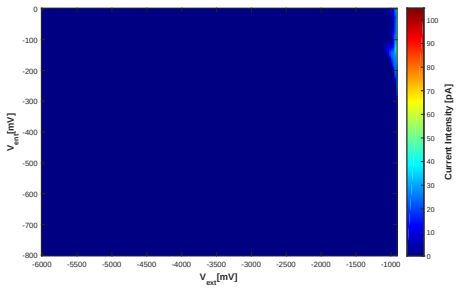

(i) Pump map of pulse C.8 (blue) with pulse width of 4 ns.

Figure 4: **Shows the Trapezoidal Pulse waveform with various pulse width in increments of 0.5 ns. The sinusoidal segment has the same frequency. The width increases from C.1 to C.2 in (a) and their corresponding pump maps are shown in (b) to (i) respectively. The pulses were operated at a frequency of 181.81 MHz at 1 Vp-p amplitude. The first, second and third plateaus have numerical values of 28.8 pA, 57.6 pA and 86.4 pA on the color bar respectively**

Pumping with Triangular and Square waveforms

Figure (5) shows additional experiments done with triangular to square pulses. In future, we will investigate these experiments further.

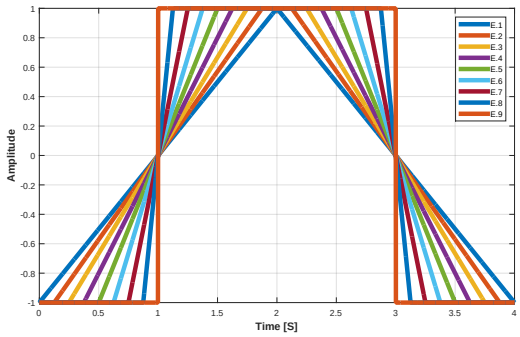

(a) Transforming the waveform from triangular E1 to square E9

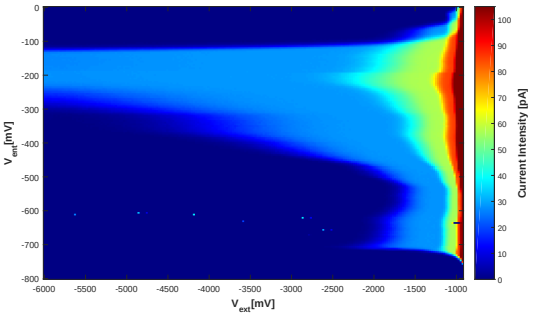

(b) Pump map of pulse E.1

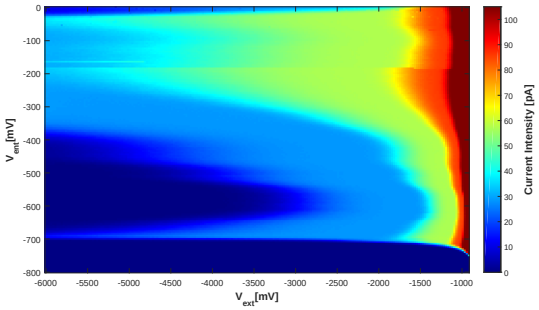

(c) Pump map of pulse E.2

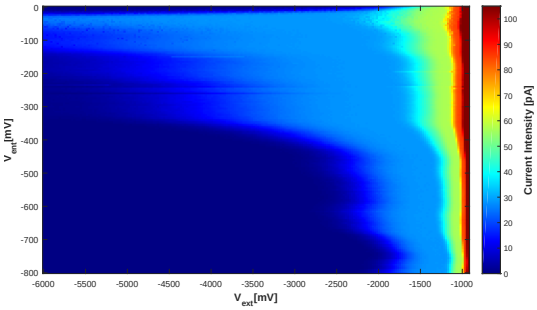

(d) Pump map of pulse E.3

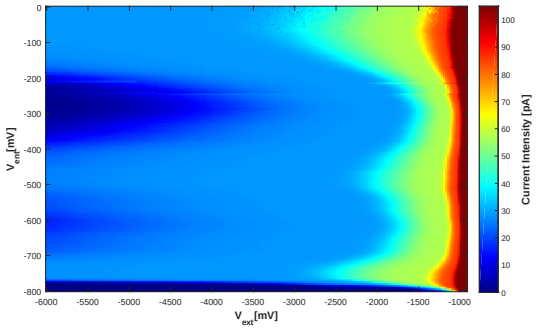

(e) Pump map of pulse E.4

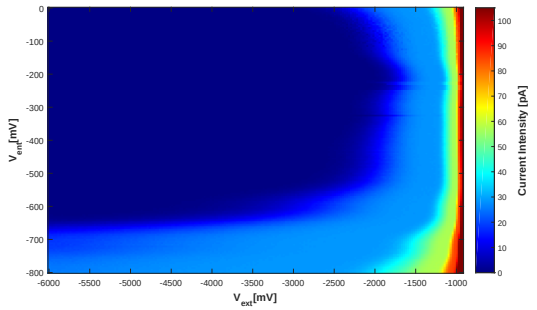

(f) Pump map of pulse E.5

Figure 5: **Illustrates (a) the waveform pulses from triangular E1 to square E2, and their corresponding pump maps (b) to (j)**

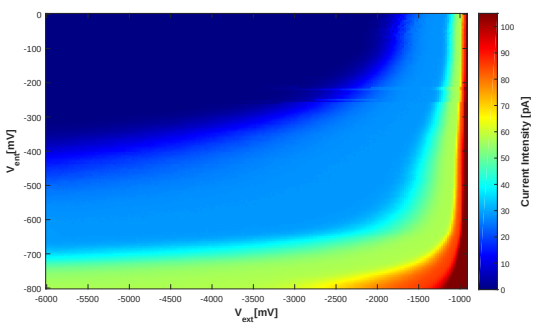

(g) Pump map of pulse E.6

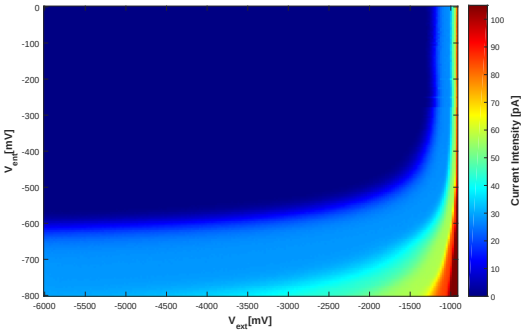

(h) Pump map of pulse E.7

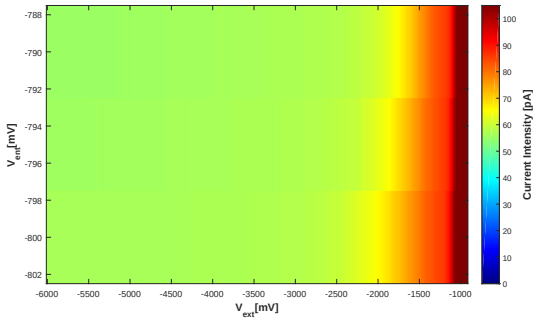

(i) Pump map of pulse E.8

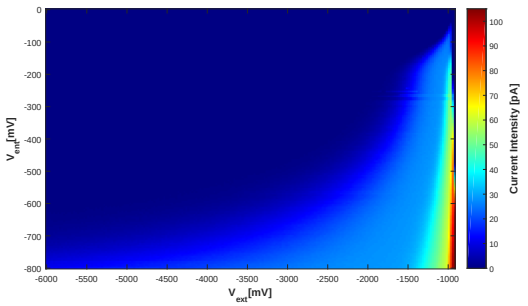

(j) Pump map of pulse E.9

Figure 5: **Illustrates (a) the waveform pulses from triangular E1 to square E2, and their corresponding pump maps (b) to (j)**

Ultrastable low-noise current amplifier (ULCA)

Although the ultrastable low-noise current amplifier (ULCA) was not used in this thesis, it is nevertheless an extremely important instrument that merits an introduction in this thesis. This state-of-the-art instrument is used nowadays by metrology institutes worldwide. The ULCA is a non-cryogenic electrical instrument based on specially designed resistor networks and operational amplifiers. It has two stages, the first provides a 1000-fold current gain, and the second performs a current-to-voltage conversion via an internal reference resistor of 1 MΩ or one can use an external standard resistor. The ULCA's transfer coefficient is highly stable versus temperature, time, and current amplitude within the full dynamic range of $\pm$5 nA. The averaging time is kept short at small input currents due to the low noise level of 2.4 fA.Hz$^{-\frac{1}{2}}$. A cryogenic current comparator is used to calibrate both outputs trans resistance and the input current gain, which can be traced to the quantum Hall effect. Within a week after calibration, the uncertainty contribution from short-term fluctuations and drift of the trans resistance is about 0.1 parts per million (ppm) and the long-term drift is typically 5 ppm/yr. The ULCA also allows one to trace the generation of small currents or to calibrate high-ohmic resistors [83].

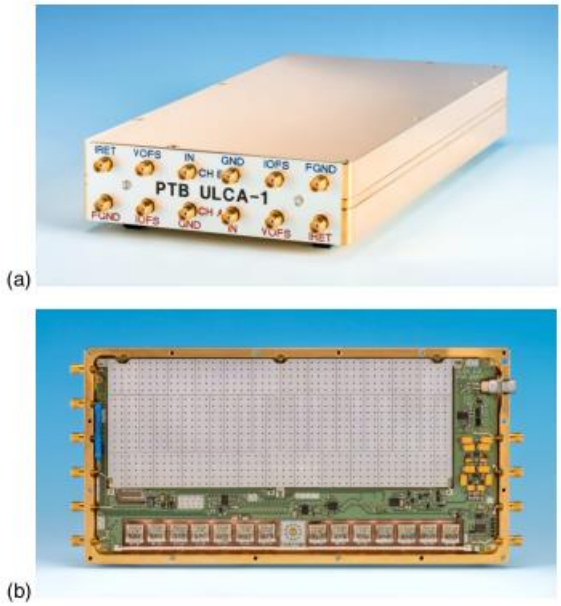

Figure 6: **Photographs of a ULCA prototype. (a) Complete two-channel unit and (b) Single ULCA channel without cover plate (adapted from [83])**

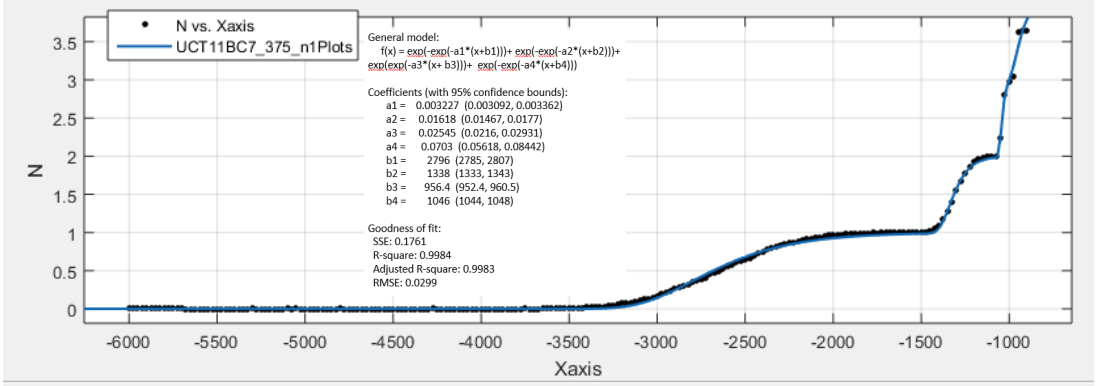

Figure 7: **The Universal Decay Cascade Model fitted to the normalised pumped current of Figure (5.12) at an entrance voltage of -375 mV. First we notice that the model fits the data quite well. The delta values for the first and second plateaus are:** $\delta_1 = 1458$ **and** $\delta_2 = 381.6$**. The alpha values represented by** a_j **indicates that** $a_1 \neq a_2 \neq a_3 \neq a_4$ **and** $a_1 < a_2 < a_3 < a_4$**, however, the assumption is that they should all be equal, but even with the short plateaus, the values of alphas which are expected to be equal differ. thus it is not clear which alpha value should be chosen.**

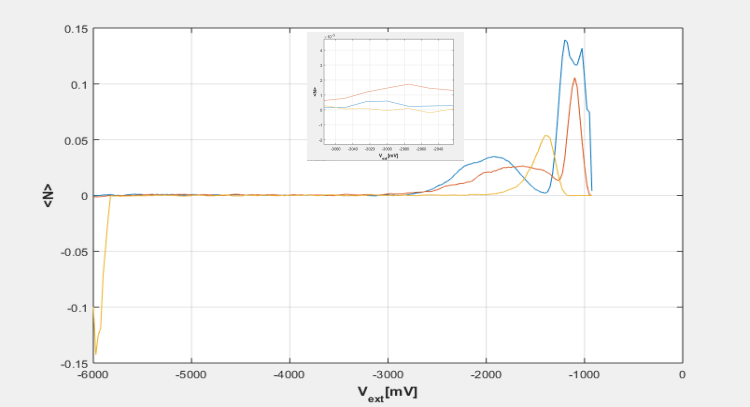

Figure 8: **The inflection point technique is another way to analyse the accuracy of the plateaus, however, probably due to the noise as shown on the plot, there is not clear inflection point for the long plateau data of this thesis and another method has to be applied.**

Bibliography

[1] H. Howe, M. Blumenthal, H. E. Beere, T. Mitchell, D. A. Ritchie, and M. Pepper, "Controllable plateaus in single-electron ' long pumping regime '," *Draft Unpublished*, pp. 1–10, 2020.

[2] L. P. Kouwenhoven, "Transport of Electron-Waves and Single-Charges in Semiconductor Nanostructures," Ph.D. dissertation, Delft University of Technology, 1992. [Online]. Available: http://resolver.tudelft.nl/uuid:44fc9935-8fe4-41e2-8c7a-4be9a31af5db

[3] BIPM, "The International System of Units (SI)," bipm.org. https://www.bipm.org/en/measurement-units/ (accessed Feb. 14, 2021).

[4] JCGM, "International vocabulary of metrology-Basic and general concepts and associated terms (VIM) 3rd edition 2008 version with minor corrections," International Bureau of Weights and Measures, Tech. Rep., 2012, Feb. 14, 2021. [Online]. Available: https://www.bipm.org/utils/common/documents/jcgm/JCGM{_}200{_}2012.pdf.

[5] CCEM, "Mise en pratique for the definition of the ampere and other electric units in the SI," International Bureau of Weights and Measures, Tech. Rep., 2019, May. 05, 2019. [Online]. Available: https://www.bipm.org/utils/en/pdf/si-mep/SI-App2-ampere.pdf.

[6] CIPM, "The International System of Units (SI)," International Bureau of Weights and Measures, Tech. Rep., 2006, May. 29, 2019. [Online]. Available: https://www.bipm.org/utils/common/pdf/si{_}brochure{_}8.pdf.

[7] J. P. Pekola, O.-P. Saira, V. F. Maisi, A. Kemppinen, M. Möttönen, Y. A. Pashkin, and D. V. Averin, "Single-electron current sources: Toward a refined definition of the ampere," *Reviews of Modern Physics*, vol. 85, no. 4, pp. 1421–1472, Oct 2013. [Online]. Available: https://link.aps.org/doi/10.1103/RevModPhys.85.1421

[8] TJBM. Janssen, SP. Giblin, P. See, JD . Fletcher, and M. Kataoka, "Redefinition of the Ampere," *Measurement and Control*, vol. 47, no. 10, pp. 315–322, Dec 2014. [Online]. Available: http://journals.sagepub.com/doi/10.1177/0020294014561724

[9] N. H. Kaneko, S. Nakamura, and Y. Okazaki, "A review of the quantum current standard," *Measurement Science and Technology*, vol. 27, no. 3, p. 032001, feb 2016. [Online]. Available: https://iopscience.iop.org/article/10.1088/0957-0233/27/3/032001

[10] CIPM, "The International System of Units (SI)," International Bureau of Weights and Measures, Tech. Rep., 2019, Feb. 14, 2020. [Online]. Available: https://www.bipm.org/utils/common/pdf/si-brochure/SI-Brochure-9-EN.pdf.

[11] J. L. Lee, "Kilogram: The Kibble Balance," nist.gov. https://www.nist.gov/si-redefinition/kilogram/kilogram-kibble-balance (accessed Mar. 07, 2021).

[12] D. V. Averin, A. B. Zorin, and K. K. Likharev, "Bloch oscillations in small Josephson junctions," *Zh. Eksp. Teor. Fiz*, vol. 88, no. August 1984, pp. 692–703, 1985. [Online]. Available: http://jetp.ac.ru/cgi-bin/dn/e{_}061{_}02{_}0407.pdf

[13] D. V. Averin and K. K. Likharev, "Coulomb blockade of single-electron tunneling, and coherent oscillations in small tunnel junctions," *Journal of Low Temperature Physics*, vol. 62, no. 3-4, pp. 345–373, 1986. [Online]. Available: https://doi.org/10.1007/BF00683469

[14] K. K. Likharev and A. B. Zorin, "Theory of the Bloch-wave oscillations in small Josephson junctions," *Journal of Low Temperature Physics*, vol. 59, no. 3-4, pp. 347–382, 1985. [Online]. Available: https://doi.org/10.1007/BF00683782

[15] L. J. Geerligs, V. F. Anderegg, P. A. M. Holweg, J. E. Mooij, H. Pothier, D. Esteve, C. Urbina, and M. H. Devoret, "Frequency-locked turnstile device for single electrons," *Physical Review Letters*, vol. 64, no. 22, pp. 2691–2694, 1990. [Online]. Available: https://link.aps.org/doi/10.1103/PhysRevLett.64.2691

[16] H. Pothier, P. Lafarge, C. Urbina, D. Esteve, and M. H. Devoret, "Single-Electron Pump Based on Charging Effects," *Europhysics Letters (EPL)*, vol. 17, no. 3, pp. 249–254, jan 1992. [Online]. Available: https://iopscience.iop.org/article/10.1209/0295-5075/17/3/011

[17] L. P. Kouwenhoven, A. T. Johnson, N. C. van der Vaart, C. J. P. M. Harmans and C. T. Foxon, "Quantized current in a quantum-dot turnstile using oscillating tunnel barriers," *Physical Review Letters*, vol. 67, no. 12, pp. 1626—-1629, 1991. [Online]. Available: https://link.aps.org/doi/10.1103/PhysRevLett.67.1626

[18] M. W. Keller, J. M. Martinis, N. M. Zimmerman, and A. H. Steinbach, "Accuracy of electron counting using a 7-junction electron pump," *Applied Physics Letters*, vol. 69, no. 12, pp. 1804–1806, sep 1996. [Online]. Available: http://aip.scitation.org/doi/10.1063/1.117492

[19] J. M. Shilton, V. I. Talyanskii, M. Pepper, D. A. Ritchie, J. E. F. Frost, C. J. B. Ford, C. G. Smith, and G. A. C. Jones, "High-frequency single-electron transport in a quasi-one-dimensional GaAs channel induced by surface acoustic waves," *Journal of Physics Condensed Matter*, vol. 8, no. 38, pp. 531–539, sep 1996. [Online]. Available: https://iopscience.iop.org/article/10.1088/0953-8984/8/38/001

[20] M. D. Blumenthal, B. Kaestner, L. Li, S. Giblin, T. J. B. M. Janssen, M. Pepper, D. Anderson, G. Jones, and D. A. Ritchie, "Gigahertz quantized charge pumping," *Nature Physics*, vol. 3, no. 5, pp. 343–347, 2007. [Online]. Available: https://doi.org/10.1038/nphys582

[21] B. Kaestner, V. Kashcheyevs, S. Amakawa, M. D. Blumenthal, L. Li, T. J. B. M. Janssen, G. Hein, K. Pierz, T. Weimann, U. Siegner, and H. W. Schumacher, "Single-parameter nonadiabatic quantized charge pumping," *PHYSICAL REVIEW B*, vol. 77, no. 15, p. 153301, 2008. [Online]. Available: https://link.aps.org/doi/10.1103/PhysRevB.77.153301

[22] J. P. Pekola, J. J. Vartiainen, M. Möttönen, O. P. Saira, M. Meschke, and D. V. Averin, "Hybrid single-electron transistor as a source of quantized electric current," *Nature Physics*, vol. 4, no. 2, pp. 120–124, 2008. [Online]. Available: https://doi.org/10.1038/nphys808

[23] V. F. Maisi, Y. A. Pashkin, S. Kafanov, J. S. Tsai, and J. P. Pekola, "Parallel pumping of electrons," *New Journal of Physics*, vol. 11, no. 11, p. 113057, 2009. [Online]. Available: https://doi.org/10.1088/1367-2630/11/11/113057

[24] V. Kashcheyevs and B. Kaestner, "Universal decay cascade model for dynamic quantum dot initialization," *Physical Review Letters*, vol. 104, no. 18, pp. 1–4, 2010.

[25] S. P. Giblin, M. Kataoka, J. D. Fletcher, P. See, T. J. B. M. Janssen, J. P. Griffiths, G. A. C. Jones, I. Farrer, and D. A. Ritchie, "Towards a quantum representation of the ampere using single electron pumps," *Nature Communications*, vol. 3, no. 1, pp. 1–6, 2012. [Online]. Available: https://doi.org/10.1038/ncomms1935

[26] K. Barnham and D. Vvedensky, *Low-Dimensional Semiconductor Structures: Fundamentals and Device Applications*. Cambridge University Press, 2010. [Online]. Available: https://doi.org/10.1017/CBO9780511624247

[27] L. P. Kouwenhoven, C. M. Marcus, P. L. McEuen, S. Tarucha, R. M. Westervelt, and N. S. Wingreen, "Electron Transport in Quantum Dots," in *Mesoscopic Electron Transport*, ser. NATO ASI Series (Series E: Applied Sciences), S. G. Sohn L.L., Kouwenhoven L.P., Ed. Springer, Dordrecht, 1997, vol. 345, pp. 105–214.

[28] C.Harmans, "Mesoscopic Physics an Intorduction," p. 230, 2003. [Online]. Available: https://ocw.tudelft.nl/courses/mesoscopic-physics/

[29] C. W. J. Beenakker and H. van Houten, "Quantum Transport in Semiconductor Nanostructures," in *Semiconductor Heterostructures and Nanostructures*, ser. Solid State Physics, H. E. Turnbull and David, Eds. Academic Press, Dec 1991, vol. 44, pp. 1–228. [Online]. Available: http://dx.doi.org/10.1016/S0081-1947(08)60091-0

[30] B. L. Sharma and R. K. Purohit, *Semiconductor Heterojunctions*, 1st ed., ser. International Series of Monographs in the Science of the Sol, B. Pamplin, Ed. Elsevier Science, 1974, vol. 5. [Online]. Available: https://doi.org/10.1016/b978-0-08-017747-2.50005-8

[31] J. H. Davies, *The Physics of Low-dimensional Semiconductors: An Introduction*. Cambridge University Press, 1997. [Online]. Available: https://doi.org/10.1017/CBO9780511819070

[32] A. Rogalski, "Recent progress in infrared detector technologies," *Infrared Physics and Technology*, vol. 54, no. 3, pp. 136–154, 2011. [Online]. Available: https://doi.org/10.1016/j.infrared.2010.12.003

[33] T. R. S. A. Sciences, "The Nobel Prize in Physics 1985," nobelprize.org. https://www.nobelprize.org/prizes/physics/1985/summary/ (accessed Feb. 02, 2020).

[34] T. R. S. A. of Sciences, "The Nobel Prize in Physics 1998," nobelprize.org. https://www.nobelprize.org/prizes/physics/1998/stormer/facts/ (accessed Feb. 02, 2020).

[35] T. J. Thornton, M. Pepper, H. Ahmed, D. Andrews, and G. J. Davies, "One-dimensional conduction in the 2D electron gas of a GaAs-AlGaAs heterojunction," *Physical Review Letters*, vol. 56, no. 11, pp. 1198–1201, 1986. [Online]. Available: https://doi.org/10.1103/PhysRevLett.56.1198

[36] H. Z. Zheng, H. P. Wei, D. C. Tsui, and G. Weimann, "Gate-controlled transport in narrow GaAs/AlxGa1-xAs heterostructures," *Physical Review B*, vol. 34, no. 8, pp. 5635–5638, 1986. [Online]. Available: https://doi.org/10.1103/PhysRevB.34.5635

[37] H. Van Houten, B. J. Van Wees, M. G. J. Heijman, and J. P. André, "Submicron conducting channels defined by shallow mesa etch in GaAs-AlGaAs heterojunctions," *Applied Physics Letters*, vol. 49, no. 26, pp. 1781–1783, 1986. [Online]. Available: https://doi.org/10.1063/1.97243

[38] C. J. B. Ford, T. J. Thornton, R. Newbury, M. Pepper, H. Ahmed, C. T. Foxon, J. J. Harris, and C. Roberts, "The Aharonov-Bohm effect in electrostatically defined heterojunction rings," *Journal of Physics C: Solid State Physics*, vol. 21, no. 10, pp. L325—-L331, apr 1988. [Online]. Available: https://doi.org/10.1088/0022-3719/21/10/005

[39] M. A. Kastner, "Artificial atoms," *Physics Today*, vol. 46, no. 1, pp. 24–31, 1993. [Online]. Available: https://doi.org/10.1063/1.881393

[40] M. N. A. Aadit, S. G. Kirtania, F. Afrin, M. K. Alam, and Q. D. M. Khosru, "High Electron Mobility Transistors: Performance Analysis, Research Trend and Applications," in *Different Types of Field-Effect Transistors - Theory and Applications*, M. M. P. Momčilo Pejović, Ed. IntechOpen, jun 2017, ch. 3, p. 192. [Online]. Available: http://dx.doi.org/10.5772/67796

[41] R. H. Harrell, K. S. Pyshkin, M. Y. Simmons, D. A. Ritchie, C. J. B. Ford, G. A. C. Jones, and M. Pepper, "Fabrication of high-quality one-and two-dimensional electron gases in undoped GaAs/AlGaAs heterostructures," *Applied Physics Letters*, vol. 74, no. 16, pp. 2328–2330, 1999. [Online]. Available: https://doi.org/10.1063/1.123840

[42] R. A. Millikan, "The Isolation of an Ion, a Precision Measurement of its Charge, and the Correction of Stokes's Law," *PHYSICAL REVIEW JOURNALS ARCHIVE*, vol. 32, no. 4, pp. 349—-397, 1911. [Online]. Available: https://link.aps.org/doi/10.1103/PhysRevSeriesI.32.349

[43] K. K. Likharev, "Single-Electron Devices and Their Applications," in *Proceedings of the IEEE*, vol. 87, no. 4. IEEE, 1999, pp. 606–632. [Online]. Available: https://ieeexplore.ieee.org/10.1109/5.752518

[44] D. C. Wasshuber, *Computational Single-Electronics*, 1st ed., ser. Computational Microelectronics. Springer-Verlag Wien, 2001. [Online]. Available: http://link.springer.com/10.1007/978-3-7091-6257-6

[45] I. O. Kulik and R. I. Shekhter, "Kinetic phenomena and charge discreteness effects in granular media," *Journal of Experimental and Theoretical Physics*, vol. 41, no. 2, pp. 308–316, 1975. [Online]. Available: http://jetp.ac.ru/cgi-bin/dn/e{_}041{_}02{_}0308.pdf

[46] B. Kaestner and V. Kashcheyevs, "Non-adiabatic quantized charge pumping with tunable-barrier quantum dots: A review of current progress," *Reports on Progress in Physics*, vol. 78, no. 10, 2015.

[47] H. Howe, "Amplitude, temperature, and frequency dependence of quantum pumps in semiconductor heterostructures," Ph.D. dissertation, University College London, 2015. [Online]. Available: https://discovery.ucl.ac.uk/id/eprint/1474205/

[48] N. M. Zimmerman and M. W. Keller, "Electrical metrology with single electrons," *Measurement Science and Technology*, vol. 14, no. 8, pp. 1237—-1242, 2003. [Online]. Available: https://doi.org/10.1088/0957-0233/14/8/307

[49] M. W. Keller, A. L. Eichenberger, J. M. Martinis, and N. M. Zimmerman, "A Capacitance Standard Based on Counting Electrons," *Science*, vol. 285, no. 5434, pp. 1706–1709, 1999. [Online]. Available: https://science.sciencemag.org/10.1126/science.285.5434.1706

[50] S. P. Giblin, S. J. Wright, J. D. Fletcher, M. Kataoka, M. Pepper, T. J. B. M. Janssen, D. A. Ritchie, C. A. Nicoll, D. Anderson, and G. A. C. Jones, "An accurate high-speed single-electron quantum dot pump," *New Journal of Physics*, vol. 12, no. 7, p. 073013, 2010. [Online]. Available: https://doi.org/10.1088/1367-2630/12/7/073013

[51] Y. Nagamune, H. Sakaki, L. P. Kouwenhoven, L. C. Mur, C. J. P. M. Harmans, J. Motohisa, and H. Noge, "Single electron transport and current quantization in a novel quantum dot structure," *Applied Physics Letters*, vol. 64, no. 18, pp. 2379–2381, 1994. [Online]. Available: https://aip.scitation.org/doi/abs/10.1063/1.111620

[52] N. Maire, F. Hohls, B. Kaestner, K. Pierz, H. W. Schumacher, and R. J. Haug, "Noise measurement of a quantized charge pump Noise measurement of a quantized charge pump," *Applied Physics Letters*, vol. 92, no. 8, p. 082112, 2008. [Online]. Available: https://doi.org/10.1063/1.2885076

[53] B. Kaestner, V. Kashcheyevs, G. Hein, K. Pierz, U. Siegner, and H. W. Schumacher, "Robust single-parameter quantized charge pumping," *Applied Physics Letters*, vol. 92, no. 19, p. 192106, 2008. [Online]. Available: https://doi.org/10.1063/1.2928231

[54] S. J. Wright, M. D. Blumenthal, G. Gumbs, A. L. Thorn, M. Pepper, T. J. B. M. Janssen, S. N. Holmes, D. Anderson, G. A. C. Jones, C. A. Nicoll, and D. A. Ritchie, "Enhanced current quantization in high-frequency electron pumps in a perpendicular magnetic field," *Physical Review B*, vol. 78, no. 23, p. 233311, 2008. [Online]. Available: https://link.aps.org/doi/10.1103/PhysRevB.78.233311

[55] S. J. Wright, M. D. Blumenthal, M. Pepper, D. Anderson, G. A. C. Jones, C. A. Nicoll, and D. A. Ritchie, "Parallel quantized charge pumping," *Physical Review B*, vol. 80, no. 11, p. 113303, 2009. [Online]. Available: https://link.aps.org/doi/10.1103/PhysRevB.80.113303

[56] B. Kaestner, C. Leicht, V. Kashcheyevs, K. Pierz, U. Siegner, and H. W. Schumacher, "Single-parameter quantized charge pumping in high magnetic fields," *Applied Physics Letters*, vol. 94, no. 1, p. 012106, 2009. [Online]. Available: https://doi.org/10.1063/1.3063128

[57] COLANDIS, "Definition and origin of cleanroom technology," colandis.com. https://www.colandis.com/en/requirements-cleanroom-technology (accessed Jan. 1, 2021).

[58] THOMAS, "Cleanroom Air Flow Principles," thomasnet.com. https://www.thomasnet.com/articles/automation-electronics/Cleanroom-Air-Flow-Principles/ (accessed Jan. 13, 2021).

[59] O. Usher, "Cleaning up in the cleanroom," ucl.ac.uk. https://blogs.ucl.ac.uk/science/tag/cleanroom/ (accessed Jan. 28, 2020).

[60] P. M. Martin, *Handbook of Deposition Technologies for Films and Coatings: Science, Applications and Technology*, third edit ed. William Andrew Publishing, 2010.

[61] S. Mahajan, *Encyclopedia of Materials: Science and Technology*, first edit ed., K. H. J. Buschow, R. Cahn, M. Flemings, B. Ilschner, E. Kramer, S. Mahajan, and P. Veyssiere, Eds. Pergamon, 2001.

[62] M. A. Herman and H. Sitter, *Molecular Beam Epitaxy: Fundamentals and Current Status*, 2nd ed., ser. Springer Series in Materials Science. Springer-Verlag Berlin Heidelberg, 1996, vol. 7, no. 3-4. [Online]. Available: https://www.springer.com/gp/book/9783642800627

[63] Cambridge, "MBE Systems Semiconductor Physics Group," sp.phy.cam.ac.uk. https://www.sp.phy.cam.ac.uk/research/molecular-beam-epitaxy (accessed Jan. 29, 2020).

[64] LCNMBE, "Molecular Beam Epitaxy London Nano," london-nano.com. https://www.london-nano.com/research/techniques/molecular-beam-epitaxy (accessed Jan. 29, 2020).

[65] Tescan, "DrawBeam for electron beam lithography: instruction for use," p. 35, 2014.

[66] ——, "Electron Beam Lithography (EBL)," p. 43, 2017.

[67] F. Pobell, *Matter and methods at low temperatures*, third, rev ed. Springer, Berlin, Heidelberg, 2007. [Online]. Available: https://doi.org/10.1007/978-3-540-46360-3

[68] G. Frossati, "Experimental Techniques: Methods for Cooling Below 300 mK," *Journal of Low Temperature Physics*, vol. 87, pp. 595–633, 1992. [Online]. Available: https://doi.org/10.1007/BF00114918

[69] L. C. B.V., *Cryogen-Free Dilution Refridgerator: Instruction Manual*. Leiden Cryogenics B.V., 2014.

[70] Tektronix, "Keithley Source Measure Units Tektronix," tek.com. https://www.tek.com/keithley-source-measure-units (accessed Jan. 1, 2021).

[71] ——, "Keithley High Resistance/Low Current Electrometers Series 6500, 6430 Tektronix," tek.com. https://www.tek.com/keithley-low-level-sensitive-and-specialty-instruments/keithley-high-resistance-low-current-electrom (accessed Jan. 1, 2021).

[72] Keithley, "Model 6430 Sub-Femtoamp Remote SourceMeter," p. 558. [Online]. Available: https://www.tek.com/document/specification/model-6430-sub-femptoamp-remote-sourcemeter-specifications.

[73] Agilent-technologies, "Agilent ESG-A and ESG-D RF Signal Generators," p. 32, 2007. [Online]. Available: https://literature.cdn.keysight.com/litweb/pdf/5989-4074EN.pdf

[74] N. Instruments, "Differences Between Function Generators, Arbitrary Function Generators, and Arbitrary Waveform Generators - National Instruments," ni.com. https://knowledge.ni.com/KnowledgeArticleDetails?id=kA00Z000000kFHYSA2{&}l=en-ZA (accessed June. 4, 2020).

[75] Tektronix, "Programmer Manual AWG5000 and AWG7000 Series Arbitrary Waveform Generators: Quick Start User Manual," p. 103, 2011.

[76] C. R. Paul, *Introduction to Electromagnetic Compatibility*, second edi ed., ser. Wiley Series in Microwave and Optical Engineering. John Wiley & Sons, INC., 2006. [Online]. Available: https://onlinelibrary.wiley.com/doi/book/10.1002/0471758159

[77] B. Adamczyk, *Foundations of Electromagnetic Compatibility: with Practical Applications*. John Wiley and Sons Ltd, 2017. [Online]. Available: https://onlinelibrary.wiley.com/doi/book/10.1002/9781119120810

[78] ——, "Spectra of Digital Clock Signals," incompliancemag.com. https://incompliancemag.com/article/spectra-of-digital-clock-signals/ (accessed Feb. 1, 2021).

[79] Tektronix, "Signal Generator Fundamentals," pp. 1–2, 2006.

[80] D. Systèmes, "CST Studio Suite 3D EM simulation and analysis software," 3ds.com. https://www.3ds.com/products-services/simulia/products/cst-studio-suite/ (accessed Feb. 14, 2021).

[81] F. Stein, H. Scherer, T. Gerster, R. Behr, M. Götz, E. Pesel, C. Leicht, N. Ubbelohde, T. Weimann, K. Pierz, H. W. Schumacher, and F. Hohls, "Robustness of single-electron pumps at sub-ppm current accuracy level," *Metrologia*, vol. 54, no. 1, pp. S1–S8, 2017.

[82] H. Howe, M. Blumenthal, H. E. Beere, T. Mitchell, D. A. Ritchie, and M. Pepper, "Single-electron pump with highly controllable plateaus," *Applied Physics Letters*, vol. 119, no. 15, p. 153102, 2021.

[83] D. Drung, C. Krause, U. Becker, H. Scherer, and F. J. Ahlers, "Ultrastable low-noise current amplifier: A novel device for measuring small electric currents with high accuracy," *Review of Scientific Instruments*, vol. 86, no. 2, pp. 1–11, 2015.